

Review

Linking the Remote Sensing of Geodiversity and Traits Relevant to Biodiversity—Part II: Geomorphology, Terrain and Surfaces

Angela Lausch ^{1,2,*}, Michael E. Schaepman ³, Andrew K. Skidmore ^{4,5},
Sina C. Truckenbrodt ^{6,7}, Jörg M. Hacker ^{8,9}, Jussi Baade ¹⁰, Lutz Bannehr ¹¹,
Erik Borg ^{12,13}, Jan Bumberger ¹⁴, Peter Dietrich ¹⁴, Cornelia Gläßer ¹⁵, Dagmar Haase ^{1,2},
Marco Heurich ^{16,17}, Thomas Jagdhuber ¹⁸, Sven Jany ¹⁹, Rudolf Krönert ¹, Markus Möller ²⁰,
Hannes Mollenhauer ¹⁴, Carsten Montzka ²¹, Marion Pause ²², Christian Rogass ¹,
Nesrin Salepci ⁶, Christiane Schmullius ⁶, Franziska Schrodt ²³, Claudia Schütze ²⁴,
Christian Schweitzer ²⁵, Peter Selsam ¹⁴, Daniel Spengler ²⁶, Michael Vohland ^{27,28},
Martin Volk ¹, Ute Weber ²⁴, Thilo Wellmann ^{1,2}, Ulrike Werban ¹⁴, Steffen Zacharias ¹⁴
and Christian Thiel ⁷

- ¹ Department Computational Landscape Ecology, Helmholtz Centre for Environmental Research–UFZ, Permoserstr. 15, D-04318 Leipzig, Germany; dagmar.haase@hu-berlin.de (D.H.); RudolfKroenert@web.de (R.K.); christian.rogass@ufz.de (C.R.); martin.volk@ufz.de (M.V.); thilo.wellmann@geo.hu-berlin.de (T.W.)
- ² Geography Department, Humboldt University Berlin, Unter den Linden 6, D-10099 Berlin, Germany
- ³ Remote Sensing Laboratories, Department of Geography, and University Research Priority Program on Global Change and Biodiversity, University of Zurich–Irchel, Winterthurerstrasse 190, CH-8057 Zurich, Switzerland; michael.schaepman@geo.uzh.ch
- ⁴ Faculty of Geo-Information Science and Earth Observation (ITC), University of Twente, P.O. Box 217, AE 7500 Enschede, The Netherlands; a.k.skidmore@utwente.nl
- ⁵ Department of Earth and Environmental Science, Macquarie University, Sydney, NSW 2109, Australia
- ⁶ Department for Earth Observation, Institute of Geography, Friedrich Schiller University Jena, Loebdergraben 32, D-07743 Jena, Germany; sina.truckenbrodt@uni-jena.de (S.C.T.); nesrin.salepci@uni-jena.de (N.S.); c.schmullius@uni-jena.de (C.S.)
- ⁷ DLR Institute of Data Science, Mälzerstraße 3, D-07743 Jena, Germany; christian.thiel@dlr.de
- ⁸ College of Science and Engineering, Flinders University, Adelaide, SA 5000, Australia; jmh@flinders.edu.au
- ⁹ Airborne Research Australia (ARA), Parafield Airport, Adelaide, SA 5106, Australia
- ¹⁰ Department of Physical Geography, Institute of Geography, Friedrich Schiller University Jena, Loebdergraben 32, D-07743 Jena, Germany; jussi.baade@uni-jena.de
- ¹¹ Department of Architecture, Facility Management and Geoinformation, Institut for Geoinformation and Surveying, Bauhausstraße 8, D-06846 Dessau, Germany; l.bannehr@afg.hs-anhalt.de
- ¹² German Remote Sensing Data Center–DFD, German Aerospace Center–DLR, Kalkhorstweg 53, D-17235 Neustrelitz, Germany; erik.borg@dlr.de
- ¹³ Geodesy and Geoinformatics, University of Applied Sciences Neubrandenburg, Brodaer Strasse 2, D-17033 Neubrandenburg, Germany
- ¹⁴ Department Monitoring and Exploration Technologies, Helmholtz Centre for Environmental Research–UFZ, Permoserstr. 15, D-04318 Leipzig, Germany; jan.bumberger@ufz.de (J.B.); peter.dietrich@ufz.de (P.D.); hannes.mollenhauer@ufz.de (H.M.); peter.selsam@ufz.de (P.S.); ulrike.werban@ufz.de (U.W.); steffen.zacharias@ufz.de (S.Z.)
- ¹⁵ Department of Remote Sensing, Martin Luther University Halle-Wittenberg, Von-Seckendorff-Platz 4, D-06120 Halle, Germany; cornelia.glaesser@geo.uni-halle.de
- ¹⁶ Department of Conservation and Research, Bavarian Forest National Park, Freyunger Straße 2, D-94481 Grafenau, Germany; marco.heurich@npv-bw.bayern.de
- ¹⁷ Faculty of Environment and Natural Resources, University of Freiburg, Tennenbacher Straße 4, D-79106 Freiburg, Germany
- ¹⁸ German Aerospace Center (DLR) Microwaves and Radar Institute, Oberpfaffenhofen, D-82234 Wessling, Germany; thomas.jagdhuber@dlr.de
- ¹⁹ MILAN Geoservice GmbH, Zum Tower 4, D-01917 Kamenz, Germany; s.jany@milan-geoservice.de

- ²⁰ Federal Research Centre for Cultivated Plants, Institute for Crop and Soil Science, Research Centre for Agricultural Remote Sensing (FLF), Julius Kühn Institute (JKI), Bundesallee 69, D-38116 Braunschweig, Germany; markus.moeller@julius-kuehn.de
- ²¹ Forschungszentrum Jülich GmbH, Institute of Bio- and Geoscience, Agrosphere (IBG-3), Wilhelm-Johnen-Str. D-52428 Jülich, Germany; c.montzka@fz-juelich.de
- ²² Institut of Photogrammetry and Remote Sensing, Technical University Dresden, Helmholtzstr. 10, D-01061 Dresden, Germany; marion.pause@tu-dresden.de
- ²³ School of Geography, University of Nottingham, University Park, NG7 2RD Nottingham, UK; franziska.schrodt1@nottingham.ac.uk
- ²⁴ Computational Hydrosystems Helmholtz Centre for Environmental Research–UFZ, Permoserstr. 15, D-04318 Leipzig, Germany; claudia.schuetze@ufz.de (C.S.); ute.weber@ufz.de (U.W.)
- ²⁵ German Environment Agency, Wörlitzer Platz 1, D-06844 Dessau Roßlau, Germany; christian.schweitzer@uba.de
- ²⁶ Helmholtz Center Potsdam, German Research Center for Geosciences, Telegrafenberg, D-14473 Potsdam, Germany; daniel.spengler@gfz-potsdam.de
- ²⁷ Geoinformatics and Remote Sensing, Institute for Geography, Leipzig University, Johannisallee 19a, D-04103 Leipzig, Germany; michael.vohland@uni-leipzig.de
- ²⁸ Remote Sensing Centre for Earth System Research, Leipzig University, Talstr. 35, D-04103 Leipzig, Germany
- * Correspondence: angela.lausch@ufz.de; Tel.: +49-341-235-1961; Fax: +49-341-235-1939

Received: 22 September 2020; Accepted: 3 November 2020; Published: 10 November 2020



Abstract: The status, changes, and disturbances in geomorphological regimes can be regarded as controlling and regulating factors for biodiversity. Therefore, monitoring geomorphology at local, regional, and global scales is not only necessary to conserve geodiversity, but also to preserve biodiversity, as well as to improve biodiversity conservation and ecosystem management. Numerous remote sensing (RS) approaches and platforms have been used in the past to enable a cost-effective, increasingly freely available, comprehensive, repetitive, standardized, and objective monitoring of geomorphological characteristics and their traits. This contribution provides a state-of-the-art review for the RS-based monitoring of these characteristics and traits, by presenting examples of aeolian, fluvial, and coastal landforms. Different examples for monitoring geomorphology as a crucial discipline of geodiversity using RS are provided, discussing the implementation of RS technologies such as LiDAR, RADAR, as well as multi-spectral and hyperspectral sensor technologies. Furthermore, data products and RS technologies that could be used in the future for monitoring geomorphology are introduced. The use of spectral traits (ST) and spectral trait variation (STV) approaches with RS enable the status, changes, and disturbances of geomorphic diversity to be monitored. We focus on the requirements for future geomorphology monitoring specifically aimed at overcoming some key limitations of ecological modeling, namely: the implementation and linking of in-situ, close-range, air- and spaceborne RS technologies, geomorphic traits, and data science approaches as crucial components for a better understanding of the geomorphic impacts on complex ecosystems. This paper aims to impart multidimensional geomorphic information obtained by RS for improved utilization in biodiversity monitoring.

Keywords: geomorphology; terrain; surface; geodiversity; fluvial; aeolian; coastal; traits; spectral traits; remote sensing; earth observation; DEM; DTM; DSM; monitoring

1. Introduction

The evolutionary and ecological processes, structures, and functions of life on Earth are strongly influenced by multi-faceted geophysical processes, shaping geomorphic factors, and geodiversity on all spatio-temporal scales [1,2]. Geodiversity, including the lithosphere, the atmosphere, the hydrosphere,

and the cryosphere [3], is the controlling and regulating factor for landscape processes and thus a decisive factor for biodiversity. Organisms both respond to [4] and significantly alter their abiotic environment, affecting, for example, nutrient loads, weathering rates, sediment transport, and water cycles. Indeed, recent work has shown that knowledge of geodiversity has a paradigm-shifting ability to improve predictions about the effects of environmental change on biodiversity [5,6] and that the successful conservation of biodiversity requires the conservation of geodiversity [7]. Of particular importance is the link with the maintenance or restoration of species diversity, ecosystem resilience, and connectivity in the face of climate change [7,8]. Monitoring geodiversity and its relation to biodiversity, ecosystem, and ecological integrity [1,9,10] is thus essential if we are to effectively manage our natural resources.

In the last decade, global conservation organisations have started to recognize that protected areas should address aspects of geodiversity and that geodiversity is part of natural diversity [11–13]. Consequently, these factors are increasingly being integrated into nature conservation planning and management measures, and adopted by nature conservation designations such as the Geoconservation programme of the International Union for the Conservation of Nature (IUCN, 2018) [11]. Gray et al. [14] provided an integrative review as a contribution to the sustainable management of ecosystems based on geodiversity, defining geodiversity as the diversity of abiotic features and their surface and subsurface processes or generally as the abiotic diversity of the Earth's surface, which is represented by various geomorphic characteristics. Lausch et al. [3] extended this approach by defining geodiversity as “the range and variability of geo-components and their intraspecific and interspecific interactions on all levels of organization of their geo-components”. In the latter, five basic characteristics of geodiversity were defined, namely: geo-genesis diversity (GGD), geo-taxonomic diversity (GTaxD), geo-structural diversity (GSD), geo-functional diversity (GFD), as well as geo-trait diversity (GTD). Numerous interpretations of the geodiversity definition exist and the question as to whether a geocompartment belongs to geodiversity or not sometimes becomes a controversial issue [15]. All definitions of geodiversity account for geomorphic characteristics and their traits.

The physical and chemical weathering of rocks and mass movements induce the formation of particular geomorphic structures and patterns, which form the basis of different geomorphic functions [16]. In this way, specific landforms developed from the geological process of geo-genesis (e.g., kettle holes from retreating glaciers, gullies from fluvial processes or various mountain, volcano, and coast types), creating specific microrefugia with characteristic morphological, hydrological, climatic, lithological, and soil patterns. Geomorphic diversity therefore creates the basis for niches and habitat diversity.

Mountains are landforms [1] that can act as central interfaces with all other geo-factors, such as the climate, water, lithology, and soil, defining biodiversity at alpha, beta, and gamma levels, i.e., through species richness, or Shannon or Simpson diversity (see also [17]). They help when explaining patterns in the distribution of flora and fauna [18,19], leading not only to the development of distinct plant strategies and plant functional types [20,21], but also to spatial differentiation and speciation in animal populations due to barrier effects. Consequently, landforms, such as landslide scars [16,22] or water channels [23], make a crucial contribution to the richness, composition, and the occurrence of characteristic species traits and communities. Furthermore, geomorphic variables derived from digital elevation models (DEM) explain “the potential to open new research avenues for a variety of research disciplines that require detailed geomorphometric and land and aquatic surface information” [24]. A comprehensive overview of the state on landslides and quaternary climate changes is given by Pánek [25].

Geomorphic characteristics and their traits exist on all spatio-temporal scales [26,27], creating a strong link to biodiversity patterns and their interactions on a local, regional and even landscape scale [3]. Numerous studies have investigated the importance of individual geo-components to biodiversity from the local or the patch scale [28,29] to the global scale [30,31] and investigated on which scales geodiversity is most relevant for biodiversity [32].

Patterns of bio- and geodiversity are particularly defined by topography, which defines the terrain, the three-dimensional quality of the surface, and the identification of specific landforms [33]. For example, topographic complexity is one of the main factors influencing the global patterns of mountain biodiversity [34]. Furthermore, topography explains the distribution of genetic diversity in one of the most fragile European hotspots of plant species [35]. The combination of both topography and climate also greatly influences the distribution patterns of vegetation on Earth [36]. More broadly, changes in species distribution, abundance, performance, and richness are shaped by geomorphic traits such as slope, aspect, curvature, variables of morphometry, lighting, visibility, soil moisture, or hydrological factors, such as channels, drainage networks, flow directions, or valley depths. Yet, current large-scale biodiversity models mainly focus on coarse and easily measured macroclimatic and topographic predictor variables, whilst largely ignoring other key aspects of the Earth's surface and subsurface. Moreover, most analyses of biodiversity change do not consider the range of spatial and temporal scales at which geomorphic processes and traits act and the mechanisms by which they influence biodiversity. Despite meta-analyses [37] and recent progress (e.g., [5,6]), there remain fundamental gaps in synthesizing and integrating the links between biodiversity and geodiversity, especially for biogeography, macroecology, conservation planning, and global change biology [38].

Remote sensing (RS) can monitor geomorphic traits and changes in them. Due to sensor-specific RS characteristics such as spatial, spectral, temporal, or directional resolution, RS measurements with, e.g., insufficient spatial resolution, can lead to a loss of important information and subsequently to erroneous statements or input variables for ecosystem models [37–40]. In combination with modelling approaches, RS research is used to improve topographic base maps and to monitor landscape management, geoengineering, geomorphology, geohydrology, and geoecology [39–41]. RS is of particular importance in the prediction of geohazards, such as volcano eruptions and earthquakes, flooding, landslides, permafrost-related hazards, mass movements, soil erodibility, and erosion on land and in coastal waters [42,43]. Recent RS technologies such as the satellite-based light detection and ranging (LiDAR), global ecosystem dynamics investigation (GEDI) [44,45], as well as upcoming radio direction and ranging (RADAR) technologies such as the Tandem-L [46,47], NISAR (NASA-ISRO Synthetic Aperture RADAR) or even Rose-L (Copernicus High Priority Candidate Mission), alone and in combination with imaging spectroscopy [48] and thermal infrared (TIR) sensor technology such as the Copernicus Hyperspectral Imaging Mission (CHIME) [49], the Hyperspectral Infrared Imager Mission (HypIRI, [50]) and Environmental Mapping and Analysis Program (EnMAP, [51]), open up new opportunities for a global monitoring of geo- and biodiversity and their interactions [3,52–54].

With the target-oriented open data policies for RS data [55–57], the continuity of RS time series like Landsat-5–9 [58] and increasingly more freely available RS-data products [59], the monitoring of geomorphology with RS sensors on close-range, as well as airborne and spaceborne platforms has been integrated for some years now into ecological modelling and geoengineering in science, economics, planning, and political decision-making processes. Indeed, the growing number of existing and future RS sensors and new technologies provide researchers, planners and political decision-makers tremendous opportunities. However, it is becoming increasingly difficult to get a proper overview or an understanding of which RS sensors, missions, and platforms can be used to monitor geomorphic characteristics and their traits. The goals of this paper are therefore as follows:

- To document the state of the art of existing and upcoming RS technologies in air- and spaceborne RS for monitoring terrain and surfaces by using examples of aeolian-, fluvial- and coastal- landforms and their traits.
- To provide a short overview of existing RS data products in the context of geomorphology.
- To present a concise overview of the geomorphic characteristics and their traits that can be recorded by RS.

The following chapters present the state-of-the-art for monitoring geomorphic landforms using airborne (UAV, airplanes), spaceborne (satellite) RS sensors (Figure 1). We discuss different technologies,

such as RADAR, LiDAR, thermal, multispectral, and hyperspectral sensors, that can be used for monitoring geomorphic characteristics and their traits. Furthermore, we address current and future satellite-borne sensors and missions as well as existing RS data products that enable the recording and monitoring of geomorphology, land terrain, and land surfaces.



Figure 1. Different air- and spaceborne remote sensing platforms for assessing geomorphological landforms and their traits: (a) unmanned aerial vehicles (UAVs) or drones, (b) microlight-gravity-controlled aircrafts (c) gyrocopter-microlight helicopter, (d) ECO-Dimona aircraft (top) and Cessna aircraft (bottom), and (e) satellite (from Lausch et al. [3]).

2. Remote Sensing Techniques for Monitoring Geomorphology—Terrain and Surfaces

Both land surface and relief influence the distribution and characteristics of geographic patterns of biodiversity by isolating and connecting plant and animal populations [60]. Surface elevation provides the foundation for many aspects of biodiversity, such as the vertical and spatial vegetation structure and fragmentation, homogeneity, biomass, age, and the height of the vegetation. Surface elevation influences the microclimate and precipitation patterns, affecting species distribution and primary production. Hence, surface elevation data are important to detect changes in ecosystems. Moreover, they build the basis for models that represent the height of the terrain surface (digital elevation models, DEMs) or models that represent surface heights and the height of buildings or vegetation (digital surface models, DSMs). If both DEM and DSM are available for an area, then the height difference from them results in the height of the vegetation or buildings, which is commonly referred to as the normalised digital surface model (nDSM). DEMs and DSMs are increasingly being combined with multi-temporal and multi-/hyperspectral RS data to describe biodiversity features in their complex multidimensionality. These models are of major importance for quantifying, modelling and monitoring plant and animal species distributions, especially at small spatial scales [32,61]. Terrain features such as slope aspect, slope gradient and terrain position are crucial variables that are derived from a DEM. These variables are essential for landscape analysis, evaluation, and modelling in geo- and biodiversity [62,63]. High resolution spatial 3D vegetation geometry is increasingly used as information for modelling animal movement and migration behaviours [64] and to describe the microclimate of animal and plant species habitats [65,66].

For a long time ground-based in-situ point measurement methods were the only way to collect the base data for elevation maps. Surveyors traditionally used instruments such as tapes, compasses, theodolites, sextants, and aneroid barometers for mapping. The development of plane tables and alidades increased the precision of measurements. With the invention of tachymeters that determine distances through traveling time or the phase shift of light and the differential global navigation satellite system (CDGNSS), measurement precision has become even more accurate to the order of centimetres [67]. With these technologies, digital data collection has also emerged in the field of mapping, reducing the amount of cumbersome and laborious work. Nevertheless, these techniques are still labour intensive and only enable point measurements. For these reasons, it was difficult to achieve a universal ground-based survey of elevation data that fulfil the requirements of biodiversity studies and modern monitoring approaches.

In the 19th century, airborne stereo-photogrammetry was developed [68], but considerable efforts still had to be made to obtain the desired results. Air- and spaceborne RS were able to overcome this limitation, enabling acquisitions of elevation data from the local to the global scale. The most

ground-breaking development in terms of the acquisition of a global high-resolution digital terrain database was the International Shuttle RADAR Topography Mission—SRTM, which was on-board the Space Shuttle Endeavour for 11 days in February 2000 using a C-/X-band RADAR. This ultimately led to 1 or 3 arc degree global coverage [69].

Round about the same time airborne LiDAR systems became available [70] which were able to map surfaces at very high resolution from the local to the regional scale. Today, these systems are arguably the most commonly used systems in geomorphic-relevant applications [71]. Other systems are airborne and spaceborne SAR (synthetic aperture RADAR) and InSAR systems (interferometric SAR, [72]) that enable geomorphology to be monitored with accuracy levels to the mm. For example, SAR interferometers enable the monitoring of unstable slopes in high mountain ranges [73,74].

Over recent years, the automatic photogrammetric processing of aerial images developed to a level where even laypeople were easily able to generate high resolution DEMs. As this method only requires a camera and a positioning system, it enables the wide-spread use of UAVs and airplanes to map the landscape. Numerous examples of how terrain, surfaces, and their changes can be derived using air- and spaceborne RS techniques are shown in Figure 2.

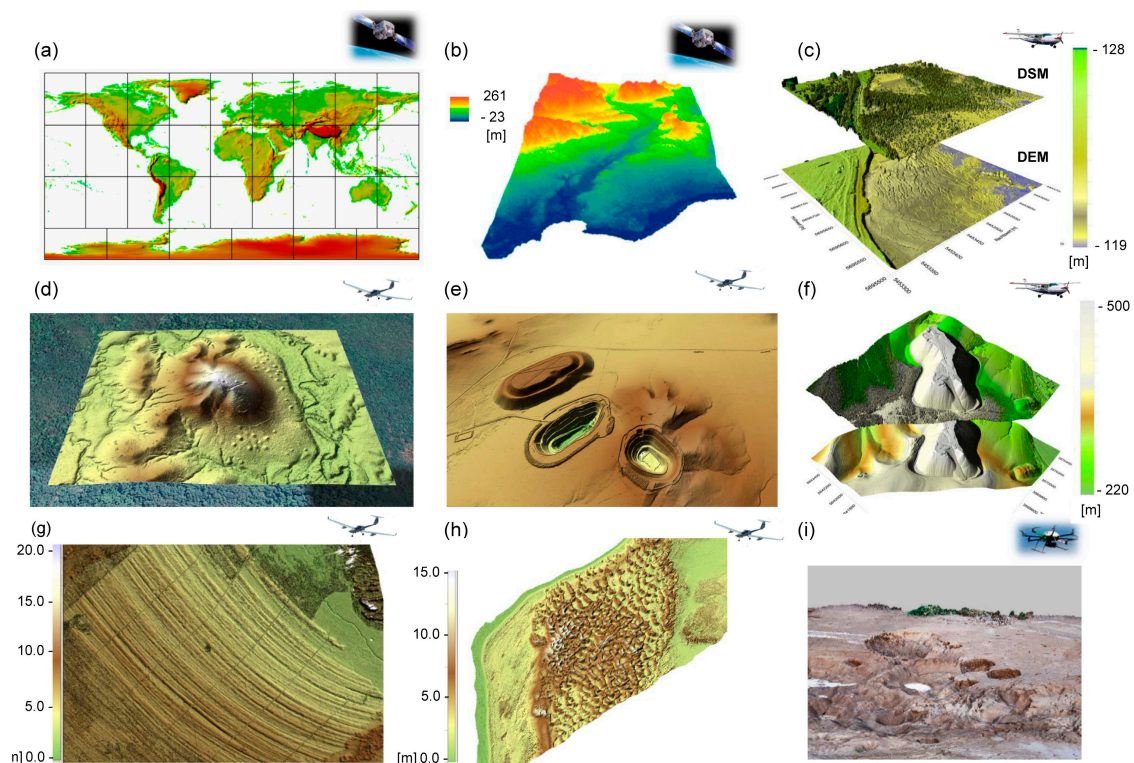


Figure 2. Elevation, terrain and surfaces as crucial characteristics for all geomorphological landforms can be monitored with different air- and spaceborne RS technologies: (a) Digital Elevation Model (DEM)—GTOPO30, (b) an oblique, three-dimensional (3D) perspective of the DEM of the downstream area of Wadi El-Ambagi derived from a WorldView-2 stereo pair [75], (c) Digital Surface Model DSM and DEM derived from airborne LiDAR, area of reforestation in the former open-cast mining region Lausitz, Germany, (d) DEM of a rainforest area in Cape York (Australia) showing mining exploration scars and revealing groups of Brush Turkey mounds (airborne LiDAR—RIEGL Q680i-S), (e) 50 cm DEM of a mine site rehabilitation area near Morawa (Australia, airborne LiDAR—RIEGL Q680i-S), (f) DSM and DEM derived from airborne LiDAR acquisitions of an open pit mining dump of Wintershall in Germany, (2 km × 2 km, >12 points/m²), (g) low resolution DEM of a dunescape in Tasmania (airborne LiDAR—RIEGL Q680i-S), (h) 25 cm DEM of sand dunes at the Tubridgi Coast in North West Australia (airborne LiDAR—RIEGL Q680i-S) and, (i) a land surface with 3D sinkholes in Israel (UAV).

2.1. Stereophotogrammetry and Related Approaches

Stereophotogrammetry requires the acquisition of image data of the same area from slightly different positions. Due to the different viewing angles along the flight path of a platform, differences in elevation result in a different parallax, which can be measured and converted into elevation differences. Aerial images, for example, are often acquired with an overlap of more than 50% along the track. This allows stereoscopic measurements in the overlapping area. Pushbroom-like line scanners can be installed in such a way that enable forward view, nadir view, and backward view image strips to be recorded separately, allowing stereoscopic measurements. While airborne RS data can only be recorded under optimal weather conditions (no clouds, suitable lighting conditions), the data quality of optical data decreases enormously under cloud cover or poor lighting conditions. However, VNIR (visible and near infrared) can also be acquired below any clouds or even during heavy rain. This depends on the desired total signal-to-noise ratio (SNR), the flight altitude and the speed of, e.g., the aircraft or UAV. The advantage of airborne RS data is that the people interested in (or paying for) it have some control over the acquisition time, the spatial and spectral characteristics of the RS data. For spaceborne sensors this is rarely the case. One further advantage is that the resolution and precision of airborne is generally much higher than spaceborne RS, but the covered area is much bigger for spaceborne RS. For instance, for UAV we can have cm resolution and precision, while for spaceborne we have only very recently had m resolution (see also chapter 2.4, Table 1)

Radargrammetry could solve this matter since it resorts to SAR data, for the acquisition of which illumination conditions (active sensor) and cloud cover are not that relevant (for a frequency ≤ 4 GHz electromagnetic (EM) waves penetrate clouds). Furthermore, there is a dependency with regard to different cloud types. In general, the approach of radargrammetry is identical to stereophotogrammetry except for the fact that the amplitude of the SAR signal is used instead of optical data. Because of the specifics of the RADAR geometry, additional processing steps are required. Due to the fact that the geometric resolution of RADAR used to be lower than the optical data, which were used during the photogrammetric DEM generation, and because the SAR-inherent speckle causes a degradation of the results, so far SAR data have not been widely used for elevation models. However, with the launch of sensors such as TanDEM-X, TerraSAR-X, Cosmo-Skymed, and ALOS-2 PALSAR, providing data with a geometric resolution as high as 1 m, radargrammetry has recently become a valid approach to fill gaps in cloud-prone regions or feature other peculiarities that complicate the stereophotogrammetry or InSAR [76].

Over recent years, UAVs have been increasingly used for monitoring the status, changes or disturbances of geomorphic characteristics [77–80]. Once the hardware, operator training and licencing, UAV licensing, insurance, and institutional certification (although not yet universal, but heading that way for many countries) have been organized, data can be recorded at a comparatively low cost for many applications. The image parameters, such as spectral channels, image overlap, and geometric resolution can be determined according to the mission requirements [81]. The overlap between the images enables stereoscopic image processing, the generation of seamless image mosaics, and the triangulation of high-density 3D point clouds (Figure 3). For the operational delineation of these products, several commercial and open source software packages are available. This kind of software commonly comprises bundle adjustment and structure from motion (SfM) algorithms [82,83]. In particular, this approach is increasingly being used to record geomorphic characteristics [84].

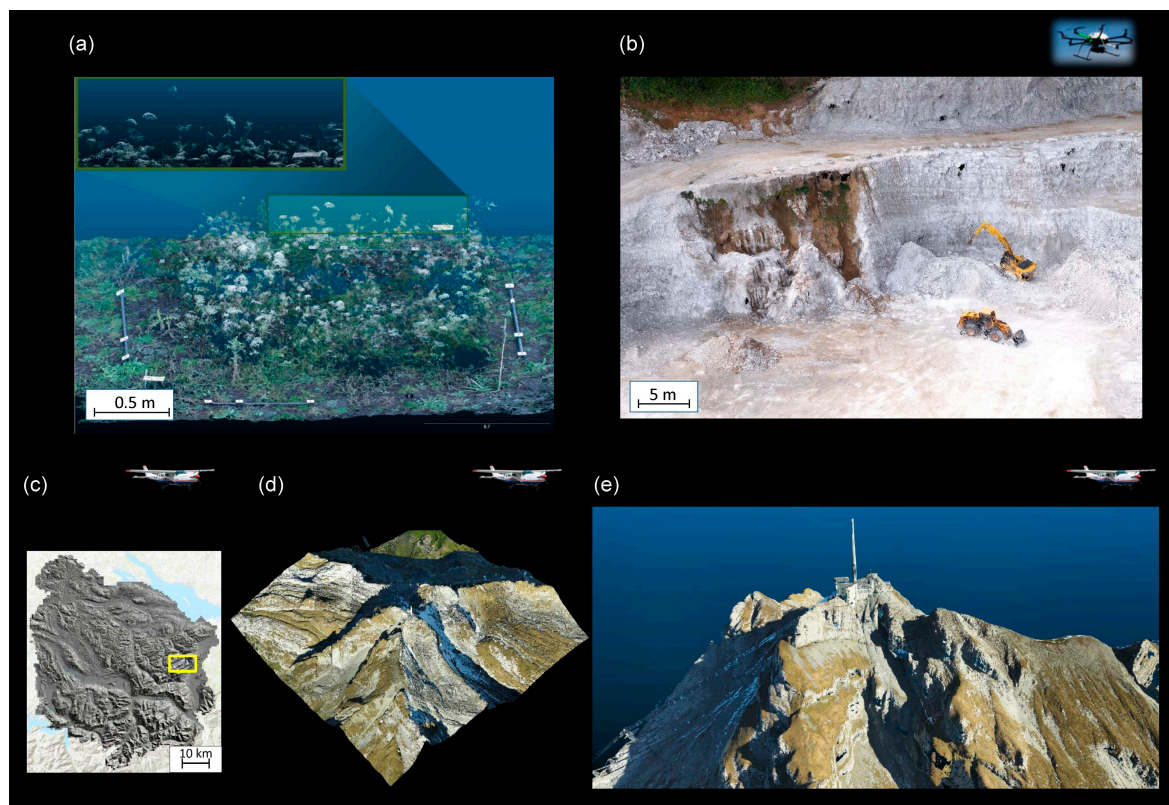


Figure 3. Three-dimensional (3D) representations derived from overlapping images: (a) Representations of 3D plant species structure “*Onobrychis viciifolia*” and “*Daucus carot*” created with Structure from Motion (SfM) techniques as well as the use of a Time of Flight (TOF) 3D camera, a laser light sheet triangulation system and a coded light projection system (from Kröhnert et al., [85]), (b) Structure from Motion (SfM) techniques based dense point cloud that shows a gypsum mine close to Nordhausen, Germany. In total 250 RGB (red-green-blue) pictures, average point density 1020 points/m², UAV, (c–e) Digital Surface Model (DSM)—Santis Sankt Gallen, Switzerland, Aerial Laser Scanner (ALS)—LiDAR (RIEGL), point density (15 points/m²), total 51 million points, airplane.

Based on the point cloud DSMs (digital surface models) and after vegetation filtering, DEMs can be delineated by rasterizing the point clouds. UAV-based DSMs and DEMs can therefore be used to accurately measure the canopy height [86]. Due to regulations and technical limitations, however, UAVs are currently only used for acquisition at a local scale. When considering a visual line of sight, i.e., a maximum distance of 100–500 m between the pilot and the UAV (a legal requirement in many countries), a theoretical area of 78.5 ha can be covered in one flight. It is possible to increase the monitoring area to be recorded by changing the UAV pilot’s location, transferring control to another pilot (at a different location) during the flight, or establishing technical BVLOS (beyond visual line of sight) systems. For the retrieval of elevation data products based on stereophotogrammetry and related approaches, equal points or image objects must be identified and accurately detected in all overlapping images. Particularly, in areas with low contrast (e.g., snow-covered areas), the number of reliable points can be very low. Furthermore, this method is not viable over water. In such areas a large number of ground control points (GCP) is therefore required, leading to higher production costs. In many cases, the number and positional accuracy of detectable points per unit area rises with increasing spatial resolution. A high point density enables small raster cells in the final elevation model.

In 2009, NASA’s Advanced Spaceborne Thermal Emission and Reflection Radiometer (ASTER) aboard the Earth Observation satellite Terra provided a global DSM based on spaceborne optical data. Image acquisitions from two different angles along the satellite’s track allowed a stereographic analysis, resulting in absolute heights with an average standard deviation of 13 m [87,88]. A possible limitation

for some disciplines may be the spatial resolution of 30 m. Hence, more recent developments have focused on improving the spatial resolution, starting with an optical sensor, the Panchromatic Remote Sensing Instrument for Stereo Mapping (PRISM) aboard the Advanced Land Observing Satellite (ALOS) that was in operation from 2006 to 2011. The current global DSM yields a spatial resolution of around 5 m with a height root mean square error (RMSE) of 5 m [89,90]. Aldorsari and Jacobsen [91] and Alganci et al. [92] provided a quality assessment of DEM models from different spaceborne sensors.

As discussed above, radargrammetry can be a valuable approach in areas where no optical data is available. In fact, the German mission TanDEM-X mission (two twin satellites flying in a helix-formation) provided a suitable dataset for the generation of global radargrammetry-based elevation models like the WorldDEM. Airbus is promoting the WorldDEM, but the WorldDEM is an interferometric product: The description of WorldDEMcore: “This Digital Surface Model (DSM) represents the surface of the Earth including buildings, infrastructure and vegetation. This unedited DSM is output of the interferometric processing without any refinement. This product usually contains RADAR specific artefacts, voids, and can include processing artefacts”. Source: https://api.oneatlas.airbus.com/documents/2018-07_WorldDEM_TechnicalSpecs_Version2.4_I1.0.pdf. However, since the TanDEM-X mission has InSAR capabilities (see Section 4.3), enabling even more accurate elevation models, a global radargrammetry-based model might not be produced.

2.2. Approaches by InSAR

InSAR-based elevation models rely on the phase signal of electromagnetic waves. The SAR phase basically depends on object trait characteristics (controlling the scattering process) and the distance between SAR and the Earth’s surface [93,94]. Thus, at least two phase data sets are required to separate both impacts. In the case of InSAR, both phase data sets are acquired from slightly different positions (the maximum distance is determined by the critical baseline) and feature the same polarisation [94,95]. Thus, the object phase can be assumed equal in both images and is cancelled out when the phase differences are computed. Ultimately, the remaining range difference is exploited. The range difference can be used to infer the height of any given point. Thus, InSAR is the only instrument that provides continuous (resolution or sub aperture cell-wise) height measurements from space, even in the presence of cloud. The height value of each resolution cell represents the location of the scattering phase centre.

In the case of surface scattering, where the scattering process takes place at the boundary between air and a surface (e.g., bare soil), the scattering phase centre represents the elevation of this boundary. For volume scattering, where the scattering process takes place at several locations along a vertical profile (e.g., the forest canopy), the scattering phase centre is located somewhere within this volume [96–98]. The ultimate position in a forest canopy primarily depends on the canopy gap fraction and the attenuation of the electromagnetic wave by individual trees, but only hiding the desired geomorphic traits (the ground). Low attenuation results in deep penetration of the wave and thus in a reduced height of the scattering phase centre, whereby penetration increases with an increasing wavelength [97–100]. In terms of environmental conditions it maximized for very dry or frozen conditions and can reach several meters of penetration for L-band data (~1–2 GHz) [99]. Accordingly, DSMs based on InSAR (and radargrammetry) do not necessarily represent the real surface of a vegetation layer, which results in an underestimation of the nDSM. Nevertheless, SAR-based nDSMs can be used as a proxy for tree height (Figure 4e1–e3).

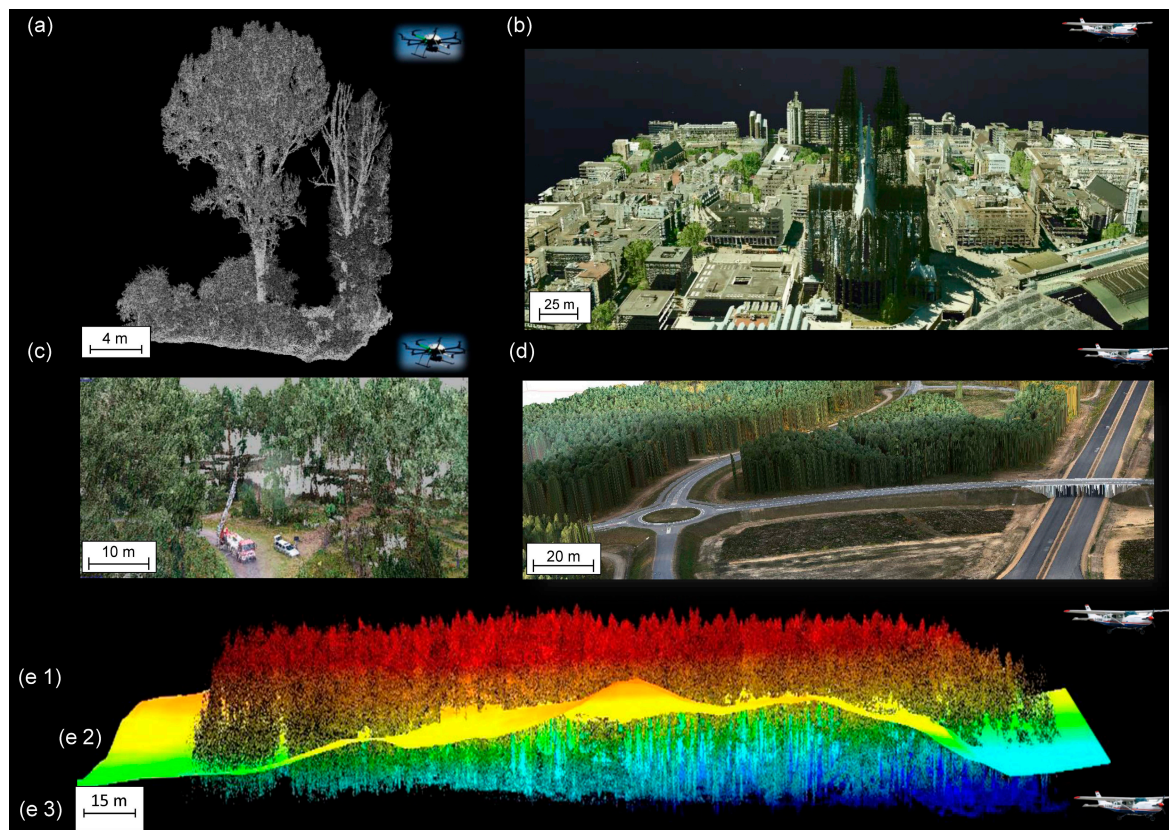


Figure 4. Digital Surface Model (DSM) recorded by different sensors and mounted on various RS platforms: (a) DSM—Terrestrial Laser Scanner—LiDAR (RIEGL VUX-1), point density (250 points/m^2), on UAV (RiCopter), (b) DSM with Terrestrial Laser Scanner—LiDAR (RIEGL VUX-1), point density (30 points/m^2), on airplane, Cologne, Germany, (c) DSM—RGB (Sony NEX-7 RGB) image data-based point cloud (natural colour), on UAV (modified after Thiel et al. [86]), (d) DSM—RGB image based point cloud, on airplane, (e) DSM comparisons of (e1) a Terrestrial Laser Scanner (TLS) DSM point cloud, (e2) a TanDEM-X DSM (satellite) and (e3, blue color) the DTM from the Federal LiDAR survey (airplane). The maximum extent of the TLS dataset is approximately 200 m and the resolution of the TanDEM-X DSM is $5 \times 5 \text{ m}^2$. (e2) Note that the TanDEM-X DSM is located within the canopy, illustrating the true backscatter center of the RADAR returns.

The ideal configuration of an InSAR system aiming to generate elevation models is achieved when both phase images are acquired at the same time. This configuration is referred to as a single pass. To date, two spaceborne missions have acquired single-pass InSAR data. The Shuttle RADAR Topography Mission (SRTM) was the first mission to generate a near-global DSM. The slightly different viewing angle was achieved by extending a 60 m mast from the payload bay of the Space Shuttle Endeavour, which hosted one of the antennas on its end. The other antenna was mounted at the payload bay of the shuttle. Within 11 days a full coverage of the globe from 56°S to 60°N of C-band InSAR data was achieved. At the same time, the German Aerospace Center (DLR) operated a second X-band interferometer. Due to its smaller swath width, however, it was not possible to cover the entire area from 56°S to 60°N . Based on the C-band data, several elevation products have been released, the most recent of which was SRTM Plus or SRTM NASA V3, with a raster cell size of $30 \text{ m} \times 30 \text{ m}$ [101]. Most voids are filled using the ASTER Global Digital Elevation Model—ASTER GDEM2 [87] and the ASTER GDEM3 (ASTGTM) [88]. A release took place in 2016, with preliminary results already showing an RMSE of the elevation of 2.3 m compared to ICESat/GLAS data [102].

The second single-pass spaceborne mission (operated by DLR) is a constellation of two satellites with X-band sensors on board that fly in a helix formation, namely TanDEM-X and TerraSAR-X.

The concerted orbits result in a slightly different viewing angle as required for elevation sensitive interferometers. Between 2010 and 2015, all land masses on Earth were scanned several times resulting in a global DEM of to date unprecedented resolution and accuracy. The raster cell size is $10\text{ m} \times 10\text{ m}$, the absolute vertical mean error of the DEM is smaller than $\pm 0.20\text{ m}$ and the RMSE is smaller than 1.4 m [103]. The TanDEM-X DEM was completed in September 2016. Currently, a new single-pass InSAR mission is being prepared under the guidance of DLR. Besides the mentioned spaceborne missions, several airborne systems operate as single-pass interferometers. Some of these systems (e.g., F-SAR, PAMIR) acquire very high resolution InSAR data (resolution cell $<1\text{ m}^2$).

Another configuration for the acquisition of InSAR data is the repeat-pass constellation. In this constellation phase, image pairs are not acquired at the same time. The minimum time lag for repeat-pass spaceborne systems that is suitable for InSAR is one day [104]. This one-day time lag was achieved for the first time during the ERS -1/-2 tandem operation phase when one of the two ERS satellites acquired the first phase image and the other satellite acquired the second phase image. A recent mission that features this minimum time lag is COSMO-SkyMed, which comprised four satellites in total. The orbits were chosen in such a way that the repeat-pass interval along the same ground track varies between one and 15 days. In contrast, the European Sentinel-1 constellation comprises two satellites. Each of the satellites repeats the same ground track every 12 days. The 180° orbital phase difference of both Sentinels results in a combined repeat-pass interval of 6 days.

Single SAR satellites commonly feature a larger time lag between both InSAR acquisitions. For instance, the repeat cycle of RADARSAT-2 is 24 days and 14 days for ALOS-2. The major disadvantage of repeat-pass systems is that they require stable biophysical conditions on the Earth's surface. Change, caused by the movement of vegetation due to wind, plant growth variations in moisture content, and traits of the soil or vegetation, affects the scattering processes and leads to a decorrelation between both phase images. Small changes might just cause a degradation of the InSAR data quality while major changes can result in complete decorrelation, inducing an entire loss of the interferometric information. In general, the probability of decorrelation increases with increasing length of repeat-pass intervals. When working with shorter wavelengths, such as X-band or C-band, vegetated areas are often completely decorrelated after several days. On the other hand, X-band data-based interferograms featuring high coherence can be retrieved when vegetation is absent and the surface parameters such as roughness and upper soil moisture remain stable. As longer wavelengths, such as L-band or particularly P-band, interact with larger (and thus temporally more stable) objects, sufficient coherence between both acquisitions can be found even for repeat-pass intervals of several days. ESA's forthcoming Earth Explorer mission BIOMASS (first P-band repeat-pass interferometer in space) and CONAE's SAOCOM mission (L-band) rely on this physical context. Another important fact is that electromagnetic waves featuring longer wavelengths are capable of penetrating deeper into media such as forest canopies. For example, P-band has the capability of penetrating through dense vegetation. Thus, BIOMASS will be the first spaceborne SAR mission providing DEMs in areas covered by dense forest such as tropical forest, while previous SAR missions only provide DSM-like DEMs (DEM plus a height component related to vegetation height). The aspired cell size of the BIOMASS mission DEM raster data is approximately $200\text{ m} \times 200\text{ m}$. An important concern of repeat-pass InSAR systems is related to the varying impact of tropospheric conditions, which can result in defective elevation measurements, in particular with shorter wavelengths.

The absolute height accuracy of InSAR-based elevation products enables geomorphic changes, i.e., in the terrain or surface to be detected at several metres only. Accordingly, InSAR-based elevation models therefore enable the detection of new clear cuts in forests, but are usually not accurate enough for the detection of subsidence in mining or karst areas. By using more than two phase images however, terrain changes can be measured with an accuracy of several millimetres, even with spaceborne sensors. The approach for the delineation of elevation changes is called Differential SAR Interferometry (DInSAR) [105,106]. Analogically to InSAR, stable environmental conditions are required for all (at least) three phase images. Therefore, areas with vegetation cover can hardly be investigated with

DInSAR. The use of long wavelengths such as the L- or P-band can remedy this [107,108]. A special form of DInSAR is the persistent scatterer interferometry (PSI) [109] (see also Figure 5). This technique only considers temporally stable scattering objects (persistent scatterers), which are selected using specific filter approaches. Subsequently, relative phase changes and thus elevation changes between these scattering objects are computed. This technique allows the integration of phase images from long time periods up to several years. Thus, elevation changes can be monitored over a very long time and movement rates can be determined with accuracy. However, persistent scatterers are hardly found in areas with vegetation cover, while a relatively high density is typical for urban areas. As DInSAR and PSI use repeat-pass data acquisition techniques, atmospheric impacts need to be considered. The common approach is to screen the temporal stack and to eliminate corrupted/strongly affected images.

Based on PSI there are numerous applications for monitoring surface deformations in mining, landslide monitoring intensity [110,111], ice motion research [112], seismotectonics or volcanology [109]. Figure 5 shows subsidence revealed by PSI for the city of Sondershausen, Germany. The subsidence rate was delineated based on ERS-1/-2 data from 1995–2005, ASAR data from 2004–2010, and PALSAR data from 2007–2010. In the PSI deformation maps persistent scatterers located in the urban area are depicted in front of a geocoded SAR image. The colour of the persistent scatterer points indicates the rate of vertical displacement (in mm/year) [113].

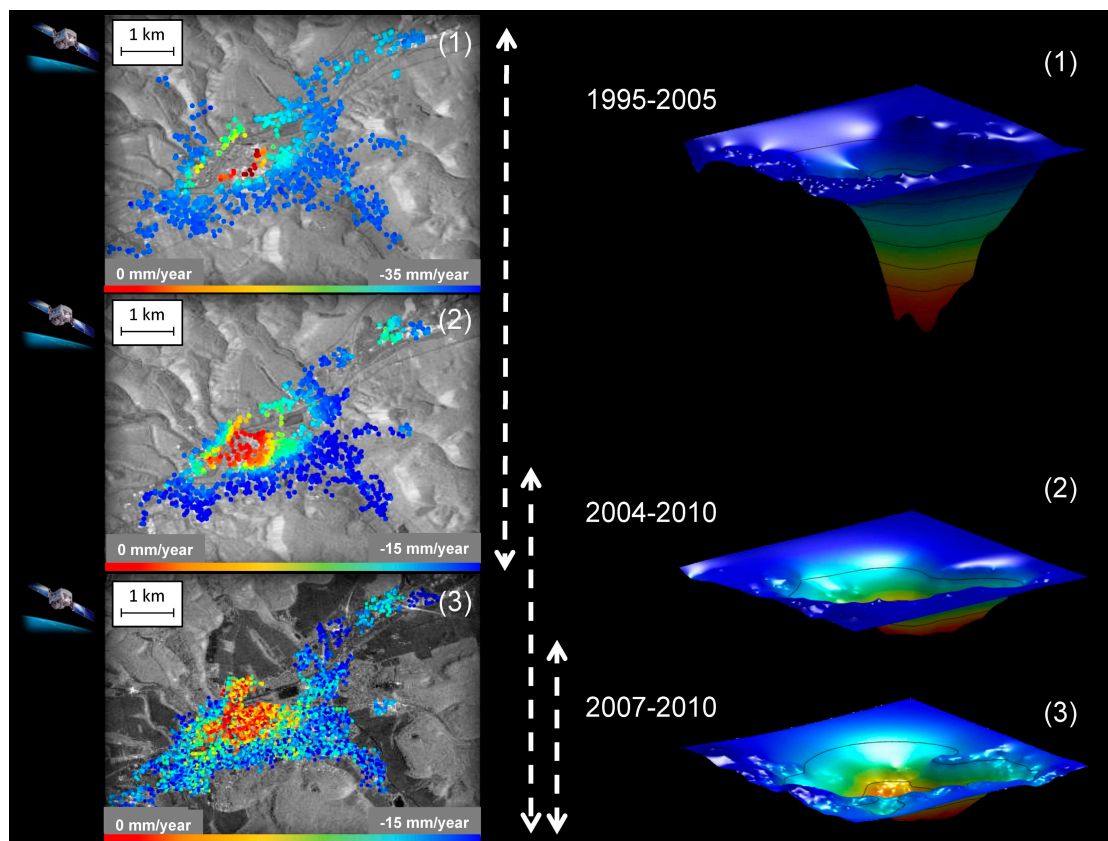


Figure 5. Persistent Scatterer Interferometry PSI reveals subsidence for the city of Sondershausen, Germany. The subsidence rate was delineated based on (1) ERS-1/-2 data from 1995–2005, (2) ASAR data from 2004–2010, and (3) PALSAR data from 2007–2010. In the PSI deformation maps persistent scatterers located in the urban area are depicted in front of a geocoded SAR image. The colour of the persistent scatterer points indicates the rate of vertical displacement in mm/year. Based on the PSI deformation maps (left hand) geometric models of the subsidence were derived (right hand column of figures; modified after Salepci [113]).

2.3. LiDAR and RADAR Altimeters

LiDAR technologies are the most widely used technology to date (from the local to the global scale) for recording the status and changes in geomorphology [114,115]. LiDAR systems actively generate laser pulses (shots) and their respective “echoes” (returns) are registered by a co-mounted telescope. Each pulse illuminates a defined area of the Earth’s surface (a footprint). Therefore, LiDAR systems enable RS information of the terrain and surfaces to be recorded, as well as numerous geomorphic traits along the shot [110,116–118]. The spatial density of the samples depends on the LiDAR system specifications. Recent airborne systems can achieve several measurements per square meter. The point density of LiDAR systems can range from 5–250 points/m² (Figure 6).

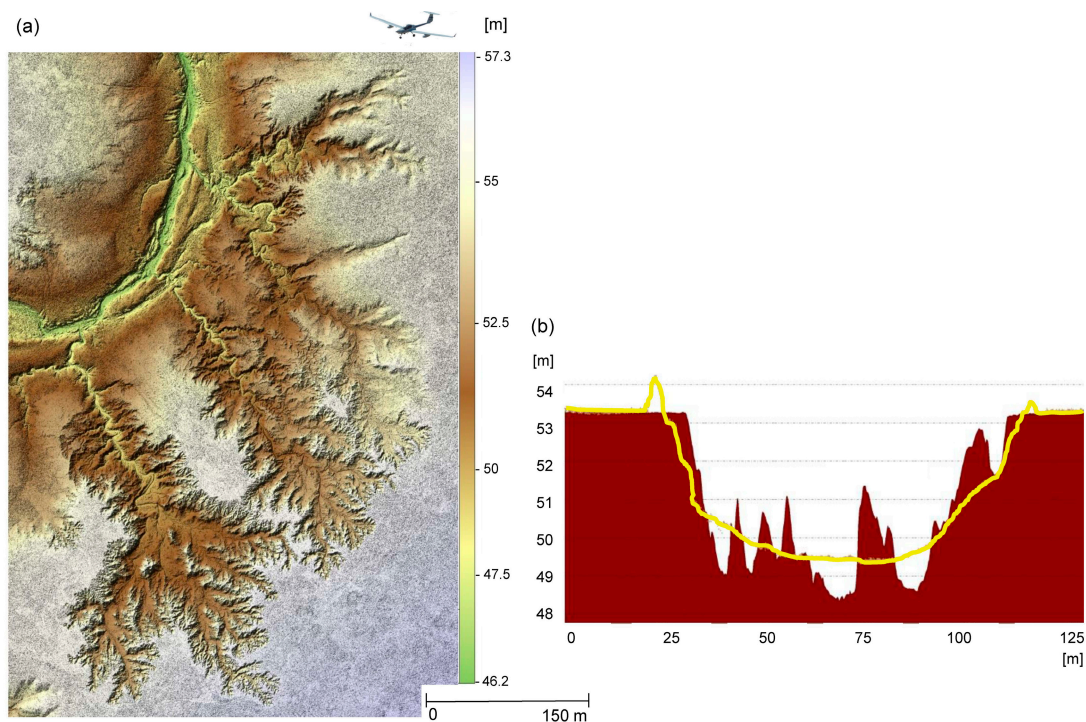


Figure 6. Erosion gullies in Northern Queensland (Australia) represented (a) by a 10 cm-Digital Elevation Model (DEM) derived from multiple overpasses with the RIEGL Q680i-S LiDAR and (b) by cross-sections depicted as solid area and line before and after remediation earthworks, respectively.

Depending on the point density, LiDAR technologies can achieve accuracy in the centimetre range. They are therefore able to derive very high resolution DEMs. Furthermore, in areas with forests, shrubs and single trees, LiDAR technology can penetrate the vegetation and thus provide qualitative and quantitative monitoring of terrain under forest. Another advantage of LiDAR data compared to other RS data is that LiDAR point clouds only cause a small shadow [119], e.g., from trees compared to 20 m pixel image information from Aster sensors or RADAR technologies with a higher geometric ground resolution, which contain the shadow from trees as spectral information in the RS image. LiDAR allows digital derivations of DEMs, textures, contours, slope, curvature, surface roughness, or landslides, as well as numerous other geomorphic characteristics.

There are many different types of LiDARs [71] installed on various RS platforms: the ground-based LiDAR (TLS—terrestrial laser scanner, [120]) and the MLS—mobile laser scanner, the airborne-based LiDAR (ALS—airborne laser scanner, installed on UAVs [121], microlights, and airplanes [114]), and even satellite-based LiDAR (SLS—satellite laser scanner, LiDAR—GEDI-LiDAR [45,122,123], and ICESat-2; [124], Figure 7). Comparatively simple LiDARs are limited to one or two returns per shot, usually the first and last return which typically represent the top of the canopy (first) and the ground (last). In dense vegetation, the last return does not necessarily represent the ground, so special

algorithms are used to identify true ground returns. More sophisticated LiDARs not only record the outgoing and returning discrete pulses, but also the full waveforms [114]. This not only enables more algorithms to be used for monitoring geomorphic characteristics, traits, and changes of that during post-processing of the data to derive point clouds, but the information contained in the waveforms themselves (shape, amplitude, etc.) can be used for further analysis.

LiDAR data of this type together with a wide variety of analytical algorithms and optimally in combination with many more in-situ, close-range, air- and spaceborne RS techniques [125,126] enable the detection and monitoring of geomorphology. Modern full waveform-resolving LiDARs, such as the RIEGL Q1560, Q780, and others, are capable of generating rather dense point clouds, resolving geomorphic and surface characteristics with a resolution as accurate as 10 cm. These LiDARs are typically operated at wavelengths of 1550 nm or 1064 nm. There are even LiDAR systems under development that use several different wavelengths to resolve some spectral characteristics together with point clouds.

The above-mentioned LiDAR systems are usually flown on manned aircraft, including rather small ones. Recently, LiDAR systems have also been developed for small UAVs [121]. Most of the UAV-deployed LiDARs are comparatively simple systems, which do not match the capabilities and the accuracy of the larger LiDARs. One of the main reasons for this is that GPS/INSS systems for UAV do not have the performance compared to airborne GPS/INS technologies. This area is indeed under intense development and new and improved systems are constantly emerging. At this stage, the most advanced and capable UAV-deployable LiDAR system is the RIEGL VUX with its various sub-types [127], including the integrated UAV-RiCOPTER. However, since the UAV can be operated at a very low flight speed with great overlap between the tracks and variable flight altitude, the resulting sample point density can be very high (~250 points/m²). Another feature is the wide scanning angle of the small field of view (FOV) of LiDAR RIEGL VUX-1UAV [128]. 2D–4 D geomorphic characteristics such as the walls of mountains, micro-morphological structures and textures, landslide mapping or the monitoring of soil erosions can be sampled with a high density of pulses [129]. When such systems are implemented, users are able to independently obtain up-to-the-minute DEMs and DSMs, which are of particular importance when attempting to solve specific local and regional issues requiring user-defined spatial and temporal resolution.

The highest precision of LiDAR measurements can be achieved with ground-based TLS systems [120]. Such systems are typically installed on top of a tripod and scan their surrounding area with an accuracy of a few millimetres. The scanning range can be up to 6000 m (e.g., RIEGL VZ-6000). To scan the entire area of interest, a combination of scans from several scanning positions might be necessary. Analogous to UAV-based LiDAR data, TLS data capture vertical structures enabling the delineation of 3D features beyond DSMs or DEMs. The acquisition of TLS data is very time consuming and thus restricted to small areas. There are also mobile laser scanning (MLS) systems, which are basically TLS-systems mounted onto a moving ground-based platform (vehicles, vessels, railcars, even bicycles or pedestrians) [115].

LiDAR systems can also be operated from space. Although capable of providing global datasets, spaceborne LiDAR systems currently have some critical limitations. Due to physical constraints the footprint will always be relatively large (e.g., 50–120 m for ICESat/GLAS; [124,130,131]), which results in inaccurate elevation measurements, in particular in steep terrain. Furthermore, the point density is relatively low (ICESat/GLAS: 175 m spacing along the flight track, 3 km spacing between the three laser beams across the track). The NASA mission GEDI LiDAR (GEDI—Global Ecosystem Dynamics Investigation), launched on 5th December 2018 attempted to overcome some of these limitations. The GEDI Ecosystem LiDAR is a high resolution laser monitoring the Earth's forests and topography from the International Space Station (ISS, <https://gedi.umd.edu/>) [45,122,132]. The footprint has a reduced diameter of 25 m, the along-track spacing of the separate footprints is 25 m, and the across track spacing between each of the ten tracks is 600 m. However, the sampling density will not be sufficient to generate detailed DSMs or DEMs. Small footprint airborne LiDARs overcome this limitation, as they

sample the Earth's surface with a very high level of detail. Unfortunately, global datasets cannot be acquired when reasonable time and expenditure are taken into account.

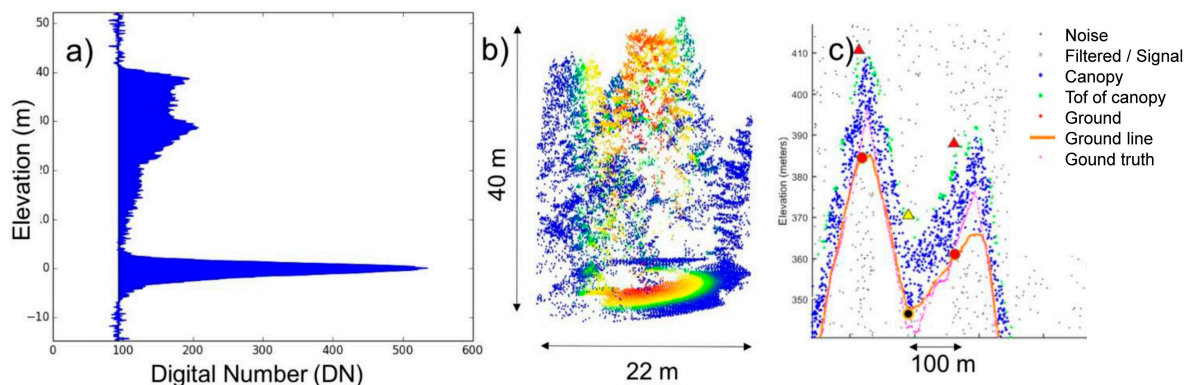


Figure 7. Simulated Global Ecosystem Dynamics Investigation GEDI waveforms (a) are vertical aggregations of point clouds (b) in GEDI sized footprints, which have been modeled to match expected pulse shape and spatial distribution of reflected energy for GEDI. ICESat-2 simulations (c) use degraded point clouds along transects with added background noise. Simulated photon returns are classified as noise, ground, or vegetation returns (taken from Duncanson et al. [132], License Nr: 4856241027296).

RADAR altimeters (RAs) rely on similar functional principles as LiDAR. The RA emits electromagnetic pulses and receives the echo. Based on the traveling time, the distance between the sensor and the surface can be delineated. In contrast to LiDAR, RAs use microwaves. Several satellites were equipped with an RA instrument (e.g., ERS-1/-2, ENVISAT, Sentinel-3). Analogically to small field of view of LiDARs, many RA systems feature the capability of waveform recording and analysis. However, compared to spaceborne LiDARs, spaceborne RAs feature an even larger footprint and a lower sampling density and are thus less suited to generate DEMs or DSMs. The main focus of most RAs is on marine applications, such as sea surface height, wave heights, or wind fields [133].

2.4. Criteria for Acquiring Elevation Data and Surface Data with RS

The criteria for recording and acquiring elevation and surface data using RS can only be briefly mentioned here. Comparative reviews and papers for acquiring elevation data include those of Alganzi [92] and Hawker [134].

2.4.1. Acquiring Elevation Data with RS

Exogenous processes (e.g., weathering, deposition, and the accumulation of rock material through wind, water, ice, and climate change), endogenous processes (e.g., tectonic plate movements, volcanic activity, earthquakes) and their interactions, as well as anthropogenic drivers (e.g., river regulation, coal mining, salt and sand quarrying, or fracking) are structure-forming and lead to the formation and alteration of geomorphic traits, such as elevation, slope, aspect, curvature, and others, of the geosphere. The following factors are therefore essential to acquire digital elevation and surface data and their changes using RS:

- The characteristics and the combinations of exogenous and endogenous geomorphic processes (the scope, length, intensity, consistency, dominance or overlay of the driver) lead to formation of specific geomorphological traits such as geological shapes, patterns, and structures. These process characteristics, in turn, define the characteristics and the accuracy of the monitoring, the possibilities of classification and the acquisition of relief parameters and thus other aspects derived from the topography and physiography like elevation, slope, aspect or curvature.

- Geomorphic trait characteristics, their composition, and configuration, such as the 2D–4 D shape, structure, patterns, density, or distribution of the geomorphic traits and trait variations in space and over time.
- The spatial, spectral, radiometric, angular, and temporal characteristics of the RS sensors (see Figure 8, Table 1).
- The choice of the RS platform that influences the spatial and temporal resolution and ultimately the recordability and precision of the RS sensor properties of the geomorphic traits. With airborne LiDAR systems more accurate derivations of the DEM/DSM can be made compared to with spaceborne terrain RS approaches.
- The choice of the classification method (pixel-based, spectral-based, geographic objects based GEOBIA) and how well the applied classification algorithm and its assumptions fit the RS data and the spectral traits of geomorphology.
- A multi-variate and multi-temporal implementation of RS sensors such as RGB, multi-spectral, hyperspectral, LiDAR, RADAR or microwave radiometer, which not only increase the number but also the characteristics and diversity of traits and trait variations that can be recorded by RS.
- The coupling of in-situ, close range RS (ALS) with air- and spaceborne RS approaches, enabling the optimal calibration and validation of air- and spaceborne RS data.

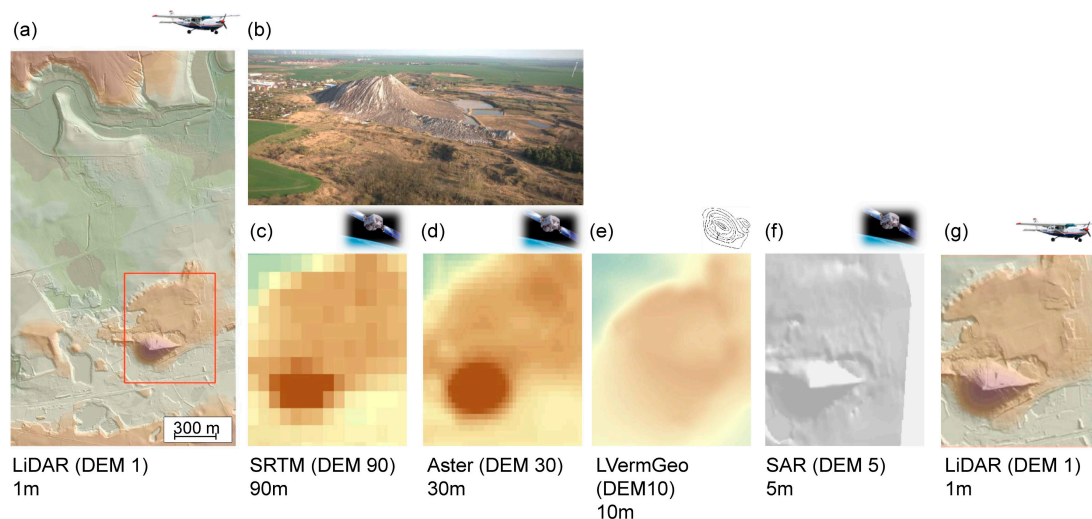


Figure 8. For discrimination and thus for successful monitoring, in addition to the characteristics and the distribution of geomorphic traits and their changes, it is also the spatial characteristics of the RS sensors used that are of major importance—in this case the spatial resolution. DEM comparison of a post-mining potash tailings pile, Teutschenthal-Bahnhof, near Halle, Germany (see also Schwefel et al., [135]), (a) LiDAR (DEM 1)—1 m, (b) photo of the post-mining landscape with a 95 m high potash tailings pile, (c) SRTM (DEM 90)—90 m, (d) Aster (DEM 30)—30 m, (e) DEM generated from height information of the land surveying office—LVerGeo (DEM 10)—10 m, (f) SAR (DEM 5)—5 m, (g) LiDAR (DEM 1)—1 m.

Table 1. Semantic categorization of potentials and practicality of RS platforms and RS techniques for elevation data acquisition; inspired by Mulder et al., [136]: -- = no, - = low, + = medium and ++ = high agreement.

Acqui-si-tion Tech-nique	High Spatial Resolu-tion	Wide Area Coverage	High Temporal Refresh	High Vertical Accuracy	High Complex-ity of Retrieval	Canopy Pene-tra-tion for DEM/(no DSM)	Weather/Il-lumi-na-tion Indepen-dence
Spaceborne Repeat-Pass InSAR	+	++	+	+	+	++	++
Spaceborne Single-Pass InSAR	+	++	++	+	-	++	++
Spaceborne LiDAR	+	++	+	+	-	+	+
Spaceborne RADAR Altimeter	-	+	+	++	-	+	++
Spaceborne Radar-grammetry	+	++	++	+	-	++	++
Spaceborne Photo-grammetry	+	+	+	+	-	-	-
Airborne InSAR	++	+	-	-	+	++	+
Airborne LiDAR	++	-	-	++	+	+	-
Airborne Radar-grammetry	++	-	-	+	+	++	+
Airborne Photo-grammetry	++	+	-	+	+	-	-
UAV-borneLiDAR	++	-	++	++	+	++	+
UAV-borne Photo-grammetry	++	-	++	++	-	-	-

High spatial resolution: ++ High [0.1–0.5 m], + Medium [0.5–50 m], + Low [50–500 m]. **Wide area coverage:** ++ Wide [$>1000 \text{ km}^2$], + Medium [$<1000 \text{ km}^2$], + Small [$<100 \text{ km}^2$]. **High temporal refresh:** ++ High [$<1 \text{ day}$], + Medium [$<1 \text{ week}$], + Low [$<1 \text{ month}$]. **High vertical accuracy:** ++ High [$<1 \text{ m}$], + Medium [$<2 \text{ m}$], + Low [$<5 \text{ m}$]. **High complexity of retrieval:** ++ High [expert level], + Medium [advanced level], + Low [beginner level]. **Canopy penetration for DEM, (no DSM):** ++ High [ground visible], + Medium [ground partly visible], + Low [ground invisible]. **Weather/illumination independence:** ++ High [full independence], + Medium [partly independent], + Low [no independence].

2.4.2. Acquiring Surface Data on Vegetation and Urban Structures

In addition to the aforementioned criteria, others also need to be taken into consideration when recording surface data using RS. To record geomorphic traits such as the DEM, structure-forming traits (i.e., structure, diversity, gradients of relief structures) play a decisive role in discriminating and deriving relief parameters.

To derive surface elevation such as the height of vegetation as well as structural traits (i.e., the height of buildings, bushes and trees) other spectral traits of the vegetation (e.g., chlorophyll content, xanthophyll, morphological and phenological plant traits, or 2D–4 D traits of the vegetation height) can also be used for discrimination. In this way, plant species, plant communities or the characteristics of vegetation diversity can be monitored using RS, when their spectral biotic traits differ in time or space.

Urban surface structures on the other hand can be distinguished by the characteristic 3D geometry of the building height or building characteristics (i.e., roof incline, building geometry), which can be recorded either by LiDAR or RADAR RS technologies. In addition to recording 3D buildings, TIR, multispectral, or hyperspectral RS technologies can be used to detect other traits such as the characteristics of buildings, the degree of sealed surfaces and other aspects. Comparative reviews and papers on the acquisition and discrimination of plant species [137], the monitoring of vegetation diversity [54,138], forest health [139,140], as well as anthropogenic structures and traits [141,142] are all important in this context.

Since various DEMs/DSMs derived from different RS technologies are already available, Table 2 shows the numerous studies assessing the accuracy of DSM's, whereas Table 3 summarizes the specifications of output DEMs of the RS technologies. Table 4 then goes on to provide an overview of RS-assisted derivation of terrain and landscape surfaces and its traits (Table 5).

3. Aeolian Landforms

There is a very strong connection between the global anthropogenic impacts of the 21st century (climate change, land use intensity, deforestation and urbanization) and increasing desertification, sand storms, wind-, water-, and soil-erosion, all leading to the degradation of large areas of the Earth's

surface [143,144]. Dune landscapes cover vast areas of the Earth's terrestrial surface and as a result of desertification are showing an annual increase of 70,000 km² [145]. The increase in human-induced soil degradation is even stronger, equating to 1964 million hectares in the world [143,146]. Desertification processes not only lead to changes in geodiversity but also threaten biodiversity and major ecosystem services [143]. "The loss of our soils is thus one of the greatest crises of our time" [147].

The Earth's surface is constantly shaped by wind, which leads to the discharge, deflation, erosion, transport, turbulence, saturation, collision as well as the sedimentation and accumulation of fine particles of different sizes and properties [148]. The type and characteristics of aeolian changes are determined by the following factors: (i) weather conditions such as consistency, continuity, intensity, extend or wind direction (wind force, rolling or sliding (creeping), the Bernoulli effect of winds—(lift), bouncing (saltation) and the impact of one particle upon another, as well as (ii) aeolian traits such as size, shape and biochemical-biophysical composition. However, RS approaches influence the discrimination and the monitoring of aeolian geomorphic traits, due to (iii) the properties of RS technologies: the spatial, spectral, radiometric, temporal and angular resolution, as well as the RS platform and the classification strategies selected for monitoring (see also Section 3).

This is an extremely complex procedure to monitor and assess wind erosion and degradation processes in landscapes. An indicator complex comprised of agro-ecological indicators (i.e., surface soil texture, foliar cover, litter and rock fragmentation cover, biological soil crusts, canopy height and 3D geometric growth form), air characteristics, and quality indicators (i.e., visibility, or PM_{2.5} concentration) as well as model calculations (soil moisture or net soil loss or surface) must be included in the modelling when monitoring and assessing wind erosion. Here, it becomes clear that "the quality of ecosystem models is only as good as the quality and/or degree of uncertainty of the model's input data" [42].

Originally, the monitoring of aeolian land forms started with the combined use of in-situ measurements (sand traps, meteorological/geochemical measurements) and model calculations [149]. Nowadays, with its different sensor characteristics and various platforms, RS is an essential technology for monitoring aeolian structural diversity [150] (see also Table 5). With the implementation of RS, numerous geomorphic diversity characteristics are used, i.e., the spatial-temporal patterns of dunes (length, minimum spacing density, orientation, height and sinuosity, [151,152], the composition and configuration of aeolian dune patterns i.e., the complexity, diversity, shapes, patterns and heterogeneity based on Landsat and SRTM RS data [153] or multisensory data using Landsat-7 ETM+ and data from Digital Orthophoto Quarter Quadrangles (DOQQs) [154]. Mechanisms that lead to the history of aeolian patterns based on RADAR have been monitored by multiple complementary RADAR RS sensor complexes (SIR-C imaging, SRTM interferometry-derived elevations and RADAR sounding or ground penetrating RADAR (GPR)) [155]. Other essential RS technologies are also available to assess the volume and changes or intensity of sedimentation or dune migration [150]. Although numerous papers have provided reviews or detailed insights into dune landscapes, few papers have actually discussed the spatial distribution and thus the characteristics of geomorphic structural diversity, which is imperative for understanding dune landscapes [156]. The reason for this is that as patch mosaics and different patterns, aeolian land forms induce very distinct geomorphic characteristics and consequently specific morphometric traits, patterns, and functions, which are the outcome of turbulences, changes, and disturbances in ecology [157,158].

Digital photogrammetry using aerial images was the first method for assessing dunes and their movements [159]. Nowadays, various optical (i.e., Landsat, Sentinel-2) as well as RADAR RS technologies such as SRTM are implemented not only to understand geo-ecological relationships and their complex effect mechanisms and interactions of dune ecosystems, but also to investigate spatio-temporal dune patterns, their migration or processes, and the spreading of desertification [143,152,160]. In fact, multispectral and multi-temporal RS approaches are increasingly being used to record a number of aeolian traits such as spatial-temporal dune-field pattern characteristics (i.e., length, minimum spacing density, orientation, height and sinuosity) [150].

LiDAR RS technologies have been successful due to their tremendously high spatial resolution and recording of 2D–4D aeolian structural traits with a high degree of precision detail when monitoring the disturbances of aeolian land forms [161]. The high-precision 2D–4D monitoring of aeolian structural traits opens up a whole new understanding of modelling, assessing and predicting complex relationships and interactions of geodiversity and biodiversity, their changes, disturbances and resilience [162,163]. The special features of LiDAR technologies are the monitoring of 2D–4D dune activity, spatial-temporal dune patterns and hierarchies, as well as extra-terrestrial dune formations [164].

One of the greatest challenges in aeolian monitoring using RS is the spatio-temporal recording and delimitation of highly dynamic dune migration as well as subtle changes that occur on the surface due to transported sand. The implementation and the connection of airborne, spaceborne (LiDAR, optical and RADAR) with high-frequency spatial and temporal close-range terrestrial laser scanning (TLS), as well as in-situ measurements will enable an almost continuous monitoring and assessment of 3D–4DD dune dynamics and morphology, their interactions and geomorphic activity, helping to understand continuous surfaces over longer periods of time [165].

Due to the technological capabilities of LiDAR (i.e., the penetration of vegetation, see Section 4), it is currently the only technology that can be used, for example, to monitor remaining historically preserved migrating sand dunes that are situated under vegetation such as forests (see Figure 9).

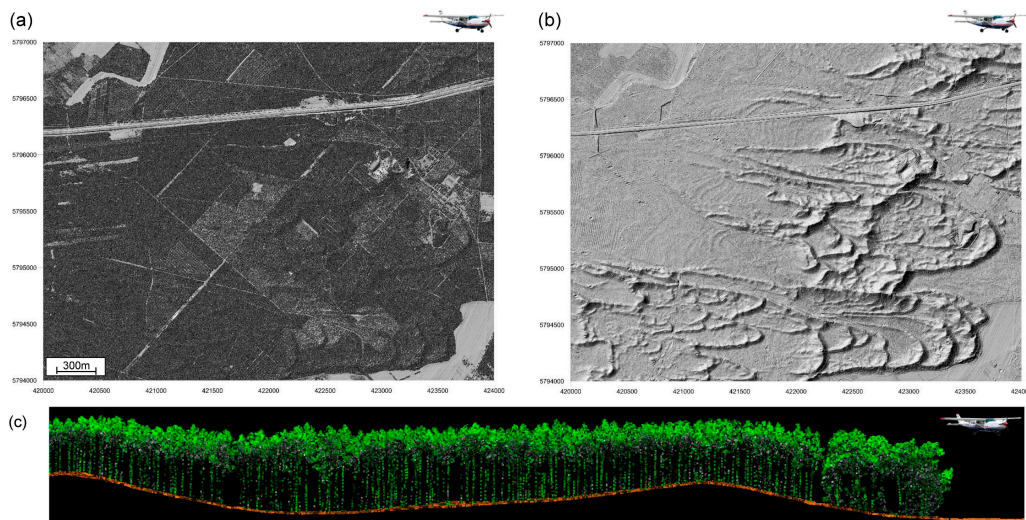


Figure 9. Walking dune near Königs Wusterhausen, southeast of Berlin (Germany) depicted (a) as Digital Surface Model (DSM), (b) a Digital Elevation Model (DEM) as shaded relief, and (c) as a 3D Profile view of the DSM whereby of the dune surface appears orange and the forest vegetation green. The data basis was generated by Airborne Laser Scanning (ALS) with a RIEGL-LiDAR (point density >5 points/m²) carried by airplane.

4. Fluvial Landforms

Fluvial landforms are the product of flowing water accumulating in creeks, streams and rivers. This includes to changes in or the formation of terraces, sediment deposits, river beds, floodplains and river valleys. Fluvial systems typically have a large inherent diversity. As a geomorphic driver, a river is able to sort particle sizes of soil and gravel by different flow velocity, and to abandon channels to establish new types of ecosystems. Therefore, fluvial landform systems are highly complex and extremely dynamic from a geomorphological perspective [166,167]. However, the resilience of rivers is not only altered by natural processes and interactions (i.e., water, sediment, geology, soil, and vegetation), but also increasingly by the complex interactions between natural and anthropogenic drivers and impacts, which can ultimately tip the ecological balance (see changes in rivers feeding the Aral Sea) [168].

Water engineering measures such as river relocation or the straightening of rivers, the reduction of retention surfaces, drainage, land use intensity and urbanization all lead to tremendous changes and disruptions to surface and subsurface runoff. The consequences are immense: an increased risk of flooding, erosion, and sedimentation in streams and rivers, leading to changes and disturbances in biodiversity, entire ecosystems, and the self-purification function of water. According to Grimaldi et al. [169] flood events are the “most frequent, disastrous and widespread natural hazards of the world” (see also [170]). Every year some 20,000 people die as a result of flood events [171]. From 1995–2015 alone, ca. 109 million people were affected by flood damage, amounting to costs of around USD 75 billion per year [172].

Due to the very complex and highly dynamic nature of river systems, their forms, meandering processes, sedimentation processes and water quality have been successfully recorded for some time now using various RS technologies. These observations allow important considerations to be drawn about different disturbances such as water pollution, river straightening, bank protection measures, or the intensification of land use. However, considerations can also be drawn for example about disturbances or changes in surface runoff after heavy rainfall [173–176]. For the monitoring of fluvial systems using RS, GIS and topographic information, in-situ measurements as well as close-range and air- and spaceborne RS technologies are often used in combination with one another. The detailed object based classification of morphology forms using LiDAR data and the classification of hyperspectral data shows the distribution of heavy metal content in soils and vegetation in flood plain areas [177–179]. Various sensor technologies are implemented for this purpose such as digital cameras, video cameras, heat-, infrared-, hyper-, and multispectral sensors, RADAR, and LIDAR [167,168,180] (see also Table 5). In this way Pekel et al. [181] were able to impressively show global surface water distribution and its long-term changes using global time series RS data (Landsat-5 TM, -7 ETM+, and -8 OLI). In the face of climate change the monitoring of global surface water distribution as well as changes and disturbances to it, will become a highly relevant topic.

Aerial photos of rivers and floodplain geomorphology were the first RS technologies to record fluvial landforms [182]. The first RADAR technologies [183] as well as optical RS sensor systems like Landsat [184] were early applications that monitored the irrigation and drainage systems of areas as well as the first morphometric characteristics of river systems. Landsat and other spaceborne data are also widely used to analyse river morphology and morphodynamics, such as meandering and avulsions [185], as well as to monitor decadal length changes in the fluvial planform of rivers [186] (see also Section 4.2). Due to the unique characteristics of RADAR technologies (24-h and all-weather capability) as well as their ability to record flood events, RADAR RS is a crucial resource and technology for the mapping and prediction of flood events, and as a basis for geo-hydraulic modelling data [169,187,188].

On finer spatial scales airborne LiDAR-RS deliver crucial 3D–4D information with a very high degree of detail for geo-hydrological modelling (see also Section 4.3), which is essential for the successful mapping and monitoring of fluvial systems [161].

4.1. Flood Events and Floodplain Risks

RS plays a crucial role in recording, assessing [189], modelling, and forecasting [190] flash floods and flood hazards, in assessing their vulnerability, and in the valuation and prediction of flood risks in riverine landscapes as well as coastal areas as a consequence of extreme events such as monsoons, tsunamis or hurricanes. For these purposes, a number of optical RS sensors are used such as Landsat, Sentinel-2 [191], RADAR technologies such as ASAR, ENVISAT, TerraSAR, or RADARSAT, Sentinel-1 [177,192], as well as airborne LiDAR systems [42] (see also Table 5).

To investigate the effects and the resilience of fluvial landforms to anthropogenic disturbances such as mining or water engineering measures, multi-source information is often used comprising of historic maps, aerial images, digital orthophotos, and different RS sensors on various platforms. Ghoshal et al. [193] proved for example through bathymetric surveys that fluvial systems recovered

over a century from the damage caused by hydraulic mining operations (1853–1884) in Sierra Nevada in California. In fact, they found that the fluvial processes investigated from 1906 to 2006, erosion, sedimentation, redistribution of sediment, as well as volume changes, led to a stabilization of the river ecosystem. During the course of the recovery process, channels of up to ~13 m cut into the mining sediments. These fluvial processes led to a drastic reduction in the local flooding incidence in the region.

Certain fluvial traits are known to play a crucial role in flood hazards and inundation modelling, such as the DEM and derived data like elevation, slope, curvature, the stream power index (SPI), the topographic wetness index (TWI), distributed roughness values, land use land cover (LULC) information, river density, distance to rivers, or different plant traits, such as phenology or plant density, that can be derived from various technologies [192].

RADAR and LiDAR are the most common RS technologies implemented for the mapping and monitoring of flood events. In fact, it was the use of RADAR that revolutionized the monitoring of flash flood hazards [194]. Costache et al. [195] conducted research on flash flood susceptibility assessments using multi-criteria decision making and machine learning approaches based on SRTM- and GIS techniques. With the open access of the RS time series for Sentinel-1 data these techniques are now widely implemented for flood detection and mapping [192,195,196]. Such techniques enabled the morphological characterization of the Kyagar glacier and the monitoring of glacier lake outburst floods based on a time series in 2018 Sentinel-1A data [197]. To monitor permanently and temporarily flooded coastal wetlands, multi-temporal ALOS PALSAR-1 data have been used [198]. If various RADAR sensors with different sensor specifics are implemented, then more fluvial traits can be investigated and the weaknesses of the sensors can offset each other. Hong Quang et al. [199] used hydrological/hydraulic modeling-based thresholding of multi SAR RS sensors (Sentinel-1) to monitor floods in regions of Vietnam's Lower Mekong River Basin. Alsdorf et al. [200] used InSAR technologies to measure water level changes on the Amazon floodplain. For high resolution flood monitoring an integrated methodology also used passive microwave brightness temperatures and Sentinel SAR imagery [201]. Furthermore, in a study by Grimaldi et al. [169], SAR RS information was not only used for mapping flood events without vegetation cover, but also for recording flood irrigation under vegetation. This study very impressively illustrated the wide application range for fluvial remote-sensing technologies.

In addition to RADAR RS information various optical RS data, i.e., Landsat, Sentinel-2, RapidEye, or WorldView, are used for mapping floods [174]. Wang et al. [202] were able to demonstrate an efficient method for mapping flood extent in a coastal floodplain based on Landsat-5 TM and DEM data. Furthermore, geomorphic changes in the Jhelum River following an extreme flood event were recorded in a case study using Landsat-8 OLI data [203]. With the help of time series Landsat-8 OLI imagery data and the integration of stream gage data, it was also possible to monitor the surface water extent in Central Valley in California [204]. There are many more studies using multitemporal Landsat data to map flood hazards over different time intervals [205]. Due to the improved spatial-temporal resolution of Sentinel-2 data, these are also being increasingly used for mapping flood events [206]. Sentinel-2 satellites provided a near real-time evaluation of catastrophic floods in a case study in the western part of the Mediterranean [207]. In another study of Ras Ghareb city in Egypt, Sentinel-2 data and fuzzy analytic hierarchy process approaches were also used for monitoring and assessing urban flash flood impacts [208]. In their case study of winter wheat fields in a semi-arid region, Olivera-Guerra et al. [209] showed irrigation retrieval from Landsat optical and thermal data integrated into a crop water balance model.

In spite of numerous existing and future spaceborne optical and RADAR missions to monitor the fluvial morphology and assessment of flood hazards, LiDAR data are increasingly becoming an essential basis for recording detailed 2D–4D spatial-temporal geomorphological-hydrological information and for hydraulic analysis and modelling [161,210]. Webster et al. [211] used topographic LiDAR to map the flood hazard from storm-surge events for Charlottetown on Prince Edward Island

in Canada. Moreover, numerous research papers have been based on the use of high-density LiDAR data, often in combination with 2D streamflow hydraulic modelling using high-density LiDAR for mapping high accuracy urban, river or coastal flood risks [212–215]. Morrissey et al. [216] used LiDAR data for modelling groundwater flooding in a lowland karst catchment. Furthermore, an increasing number of combinations and the linking of different sensors and RS platforms have been used to monitor flood events, e.g., web cameras with airborne LiDAR RS data [217]. Due to a high degree of flexibility with comparatively low costs, an increasing number of different RS sensors are being used on UAV platforms for monitoring floods [218,219].

In their research, Kulp and Strauss [42] were able to prove just how important sensor characteristics are for the quality of a model to predict flood risk. It goes without saying that models and model predictions are only as good as the quality of their input data. With the implementation of airborne LiDAR and calculations from a detailed DEM of coastal regions Kulp and Strauss [42] were able to prove that more than three times as many people are threatened by climate change and rising sea levels than was previously assumed based on models using SRTM DEM data.

4.2. Fluvial and Tidal Channel Migration

Channel “migration rates are key to understanding biogeochemical fluxes” [220], and are thus important indicators for water quality, the climate, and ultimately biodiversity. Natural channel migrations are episodic and dynamic processes on large spatial and temporal scales. Consequently, the monitoring and assessment of the river conditions, rates of change and in particular the assessment of resilience of river systems (especially after water engineering measures), has to be the kind of monitoring that incorporates all spatial-temporal scales of geomorphic organization. This not only enables a better geohydrological understanding of driving forces, processes, and interactions, but also facilitates a targeted and successful river management.

For some time now aerial image sequences as well as multispectral and multi-temporal RS technologies have been used to monitor the status, changes and disturbances of fluvial and tidal environments, channel migration and many other fluvial traits (see Table 5) in the context of different driving forces [168,174,221,222]. Preliminary research on this topic conducted by Garafalo [223] investigated the influence of wetland vegetation on tidal stream channel migration and morphology by using photogrammetric techniques over a period of 32 years (1940 to 1972). This research calculated an average relative channel migration rate of 0.21 m per annum for salt marsh tidal channels and 0.32 m per annum for freshwater tidal wetland channels. Using the time-series of aerial photographs and topographic information, the temporal evolution of natural and artificial abandoned channels of the River Rhône were analysed along with its controlling factors in a multi-pressure river system over a period from the mid-19th century until the beginning of the 20th century [224].

With the opening of the Landsat archive, the time series of Landsat RS data (multispectral and TIR) has become a crucial data source for monitoring fluvial geogenesis, fluvial taxonomy, and fluvial functionality. Yang et al. [225] used the time-series of Landsat-5 TM data over a 19-year monitoring period for the Yellow River Delta in China. This covered fluvial traits such as the channel position, systematic changes to river banks and mid-channel bar dynamics and compared fluvial channel characteristics and migration in relation to the intensity of both natural and anthropogenic changes (i.e., from water engineering). Other research work on river- and channel migration, mid-channel bar dynamics, and channel stability assessment based on Landsat time-series has been conducted by [226–229].

Finotello et al. [222] were able to derive a number of other morphometric traits such as sinuosity, intrinsic wavelength, curvature and the asymmetry index from Landsat time series data to characterize meandering patterns and meandering dynamics in tidal and fluvial environments. Sentinel-2 RS data have also been successfully implemented to characterize bankfull discharge and bankfull channel geometry indicators (width, depth, and longitudinal channel slope) of an alluvial meandering river system. RS information are the basis for their morpho-dynamic model that models fluvial processes like balancing bed sediment or bank and floodplain processes over the entire flow duration curve.

Naito and Parker [230] also showed the spatiotemporal change of bankfull channel characteristics from randomly set initial conditions to an equilibrium state at which there is no more change in either space or time.

RADAR RS is extensively used to record fluvial and tidal channel characteristics, their traits and migration processes [174]. Bhaskar and Kumar [231] used SRTM RS data to monitor channel migration processes in the Thengapatnam coastal tract bordering the Arabian Sea. With the help of SRTM and in-situ information they were able to demonstrate that the loss of river meander was caused by a relative elevation of the land surface or a lowering of the sea level. Lelpi et al. [232] used SRTM RS data to investigate the relationships between the incidence of floods and the speed of change to the channel migration rate in arid regions. They achieved this by combining the data from discharge records with channel migration rates, dynamic time-warping analysis, and chronologically calibrated subsidence rates derived from RS data. Their results showed a slight decrease in the discharge pattern of the Mojave river downstream, contradicting the results from previous studies that demonstrated an increase in the discharge patterns of comparable river systems. Furthermore, their results showed that ephemeral rivers in arid regions can show a previously unknown margin for maintaining hydraulic geometries in stratigraphic sequences. A number of other studies also used RADAR data such as SAR data to characterize fluvial channels [233]. To estimate river discharge, not only optical, but also RADAR altimetry RS data have proven to be particularly suitable such as ENVISAT, Jason –2 and –3, Sentinel-3A, CryoSat-2, and AltiKa satellite altimeters RS data [234]. Various morphometric traits, such as water velocity [235], river width [236], or water height measurements, have also been recorded using RS technologies [237].

Airborne LiDAR technologies, usually in combination with other sensor types i.e., hyperspectral, RGB or TIR RS data in terms of deriving numerous hydraulic geometric traits enable a number of fluvial channel migration characteristics and process rates to be recorded such as grain characteristics, grain and gravel size, shape or roundness. A detailed overview of the detection and characterization of fluvial traits, e.g., grain characteristics, grain, and gravel size, shape, or roundness among others, using LiDAR technologies is provided by [161,168,174](see also Figure 10).

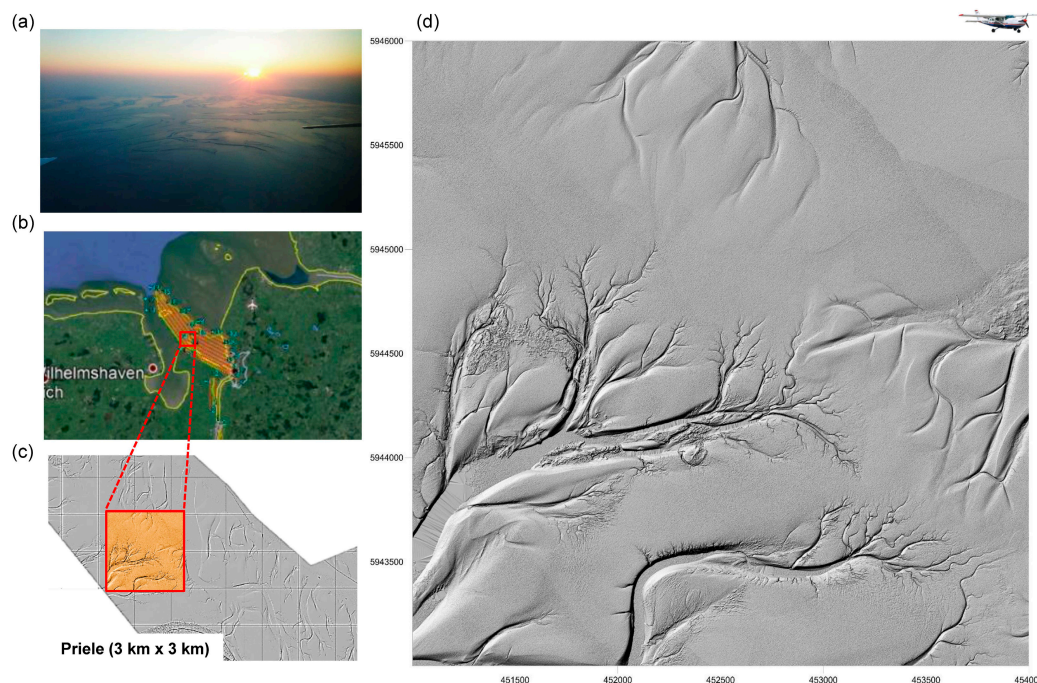


Figure 10. Tideways in the Weser river, northeast of Wilhelmshaven, Germany: (a) Photo of the tideways acquired from the airplane. (b) Location (Google Maps) of the monitored area (in orange) (c) Digital Elevation Model (DEM) created by Airborne Laser Scanning (ALS) with a blue rectangle (>5 LMW/m²), highlighting the location of the (d) 3×3 km tideways displayed as shaded relief (elevation of the contours $Z = 20$).

4.3. Stream Bank Retreat

The degradation of stream bank is caused by a combination of subaerial erosion, river erosion trees fall as well as river bank slides. Specific local geological conditions, land use intensity, and their characteristics, the flow regime, as well as the hydrological characteristics of the river catchment also play a crucial role in this respect. The significance of morphological and biological characteristics and the conditions of the riparian zones and disturbances to them through river bank deterioration in the formation of retention zones have long been ignored. For some time, attempts were made to reduce riverbank migration in agricultural from agricultural and urban areas. Stream bank retreat plays a major role in hydrodynamic processes, flows, the preservation of water purification processes, and consequently in the preservation of water quality. It has been proven that rivers with vegetation as opposed to rivers without vegetation lead to a ten-fold deceleration of river meander migration and ultimately to an improvement in the water purification process [220]. Furthermore, bank erosion processes can also monitored with UAV-SfM RGB technologies along complex bank lines of a straight mid-sized river reach [238].

4.4. Flood Hazard

The significance and selection of suitable RS data play a decisive role in how accurate model projections will be for potential areas of flooding. This has already been extensively described (see also: Flood events and floodplain risks using RS, [42]). A study by Micheli and Kirchner [239] used aerial photos to monitor and assess the effects of wet meadow riparian vegetation on stream bank erosion and on stream bank migration and erodibility over a 40-year period (1955–1995). Heeren et al. [240] used the time-series of RGB-data (2003–2008) for the monitoring and assessment of various geomorphic traits of stream bank retreat. A combination of terrestrial and airborne LiDAR with high spatial resolution RS–RGB data are crucial RS technologies for monitoring and assessing stream bank conditions [168,174,241]. UAV-based laser scanning in combination with other sensor technologies have also been used increasingly more for monitoring and modeling riverscape morphometric and vegetation traits [242–244].

4.5. Coastal Landforms

Coastal geomorphology describes the dynamic interface between the ocean and land surfaces. Based on hydrological, lithological and morphological criteria, seven different types—i.e., small delta, tidal system, lagoon, fjord and fjärd, large river, tidal estuary, ria, karst as well as arheic [245]—of coastline can be distinguished, which can be recorded using RS methods (see also Table 5). Since the different types of coasts filter the water differently, the ecosystem services of different coastal types can be recorded and evaluated based on RS methods. Coasts experience such high dynamics due to the continuous motion of waves, making them a crucial driver for hydromorphological processes such as transport, erosion, or sedimentation. The monitoring of changes or disturbances to coastal geomorphic traits play an important role, particularly in the context of climate change with the rising of sea levels, a growing world population and the settlement of coastal areas. Current studies show dramatic changes to the coastline, whereby half of the world's beaches would disappear by 2100 [246]. In this study, various RS sensor technologies, i.e., optical, RADAR, and LiDAR (Figure 11), were implemented to record shoreline erosion-accretion trends [247]. Both Allen and Wang [248] and Green et al. [249] provide a crucial overview of feasible RS approaches to monitor coastal changes and retreats, the patterns and erosions of coastlines or changing sea levels by nearshore bathymetry and refer to tools for coastal protection. A UAV overview of how RS is implemented for coasts is provided by Klemas [250].

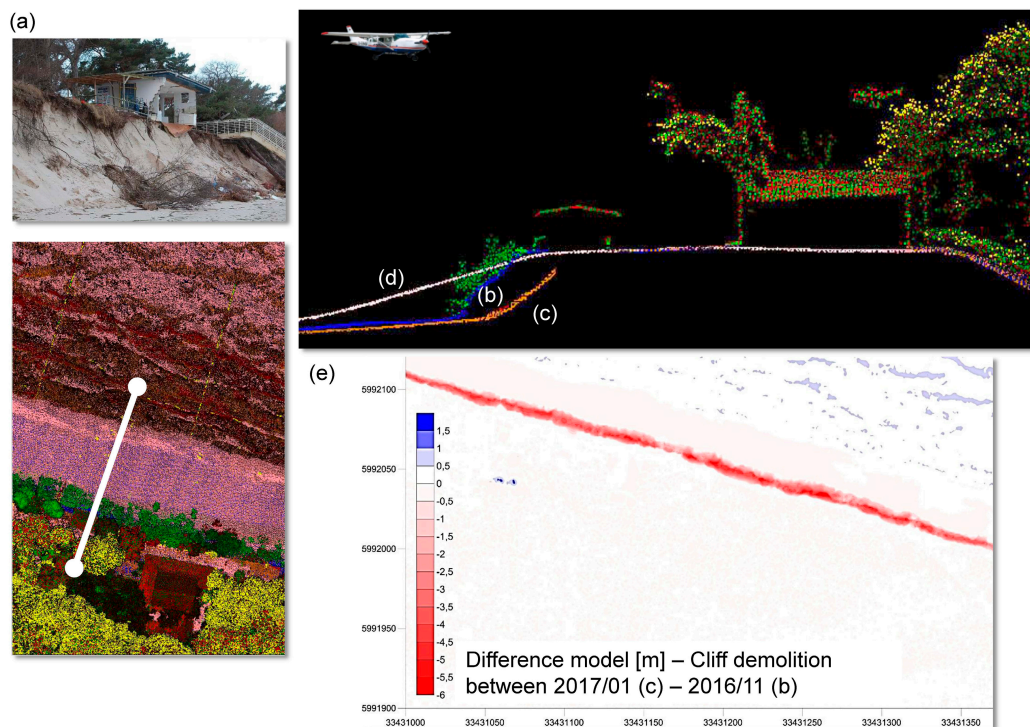


Figure 11. (a) Cliff demolition of an area of the outer coast, Zemplin Fule (Germany): (a) Photo of the cliff depicted in 3 D profile view of a Digital Terrain Model (DTM) and a Digital Surface Model (DSM) that were created by Airborne Laser Scanning (ALS) in (b) 11/2016, (c) 1/2017, and (d) 7/2019. (e) Difference model [m] of the cliff demolition between 1917 and 1916.

RS approaches with partially high temporal (several days) as well as spatial resolution (<1 m) can monitor changes to the position and configuration of coastal landslides on various spatial scales, assess their condition and consequently provide crucial predictions about populated and built-up areas. This is how Moore and Griggs [251] used methods of airborne photogrammetry for monitoring the long-term cliff retreat and erosion hotspots along the Monterey Bay National Marine Sanctuary from 1953–1994. They ascertained an average retreat rate of 7–15 cm/year, but additionally identified episodic hot spot rates for the coast of up to 20–63 cm/year. Time series from Landsat-5 TM and -8 OLI are ideally suited for a geospatial assessment of several decades of coastal changes or ebb-tidal delta migration [252,253]. With the help of Google Earth Engine or other cloud-based RS platforms, one is able to quickly and cost-effectively integrate extensive RS time series data into the mapping of coastal geomorphological changes and consequently make important predictions about changes [254]. Some studies such as those by Kawakubo et al. [255] investigated the influence of various biogenous and geogenous traits i.e., vegetation, water or soil traits on the geomorphic changes of coastlines in south-eastern Brazil using segmentation techniques based on TM and ETM+ data. Other works have also focused on assessing channel stability in the lower reaches of the Krishna River (India) using multi-temporal satellite data over the period 1973–2015 [256]. Various RADAR approaches have developed semi- or fully automated classifications and filter techniques and strategies for mapping the processes and changes to coastal geomorphology based on RADAR imagery such as SAR over longer time periods [257,258]. In this respect, LiDAR techniques are probably one of the most important RS technologies to investigate 2–4D morphometric changes of shorelines, coastal dunes, landslides, coastal cliffs or subsidence [161,246,259]. This technology in particular portrays the extremely high temporal and process dynamics of the transformation in coastal regions through erosion and sedimentation processes in the coastal environment, even over short periods of time. For this reason, developments in the implementation of spaceborne GEDI-3D LiDAR are imperative for successful global coastal monitoring.

5. A Summary of Future RS Technologies and Existing Data Products for Monitoring Geomorphological Forms and Traits Relevant to Biodiversity

This section provides a short overview of future RS technologies as well as existing data products, especially with respect to the Tandem-L mission—a mission proposal suggesting two L-band (~24 cm wavelength) SAR satellites in helical formation flight [46] (see also Table 6). This tandem formation enables single-pass interferometry and thereby 3D imaging of the land surface. Hence, a DEM will be generated that is similar to the operational TanDEM-X formation. However, with Tandem-L a global high-resolution DEM will be produced every year as opposed to only twice in the mission's life time as is the case for TanDEM-X. This is enabled by cutting-edge SAR acquisition technology including digital feed arrays combined with a mesh reflector as well as signal recoding using digital beamforming [46]. The application of L-band waves, instead of X-band (~3 cm wavelength) makes transmission through vegetation possible. This allows the creation of a DEM despite distinct vegetation cover where TanDEM-X products would rather serve as a DSM (or intermediate-height model) due to limited vegetation canopy penetration at the X-band. Geomorphology mapping with Tandem-L relies on annual and global DEM analyses, allowing dynamic (inter-annual) surface processes to be monitored. Hence, vertical soil processes (subsidence, dolines, uplifts, as well as cryo- or bioturbation) as well as topographically induced soil movements (solifluction, soil drifts, mud- and landslides, rock fall) can be assessed and monitored in unprecedented quality and quantity. Figure 12 shows important current and future RS missions and sensors to derive the status and changes of geomorphology, whereas Table 7 shows a selection of RS-aided data products for monitoring terrain, surfaces and fluvial landform data products.

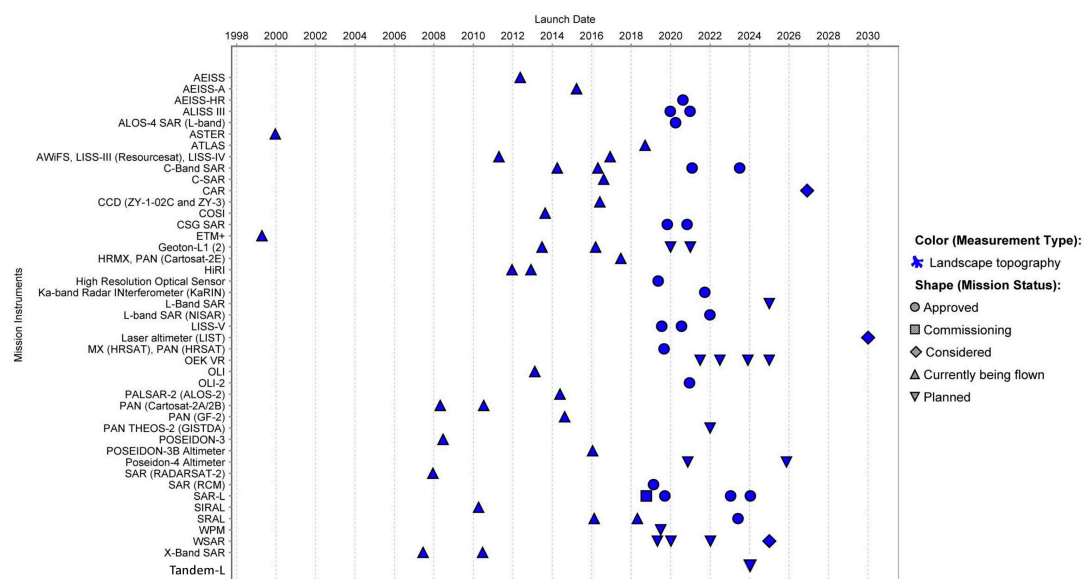


Figure 12. Current and future spaceborne RS mission instruments for monitoring landscape topography with information about the mission status, according to the CEOS database [260].

6. Conclusions and Outlook

Geodiversity controls biodiversity: Geodiversity is the promoting, controlling, regulating, and limiting factor, as well as the most important for landscape processes, and thus a decisive factor for biodiversity. Therefore, biodiversity can be regarded as the result of geodiversity as well as its interactions, disturbances and alterations, implying that a successful conservation of biodiversity primarily entails the conservation of geodiversity.

Therefore, the adequate recording of geomorphology as a crucial part of geodiversity is an important element in monitoring the state, changes and disturbances to geo- and biodiversity, ecosystem vulnerability as well as ecosystem integrity [1,9,261] and one of the greatest impacts and thus challenges of the 21st century. Many aspects of geomorphic diversity are changing rapidly due to

anthropogenic factors (e.g., mining of rare metals, terracing, sand extraction, construction, sea-floor trawling, training of rivers, dams, water-table lowering). This is highly relevant at the science–policy interface, e.g., within the context of the Sustainable Development Goals [15], but is rarely considered in biodiversity conservation planning and the sustainable stewardship of our planet.

Air and spaceborne RS approaches to record geomorphology have been used for some time now by research and planning institutions, because RS approaches enable a cost-effective, increasingly freely available, comprehensive, repetitive, standardized, as well as continuous monitoring of geomorphic characteristics from the local, to the regional and even up to the global level.

This paper review summarizes the state-of-the-art in monitoring for example aeolian-, fluvial and coastal landforms and their geomorphic traits with air- and spaceborne RS technologies. In particular, air- and spaceborne RS technologies, as well as different methods for generating DEM and DSM, are compared, and the advantages and disadvantages of different methods are highlighted.

It also presents numerous examples of monitoring the changes and disturbances of geomorphic structures and functions. Furthermore, RS data products and future RS technologies are introduced that are suitable for monitoring geomorphology as crucial part of geodiversity. A particular focus is on RS technologies such as LiDAR, RADAR, multispectral, hyperspectral, and RS technologies that can be implemented to record geomorphic traits. Due to their specific RS characteristics, spaceborne RADAR and airborne LiDAR RS technologies are the most applied technologies for monitoring aeolian-, fluvial and coastal landforms. LiDAR technologies enable the monitoring of detailed 2D–4D geomorphic traits. Despite the fact that the in-orbit implementation of the first spaceborne LiDAR-RS technologies (GEDI-LiDAR) is still in progress, it will play an essential future role in boosting innovation for monitoring the status, changes, and disturbances of geomorphology from a local to regional, and even to the global scale. The accuracy of geodiversity and biodiversity models is partly determined by the quality, accuracy and suitability of their input information. Consequently, models will only be as reliable for reproducing and forecasting real world conditions and scenarios as the quality and accuracy of the spatio-temporal input data provided. The paper therefore summarizes various RS techniques that are applied with varying precision levels to derive DEM and DSM.

One of the most important RS products is the DEM, which has been released with different levels of detail using various RS techniques with different sensors on the local, regional and global scale. The DEM can be used to derive a wide range of other structural and functional geomorphic diversity indicators, which are imperative for the monitoring and modeling of geo- and biodiversity. Furthermore, the availability of different DEM/DSM products and variants regarding scale and accuracy enable the optimization of models and predictions in terms of scale-specific representability and plausibility [27].

To understand the complexity, the multidimensionality and the interactions of geomorphic changes, processes and disturbances, it is imperative to link air- and spaceborne RS technologies—LiDAR, RADAR, multi- and hyperspectral or airborne geophysical survey technologies on different platforms with in-situ and close-range RS monitoring approaches. Currently, temporal and spectral high-frequency wireless sensor networks are being developed for lysimeters (agricultural and forest lysimeters) and eddy covariance towers, where hyperspectral (400–950 nm) as well as thermal sensor technology are integrated.

These developments are the basis for the establishment of a European or even a global wireless sensor network (spectral, geomagnetic, seismic, and other close range technologies for the high frequency measurements of geohazards) that aim: (1) to calibrate and validate information and spectral responses from air- and spaceborne RS data with close-range sensor technology, (2) to better understand and quantify local and regional processes and interactions of geo-biodiversity, land use intensity and human pressures, (3) to advance data-based modelling that will allow more accurate predictions of events, as well as (4) to reduce data and model uncertainties, thus ensuring better transferability from point to area (logical, regional and global).

With the help of spectral traits (ST) and spectral trait variations (STV), the RS approach for monitoring and understanding geodiversity [3], biodiversity [54], and ecosystem health [139,140]

can record the status, changes, disturbances and processes of geomorphology. In the context of geomorphology, the trait approach is crucial, as traits or geomorphic traits constitute the singularly crucial interface between in-situ and RS approaches (close- and air/spaceborne RS) (see Figure 13).

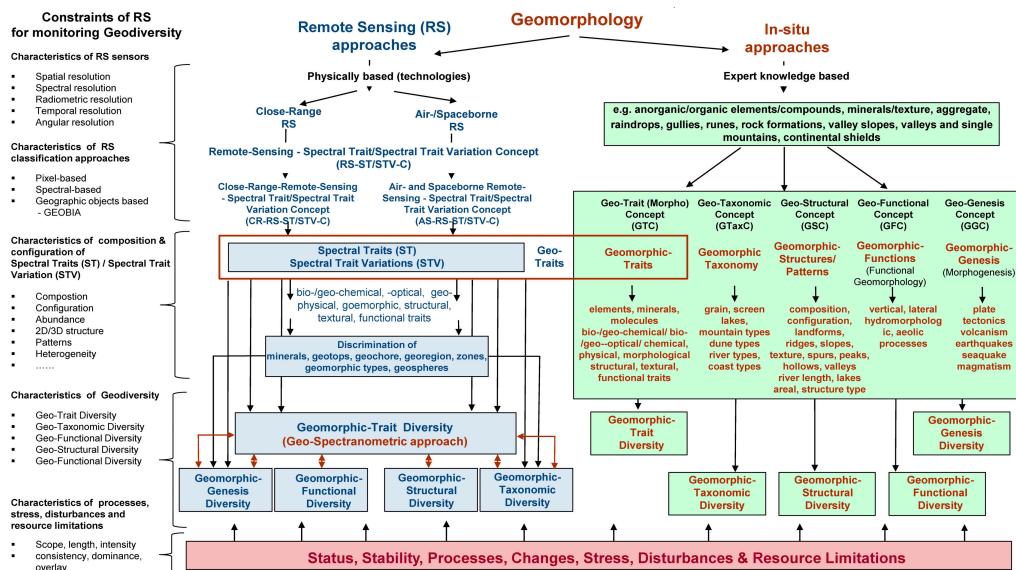


Figure 13. In-situ and remote sensing (RS) approaches and their limitations for monitoring geomorphology, its traits and its five characteristics (modified after Lausch et al., [3]).

We can only understand and classify the RS geomorphology assessment methods if we understand the RS approach, RS spectral indicators, and RS data products. This requires a new orientation and a “new RS based” definition of geomorphology, which allows for a combination of in-situ and RS approaches. The basis of this should be that geomorphology as a crucial part of geodiversity can be defined by five essential characteristics and monitored using RS approaches (see Figure 13, modified after Lausch et al. [3]). These characteristics are: geomorphic trait diversity, geomorphic genesis diversity, geomorphic taxonomic diversity, geomorphic structural diversity, and geomorphic functional diversity. Since RS approaches can record traits and trait variations of geomorphology based on the principles of image spectroscopy, geomorphic trait diversity depicts the essential components that influence the monitoring of the other four geomorphic diversity characteristics. Geomorphic diversity exists on all spatio-temporal scales and can therefore be recorded and monitored with different sensor technologies on different RS platforms.

In subsequent papers, the recording of the five characteristics of geodiversity in terms of different RS characteristics will be presented and discussed in detail. This new approach and new way of thinking guarantees a holistic recording and assessment of different geomorphic traits, which are important for the monitoring of geomorphic (genesis, taxonomic, structural, and functional) diversity patterns. Therefore, a multi-spectral and multi-temporal RS approach enables the compensation of technological limitations of the single RS sensors by synergizing multi-sensor RS approaches. There is not a single RS sensor, RS platform, monitoring approach, or model that is sufficient enough to operate individually to understand the complexity, the processes, the changes, the disturbances, and the interactions of the geo- and biodiversity within the ecosystem in the context of the social–human system.

The increasingly successful implementation of multi-sensor and multi-temporal RS techniques for data assimilation, calibration, and validation have greatly contributed to minimizing uncertainty in ecological modeling, as well as making robust predictions about extreme events and their impacts, reducing the need for as many in-situ observations [234,262–264].

Table 2. Summary of various studies on the accuracy assessment of Digital Surface Models (DSMs, modified after Alganci [92]).

Sensor/Satellite/Mission	Scale/Access	Sensor Type & Auxiliary DEM Products	Nominal Horizontal Resolution [m]	Vertical Accuracy [m]	RMSE [m]	Reference
Spaceborne Photogrammetric						
ALOS AW3D30	Global/open access	optical	30	7 (LE 90)	4.4	[265,266]
Terra ASTER	Global/open access	optical	30	(~13)	5	[87,88]
ASTER GDEM 2	Global/open access	optical	30	17 (95% conf.)	2.3	[87]
ASTER GDEM 3	Global/open access	optical	72 (2.4 arcsec) (for Japan only, [267])	17 (95% conf.)	2.3	[92,102]
SPOT DEM	Continents/commercial	optical	30	10	NA	[266]
IKONOS	commercial	optical	22	~1.5	NA	[266]
Spaceborne—RADAR						
TanDEM-X 90	Global/open access	SAR X	30, 90	NA	3.1	[268,269]
TanDEM-X	Global/open access	SAR X	10	<0.20	<1.4	[103]
TerraSAR-X	Global/open access	SAR X	10	<0.20	<1.4	[103]
Bare Earth DEM	Global/open access	SRTM	90	5.9	5.9	[270]
EarthEnv-DEM90	Global/open access	SRTM3, ASTER GDEM, GLSDEM SRTM3	90	-6.2 (average in ASTER zone) -1.64 (average in SRTM zone) 0.82 (average in blend zone)	10.554 (in ASTER zone) 4.13 (in SRTM zone) 5.362 (in blend zone)	[271]
GMTED2010	Global/open access	SRTM & 10 other sources	250, 500, 1000	6 (RMSE)	26	[272]
MERIT	Global/open access	SRTM3, AW3D30, VFP-DEM, ICESat GLAS	90	<2 (for 58% of globe)	5.0 (LE90)	[273]
SRTM	Global/open access	SAR C-band	30, 90	6–9 (LE90)	6.0 (MAE)	[274]
Viewfinder Panorama	Global/open access	ASTER, SRTM & other sources	90	NA	Not reported	[275]
SRTM Plus or SRTM NASA V3	Global/open access	SAR C-band	90	6–9 (LE90)	5.9	[266]
ALOS AW3D (ALOS PALSAR)	Global/commercial	optical	5	4.10	2.7	[276,277]
PlanetDEM 30 Plus	Global/commercial	SRTM	<10 (LE90)	Not reported	Not reported	[278]
NEXMap World 10	Global/commercial	Not reported	10	5 (RMSE)	10 (LE9)	[279]
WorldDEM	Global/commercial	TanDEM-X	12	<2 (relative), <6 (absolute)	<1.4	[268,277]
Tandem-L (planned)	Global	SAR L-band	~12 (bare), 25 (forest)	2 (bare), 4 (vegetated)	NA	[46]

Table 3. Specification of output Digital Elevation Models (DEMs, modified after Hawker [134]).

Data Source	Generation Method	Date of the Study	Region of the Study	Reference
SPOT-5 HRS	Parallel projection modeling	2004	Korea, Belgium	[280]
SRTM, ASTER	Statistical measures	2006	Crete, Greece	[281]
IKONOS, QuickBird and OrbView-3	Automatic image matching	2006	Maras and Zonguldak, Turkey; Phoenix, United States	[282]
SPOT-5 in-track HRS and across-track HRG	Area-based multiscale image matching method	2006	North of Québec City, Canada	[283]
IKONOS, QuickBird	Physical and empirical models	2006	North of Québec City, Canada	[284]
IKONOS	Multi-image matching	2006	Thun, Switzerland	[285]
IKONOS, QuickBird, OrbView-3, Cartosat-1	Automatic image matching	2007	Maras and Zonguldak, Turkey; Phoenix, United States	[286]
IKONOS	Automatic image matching	2008	Maras and Istanbul, Turkey	[287]
Cartosat-1	Towards automated DEM generation	2008	Catalonia, Spain	[239]
Geoeye-1 and Cosmo-SkyMed	Rigorous model and RPC model	2010	Rome and Merano, Italy	[288]
GeoEye-1 and TerraSAR-X	RPC models for optical, radargrammetry for synthetic aperture RADAR (SAR)	2012	Trento, Italy	[289]
WorldView-2 Google	Bias-compensated RPC bundle block-adjusted images generation, dense image matching, and DSM generation	2016	Munich, Germany	[290]
Google Earth (GE)	Terrain extraction from GE	2016	Guangyuan City, China	[291]
ALOS PALSAR	DEM extraction with InSAR technique	2015	Guangyuan City, China	[292]
ASTER GDEM v.2, SRTM-C, TerraSAR-X, ALOS W3D	Vertical accuracy by dGPS and morphometric comp	2017	Central Andean Plateau, Argentina	[293]
AW3D30, ASTER, SRTM30, SRTM90, TanDEM-X	Optical stereo mapping (AW3D30, ASTER) & Single-pass SAR interferometry (SRTM30, SRTM90, TanDEM-X)	2020	14 sites in Europe, USA and Antarctica	[294]

Table 4. RS-assisted derivation of terrain and landscape surfaces.

Mission/Platform Sensor UAV ¹ Airborne ² Spaceborne ³	Sensor Characteristics	Spectral Resolution Spectral Bands/Frequency	References
Terrain, Digital Elevation Model (DEM)			
SRTM ³	single pass InSAR	X-band, C-band	[69]
TerraSAR-X ³	single pass InSAR	X-band	[57]
TanDEM-X ³	single pass InSAR	X-band	[103,295]
Sentinel-1 A/B ³	repeat pass InSAR	C-band	[296]
ALOS PALSAR ³	repeat pass InSAR	L-band	[297]
ALOS-2 PALSAR-2 ³	repeat pass InSAR	L-band	[298]
Terra ASTER ³	dual stereographic imaging system (line scanner)	NIR (nadir and 28° backward looking)	[299]
ALOS PRISM ³	triplet stereographic imaging system (line scanner)	Panchromatic: $\lambda = 520\text{--}770$ nm (forward, nadir, and backwards looking)	[297,300]
ICESat GLAS ³	LiDAR (full waveform)	3 lasers ($\lambda = 1064$ nm)	[301]
Sentinel-3 SRAL ³	RADAR altimeter	Ku-band, C-band	[302]
F-SAR ²	single pass InSAR repeat pass InSAR	X-band, S-band C-band, L-band, P-band	[303]
UAVSAR ²	repeat pass InSAR	L-band	[304]
Orbisar-RFP ²	single pass InSAR	X-band, P-band	[305]
Pi-SAR-L ²	repeat pass InSAR	L-band	[306]
Leica DMC III ²	stereographic imaging system (discrete overlapping images)	R, G, B, NIR	[307]
Leica ADS40 ²	triplet stereographic imaging system (line scanner)	R, G, B, NIR (nadir), panchromatic (forward, nadir, and backwards looking)	[308]
Quantum systems TRON ¹ Quadrocopter-fixed wing hybrid (platform, gimbal, various camera systems)	stereographic imaging system (discrete overlapping images)	R, G, B (multiple sensors)	[309]
Geocopter X8000 ¹ Octocopter (platform, gimbal, various camera systems)	stereographic imaging system (discrete overlapping images)	R, G, B (Sony NEX7) or similar sensors	[86]
DJI Phantom IV Pro ¹ Quadrocopter (platform, gimbal, installed camera system)	stereographic imaging system (discrete overlapping images)	R, G, B (1'' CMOS)	[310]
RiCOPTER VUX-SYS ¹ (platform with integrated VUX1UAV LiDAR scanner)	LiDAR (multiple return, echo intensity recording)	One laser (NIR), max. 500,000 shots/s	[311]
Quantum systems TRON ¹ Quadrocopter-fixed wing hybrid (platform with integrated YellowScan "SURVEYOR" LiDAR scanner)	LiDAR (two return)	One laser ($\lambda = 905$ nm), max. 300,000 shots/s	[309]

Table 4. Cont.

Mission/Platform Sensor UAV ¹ Airborne ² Spaceborne ³	Sensor Characteristics	Spectral Resolution Spectral Bands/Frequency	References
Surfaces/vegetation surfaces (digital surface model–DSM)			
TanDEM-X ³	single pass InSAR	X-band	[295]
ALOS PALSAR ³	repeat pass InSAR	L-band	[297]
ALOS-2 PALSAR-2 ³	repeat pass InSAR	L-band	[298]
ICeStaT GLAS ³	LiDAR (full waveform)	3 lasers ($\lambda = 1064$ nm)	[301]
F-SAR ²	single pass InSAR repeat pass InSAR	X-band, S-band C-band, L-band, P-band	[303]
UAVSAR ²	repeat pass InSAR	L-band	[304]
Orbisar-RFP ²	single pass InSAR	X-band, P-band	[305]
Pi-SAR-L ²	repeat pass InSAR	L-band	[306]
Geocopter X8000 ¹ Octocopter (platform, gimbal, various camera systems)	stereographic imaging system (discrete overlapping images)	R, G, B (Sony NEX7) or similar sensors	[86,312]
DJI Phantom IV Pro ¹ Quadcopter (platform, gimbal, installed camera system)	stereographic imaging system (discrete overlapping images)	R, G, B (1" CMOS)	[310]
RiCOPTER VUX-SYS ¹ (platform with integrated VUX1UAV LiDAR scanner)	LiDAR (multiple return, echo intensity recording)	One laser (NIR), max. 500,000 shots/s	[311]
Quantum systems TRON ¹ Quadcopter-fixed wing hybrid (platform with integrated YellowScan "SURVEYOR" LiDAR scanner)	LiDAR (two return)	One laser ($\lambda = 905$ nm), max. 300,000 shots/s	[309]
Geomorphic changes and disturbances—terrain changes, vertical displacements, elevation differences, surface deformations			
COSMO Skymed ³	DiffInSAR (in areas with no vegetation) PSI (essentially in urban areas, suited time series available for some regions)	X-band	[313]
TanDEM-X, TerraSAR-X ³	DiffInSAR (in areas with no vegetation) PSI (essentially in urban areas, suited time series available for some regions)	X-band	[314,315]
ERS-1, ERS-2 ³	DiffInSAR (in areas with no or sparse vegetation) PSI (essentially in urban areas, suited time series from 1991 to 2003 available for several regions)	C-band	[316–319]
ENVISAT ASAR ³	DiffInSAR (in areas with no or sparse vegetation) PSI (essentially in urban areas, suited time series from 2002 to 2012 available for several regions)	C-band	[316,320]
Sentinel-1 A/B ³	DiffInSAR (in areas with no or sparse vegetation) PSI (essentially in urban areas, dense time series available almost globally since end of 2014)	C-band	[317,321]
RADARSAT-2 ³	DiffInSAR (in areas with no or sparse vegetation) PSI (essentially in urban areas, dense time series rarely available)	C-band	[322,323]

Table 4. Cont.

Mission/Platform Sensor UAV ¹ Airborne ² Spaceborne ³	Sensor Characteristics	Spectral Resolution Spectral Bands/Frequency	References
Geomorphic changes and disturbances—terrain changes, vertical displacements, elevation differences, surface deformations			
ALOS PALSAR ³	DiffInSAR (in non-forested areas) PSI (essentially in urban areas, long and dense time series rarely available)	L-band	[315,320]
ALOS-2 PALSAR-2 ³	DiffInSAR (in non-forested areas) PSI (essentially in urban areas, long and dense time series rarely available)	L-band	[324]
SAOCOM ³	DiffInSAR (in non-forested areas) PSI (essentially in urban areas, long and dense time series rarely available)	L-band	[325]
Airborne LiDAR ² , e.g., Optech ALTM Gemini	LiDAR (four return, echo intensity recording), for changes in the order of dm or more	One laser, max. 167,000 shots/s	[71,319,326,327]
UAV photogrammetry ¹ , e.g., Octocopter X8000 (platform, gimbal, various camera systems)	stereographic imaging system (discrete overlapping images) for changes in the order of several dm or more, uniformly distributed reference targets required	R, G, B (Sony NEX7) or similar sensors	[328,329]
RiCOPTER VUX-SYS ¹ (platform with integrated VUX1UAV LiDAR scanner)	LiDAR (multiple return, echo intensity recording), for changes in the order of dm or more	One laser (NIR), max. 500,000 shots/s	[311]

Sensor is used on the RS platform: UAV¹—unmanned aerial vehicles (UAV); airborne²—airborne RS platform; spaceborne³—spaceborne RS platform.

Table 5. Remote sensing (RS)-aided derived in monitoring examples in terrain and surfaces, aeolian geomorphology, fluvial geomorphology and coastal geomorphology landslides and their traits.

	Mission/Platform Sensor	References
Terrain and Surfaces/Traits		
Geomorpho90m (90 m/100 m/250 m) (Slope, Aspect, Aspect cosine, Aspect sine, Eastness, Northness, Convergence, Compound topographic index, Stream power index, East-West first order partial derivative, North-South first order partial derivative, Profile curvature, Tangential curvature, East-West second order partial derivative, North-South second order partial derivative, Second order partial derivative, Elevation standard deviation, Terrain ruggedness index, Roughness, Vector ruggedness measure, Topographic position index, Maximum multiscale deviation, Scale of the maximum multiscale deviation, Maximum multiscale roughness, Scale of the maximum multiscale roughness, Geomorphon	(26 geomorphometric variables derived from MERIT-DEM ^{3/R} —corrected from the underlying Shuttle RADAR Topography Mission (SRTM3) and ALOS World 3D—30 m (AW3D30) DEMs)	[24]
Mountain types, relief types, relief classes	IKONOS OSA ^{3/M} , DHM25 ^{3/R} , GTOPO30-DEM ^{3/R} , LiDAR ^{2/L}	[330–332]
Volcano types (volcanic full forms),volcanoes, lava flow fields, hydrothermal alteration, geothermal explorations, heat fluxes, volcanoes hazard monitoring	Doves-PlanetScop, Terra/Aqua MODIS ^{3/M} , EO-1 ALI ^{3/M} , Landsat-8 OLI ^{3/M/TIR} , Terra ASTER ^{3/M/TIR} , MSG SEVIRI ^{3/M/TIR} , LiDAR ^{2/L}	[333–337]
Mountain hazards, mass movement (rock fall probability, boulders, denudation, mass erosion, rock decelerations, rotation changes, slope stability, rock shapes, particle shapes, patterns, structures, faults and fractures, holes and depressions)	InSAR ^{3/R} , SAR ^{3/R} , LiDAR ^{2/L} , Digital Orthophoto ^{1/RGB}	[338–347]
Landslide chances, landslide evolution	Digital Orthophoto ^{1/RGB}	[348]
Above ground—chances, disturbances Opencast mining, sand mining and extraction, tipping, dumps	TanDEM-X ^{3/R} , SRTM DEM ^{3/R} , ALOS PALSAR ^{3/R} , ERS-1 ^{3/R} , GeoEye GIS ^{3/M} , WorldView-3 Imager ^{3/M} , IKONOS OSA ^{3/M} , Landsat-5 TM/-7 ETM+/-8 OLI ^{3/M/TIR} , IRS-P6 LISS-III ^{3/M} , High resolution satellite data of Google ^{3/M} , LiDAR ^{2/L}	[349–355]
Vegetation traits as proxy of the geochemical parameters	HyMAP ^{2/H}	[356]
Below ground—chances, disturbances Salt mines, fracking	ERS-1/-2 ^{3/R} , ASAR ^{3/R} , ALOS PALSAR ^{3/R} , Landsat-5 TM/-7 ETM+/-8 OLI ^{3/M/TIR}	[113,357]

Table 5. Cont.

	Mission/Platform Sensor	References
Aeolian geomorphology/traits		
Desertification, soil and land-degradation, soil erosion	NOAA/MetOp AVHRR ^{3/R} , ERS-1/-2 ^{3/R} , SIR-C ^{3/R} , ENVISAT ^{3/R} , ASAR ^{3/R} , RADARSAT-1 ^{3/R} , ALOS PALSAR ^{3/R} , Terra/Aqua MODIS ^{3/M} , IRS1B LISS-I/LISS-II ^{3/M} , Sentinel-2 MSI ^{3/M} , Landsat-5 TM/-7 ETM+/-8 OLI ^{3/M} , LiDAR ^{2/L}	[143,144,358–363]
Dune migration, migration rates, dune expansion, dune activity, moving dunes	ALOS PALSAR ^{3/R} , Landsat-8 OLI ^{3/M} , Sentinel-2 MSI ^{3/M} , Context Camera ^{2/RGB} , LiDAR ^{2/L}	[160,161,364–366]
Dune types, dune hierarchies, dune morphometry, dune hierarchies (free dunes—shifting sand dunes, bounded dunes, dune fields, dune shapes (crescent, cross, linear, stars, dome, parabolic, longitudinal dune)	SRTM ^{3/R} , SIR-C/X-SAR ^{3/R} , WorldView-2 WV110 ^{3/M} , IRS-RS2 LISS-IV ^{3/M} , Cartosat-1 PAN-F/-A ^{3/M} , Landsat-7 ETM+ ^{3/M} , Landsat MSS ^{3/M} , LiDAR ^{2/L}	[152,367–371],
Dune spatial-temporal aeolic patterns (length, minimum spacing density, orientation, height, sinuosity), aeolian dune composition-configuration (complexity, diversity, shapes, patterns, heterogeneity), dune ridges (lines)	SRTM ^{3/R} , SIR-C ^{3/R} , Landsat-7 ETM+ ^{3/M} , LiDAR ^{2/L} , Digital Orthophoto ^{3/RGB}	[150–155,366]
Volume and their changes, intensity of dune	SRTM ^{3/R} , SPOT-5 HRG ^{3/M} , Terra ASTER ^{3/M} , LiDAR ^{2/L}	[150,152,163,372]
Fluvial geomorphology/traits		
Flooding events, flood mapping, flash-flood susceptibility assessment, flood inundation modelling, floodplain-risk mapping, erosive impacts, sedimentation	SRTM ^{3/R} , ALOS PALSAR ^{3/R} , ALSAR-1 ^{3/R} , SAR ^{3/R} , ALOS-2 ^{3/R} , TerraSAR-X ^{3/R} , RADARSAT-2 ^{3/R} , Sentinel-1 ^{3/R} , Landsat-5 TM/-7 ETM+/-8 OLI ^{3/M/TIR} , Sentinel-2 MSI ^{3/M} , IRS-1C/-1D LISS-III ^{3/M} , IKONOS OSA ^{3/M} , DEADALUS ^{2/H} , LiDAR ^{2/L}	[42,177,191,192,195–200, 202–204,207]
Flood mapping under vegetation, irrigation retrieval, groundwater flooding in a lowland karst catchment	SAR ^{3/R} , Landsat-5 TM/-7 ETM+/-8 OLI ^{3/M}	[169,209,216]
Vegetation traits as proxy of the geochemical parameters, heavy metal stress in plants	HyMAP ^{2/H} , HySPEX ^{2/H}	[179,356]
River detection, small streams detection	SAR ^{3/R} , Landsat-5 TM/-7 ETM+/-8 OLI ^{3/M} , Aerial images ^{2/RGB} , Aerial images ^{1/RGB} , LiDAR ^{2/L}	[180,262,373–375]
Channel landforms, hydrogeomorphic units including coarse woody debris, hydraulic (fluvial) landform classification, taxonomy of fluvial landforms, hydro-morphological units, riverscape units, river geomorphic units, in-stream mesohabitats, tidal channel characteristics	SAR ^{3/R} , Aerial images ^{2/RGB} , LiDAR ^{2/L}	[373,376–378]
Channel characteristics, floodplain morphology hydraulic channel morphology, geometries, topography, river width arc length, longitudinal transect, (width, depth, and longitudinal channel slope, below water line morphology), Morphometric patterns of meanders (sinuosity, intrinsic wavelength, curvature, asymmetry), meander dynamics, channel geometry	SAR ^{3/R} , ENVISAT ^{3/R} , Terra/Aqua MODIS ^{3/M} , Landsat-5 TM/-7 ETM+/-8 OLI ^{3/M} , Sentinel-2 MSI ^{3/M} , Aerial images ^{2/RGB} , LiDAR ^{2/L}	[222,230,233,235,236, 262,379–381]

Table 5. Cont.

	Mission/Platform Sensor	References
Fluvial geomorphology/traits		
Channel migration, channel migration rates, channel planform changes, tidal channel migration Channel changes, disturbances, temporal evolution of natural and artificial abandoned channels, canal position, systematic changes of the river banks and canal centre lines	SAR ^{3/R} , SRTM ^{3/R} , Landsat-5 TM ^{3/M} , Landsat-7 ETM+/-8 OLI ^{3/TIR} , Aerial images ^{2/RGB}	[223–228,378]
Flow energy of stream power, channel sensitivity to erosion and deposition processes Channel stability assessment	Landsat-1 MSS/-5 TM/-8 OLI ^{3/M} , LiDAR ^{2/L}	[229,382]
River discharge estimation (river discharge, run-off characteristics)	ENVISAT ^{3/R} , Jason-2/-3 ^{3/R} , Sentinel-3A OLCI/SLSTR ^{3/R} , CryoSat-2 ^{3/R} , AltiKa ^{3/R} , ENVISAT ^{3/R} , Advanced RADAR Altimeter (RA-2) ^{3/R} , Terra/Aqua MODIS ^{3/M}	[234,237]
Water and flow velocity	ENVISAT ^{3/R} , Terra/Aqua MODIS ^{3/M} , Aerial images ^{2/RGB} , LiDAR ^{2/L}	[235,373,383]
Water height, water level, water depth	ENVISAT ^{3/R} , AMSR-E ^{3/R} , TRMM ^{3/R} , Daedalus ^{2/H} , Aerial images ^{2/RGB} , LiDAR ^{2/L}	[237,263,373,384–386]
Fluvial sediment transport, sediment budget, channel bank erosion, exposed channel substrates and sediments, suspended soil concentration and bed material, percentage clay, silt and sand in inter-tidal sediments, suspended sediments, flood bank overbank sedimentation, sediment wave, sand mining	LiDAR ^{2/L} , Radio frequency identification ^{1/RFID}	[166,354,380,387]
Stream bank retreat	Aerial images ^{2/RGB} , LiDAR ^{2/L}	[239–244]
Grain characteristics, grain size, gravel size, shape, bed and bank sediment size	Daedalus ^{2/H} , Aerial images ^{2/RGB} , Aerial images ^{2/RGB} , LiDAR ^{2/L}	[168,388–392]
Pebble mobility	Radio frequency identification technologies ^{1/RFID}	[393]
River bathymetry	CASI ^{2/H} , Daedalus ^{2/H} , Aerial images ^{2/RGB} , LiDAR ^{2/L}	[373,386,394–396]
Coastal geomorphology/traits		
Coast taxonomy, coast types (Small Delta, Tidal system, Lagoon, Fjord and Fjärd, Large River, Tidal Estuary, Ria, Karst, Arheic)	Different RADAR Sensors ^{3/R} , Different optical RS Sensors ^{3/R}	[245]
Coastal dynamical and bio-geo-chemical patterns	NOAA/MetOp AVHRR ^{3/R} , ERS-1 ^{3/R} , TOPEX ^{3/R} , Nimbus-7 CZCS ^{3/M/TIR}	[397]
Coastal landforms, coastline and shoreline detection	SRTM ^{3/R} , ALOS ^{3/R} , NOAA ^{3/R} , Landsat-7 ETM+ ^{3/M} , Terra ASTER ^{3/M} , IKONOS OSA ^{3/M} , LiDAR ^{2/L}	[42,398,399]
Spatio-temporal shoreline dynamic, shoreline erosion-accretion trends, coast changes, cliff retreat, erosion hotspots	SRTM ^{3/R} , SAR ^{3/R} , Landsat-4 MSS/-5 TM ^{3/M} , Landsat-8 OLI ^{3/M/TIR} , SPOT 5 ^{3/M} , Sentinel-2 MSI ^{3/M} , Aerial images ^{2/RGB} , LiDAR ^{2/L}	[247,251–253,257,258, 400,401]
Different morphometric shoreline indicators (morphological reference lines, vegetation limits, instant tidal levels and wetting limits, tidal datum indicators, virtual reference lines, beach contours, storm lines)	Different optical RS Sensors ^{3/M} , LiDAR ^{2/L}	[161,246,402]

Sensor is used on the RS platform: UAV ¹—unmanned aerial vehicles (UAV); airborne ²—airborne RS platform; spaceborne ³—spaceborne RS platform. RADAR ^R, Multispectral (MSP) ^M, Hyperspectral (HSP) ^H, RGB ^{RGB}, TIR ^T, LiDAR ^L, Radio frequency identification ^{RFID}

Table 6. Important current and future RS missions and sensors to derive the status and changes of terrain and surfaces.

Mission/Platform Sensor UAV ¹ Airborne ² Spaceborne ³	Sensor Type	Frequency/Spectral Information	Launch Time	References
BIOMASS ³	repeat pass InSAR, repeat pass fully polarimetric InSAR (PolInSAR), SAR Tomography (TomoSAR)	P-band	2021	[403]
SAOCOM 1A ³ SAOCOM 1B ³ SAOCOM-CS ³	repeat pass InSAR (SAOCOM 1A & 1B), single pass PolInSAR (SAOCOM 1B & CS) Terrain observation with Progressive Scans SAR (TopSAR)	L-band	2018/2019	[404]
NiSAR ³	repeat pass InSAR	L-band S-band	>2022	[405]
ALOS-4 PALSAR-3 ³	repeat pass InSAR	L-band	2020	[406]
Tandem-L ³	single pass InSAR, single pass PolInSAR, multi-pass coherence tomography	L-band	2024	[407,408]
ROSE-L	repeat pass InSAR	L-band	2028	[409]
NovaSAR-S ³	single pass InSAR	S-band	2018	[410,411]
GEDI LiDAR ³	LiDAR (full waveform)	3 laser transmitter, 1064 nm	2019	[45,122,123,412]
ICESat-2 ³	LiDAR (full waveform)	1 laser 6 beams, 532 nm (ATLAS)	2018	[124,130,131]

Sensor is used on the RS platform: UAV ¹—unmanned aerial vehicles (UAV); airborne ²—airborne RS platform; spaceborne ³—spaceborne RS platform.

Table 7. Selection of remote sensing (RS)-aided data products for monitoring terrain, surfaces and fluvial landform data products.

Data Products	Scale	Link	References
Various DEMs	Global	Planetobserver: https://www.planetobserver.com/products/planetdem/planetdem-30/	[278]
NEXMap® Elevation Data Suite	Global	https://www.intermap.com/nextmap	[279]
TEMIS-GTOPO30 global digital elevation model (GDEM)—30 m	Global	http://www.temis.nl/data/gtopo30.html	[413,414]
GTOPO30 Earth Resources Observation and Science Center/U.S. Geological Survey/U.S. Department of the Interior, USGS 30 ARC-second Global Elevation Data, GTOPO30 (Research Data Archive at the National Center for Atmospheric Research, Computational and Information Systems Laboratory, 1997)	Global	http://rda.ucar.edu/datasets/ds758.0/ .	[415]
ASTER GDEM V3 ASTER Global Digital Elevation Model (GDEM) Version 3 (ASTGTM)1 arc second	Global	https://lpdaac.usgs.gov/products/astgtmv003/DOI:10.5067/ASTER/ASTGTM.003	[88]
ALOS Global Digital Surface Model “ALOS World 3D (AW3D30)” 30 m PRISM DEM	Global	http://www.eorc.jaxa.jp/ALOS/en/aw3d30/	[90,297]
SRTM 30 m, 90 m, 1 km Elevation Data	Global	http://www.landcover.org/data/srtm/ https://developers.google.com/earth-engine/datasets/catalog/USGS_SRTMGL1_003	[416]
SRTM/SRTM NASA V2	Global	https://dds.cr.usgs.gov/srtm/ https://www2.jpl.nasa.gov/srtm/	[293,417]
SRTM Plus/SRTM NASA V3	Global	https://lpdaac.usgs.gov/products/measures_products_table	[101,102]
ALOS DSM: 30 m	Global	https://developers.google.com/earth-engine/datasets/catalog/JAXA_ALOS_AW3D30_V1_1 http://www.eorc.jaxa.jp/ALOS/	[418]
NASADEM	Global	en/aw3d30/	[102]
TanDEM-X DEM WorldDEM	Global	https://tandemx-science.dlr.de/cgi-bin/wcm.pl?page=DEM_Promotion_Start_Page (free samples for scientific purposes) http://www.intelligence-airbusds.com/worlddem/ (commercial)	[103]
ICESat/GLAS	Global	https://nsidc.org/data/icesat/data.html	[301,329]
GEDI LiDAR	Global	https://gedi.umd.edu/data/products/	[122]
Global Land Survey Digital Elevation Model (GLSDEM)	Global	http://www.landcover.org/data/glsdem/	[419]

Table 7. Cont.

Data Products	Scale	Link	References
Global ALOS Landforms	Global	https://developers.google.com/earth-engine/datasets/catalog/CSP_ERGo_1_0_Global_ALOS_landforms	[420]
Global ALOS Topographic Diversity	Global	https://developers.google.com/earth-engine/datasets/catalog/CSP_ERGo_1_0_Global_ALOS_topoDiversity	[420]
Global ALOS CHILI (Continuous Heat-Insolation Load Index)	Global	https://developers.google.com/earth-engine/datasets/catalog/CSP_ERGo_1_0_Global_ALOS_CHILI	[420]
Global ALOS mTPI (Multi-Scale Topographic Position Index)	Global	https://developers.google.com/earth-engine/datasets/catalog/CSP_ERGo_1_0_Global_ALOS_mTPI	[420]
GMTED2010: Global Multi-resolution Terrain Elevation Data 2010	Global	https://developers.google.com/earth-engine/datasets/catalog/USGS_GMTED2010	[272]
Free Global DEM Data Sources—Digital Elevation Models	Global	https://gisgeography.com/free-global-dem-data-sources/	NA
The global Human Modification dataset (gHM)	Global	https://developers.google.com/earth-engine/datasets/catalog/CSP_HM_GlobalHumanModification	[421]
Copernicus DEM—Global and European Digital Elevation Model (COP-DEM)	Global/EEA39*	https://spacedata.copernicus.eu/web/cscda/dataset-details?articleId=394198	[422]
Geomorpho90m (90 m/100 m/250 m) (26 geomorphometric variables derived from MERIT-DEM—corrected from the underlying Shuttle RADAR Topography Mission (SRTM3) and ALOS World 3D—30 m (AW3D30) DEMs) Slope, Aspect, Aspect cosine, Aspect sine, Eastness, Northness, Convergence, Compound topographic index, Stream power index, East-West first order partial derivative, North-South first order partial derivative, Profile curvature, Tangential curvature, East-West second order partial derivative, North-South second order partial derivative, Second order partial derivative, Elevation standard deviation, Terrain ruggedness index, Roughness, Vector ruggedness measure, Topographic position index, Maximum multiscale deviation, Scale of the maximum multiscale deviation, Maximum multiscale roughness, Scale of the maximum multiscale roughness, Geomorphon	Global	http://www.spatial-ecology.net/dokuwiki/doku.php?id=topovar90m https://doi.pangaea.de/10.1594/PANGAEA.899135 https://portal.opentopography.org/dataspace/dataset?opentopoID=OTDS.012020.4326.1	[24]
Physiography	US	https://developers.google.com/earth-engine/datasets/catalog/CSP_ERGo_1_0_US_physiography	[420]
Physiographic Diversity	US	https://developers.google.com/earth-engine/datasets/catalog/CSP_ERGo_1_0_US_physioDiversity	[420]
OpenTopography High-Resolution Topography Data and Tools	Global/Regional/Local	https://opentopography.org/	NA

Table 7. Cont.

Data Products	Scale	Link	References
Airborne LiDAR data Open Topography High-Resolution Topography Data and Tools	Regional	http://gisgeography.com/top-6-free-lidar-data-sources/ http://www.geoportal-th.de/de-de/Downloadbereiche/Download-Offene-Geodaten-Th%C3%BCrtingen http://opentopography.org (US-based, but world-wide coverage)	[319,327]
RS Global Airborne Laser Scanning Data Providers Database (GlobALS)	Global/Regional	https://www.facebook.com/GlobALSData/) to	[423]
Australia's terrestrial ecosystem data	Australia	TERN data Portal https://portal.tern.org.au/#/1a471b0a	NA
Supra National Ground Motion Service	Global/Regional/Local	Yearly Sentinel-1 based products for public (first release 2019) TerraSAR-X/TanDEM-X based product on request for commercial use	[424]
Terrafirma Atlas	Global/Regional/Local	http://www.terrafirma.eu.com/ Open service partnership, production on request	[424,425]
Incomplete Inventory Surface Deformation in North America	Regional	catalogue with sites of suspected anthropogenic deformation, deformation data	[426]
ArcticDEM Mosaic	Regional	https://developers.google.com/earth-engine/datasets/catalog/UMN_PGC_ArcticDEM_V3_2m_mosaic	[427–429]
EU-DEM, Slope, Aspect, Hillshade	EEA39 **	https://land.copernicus.eu/product-portfolio/overview	NA
GeoNetworksMultisource, multisensor geospatial data and measurements of mountain areas	Global	(https://geonetwork-opensource.org/)	[430]
Global River Widths from Landsat (GRWL) Database	Global	https://doi.org/10.1126/science.aat063	[374]
GFPLAIN250m, a global high-resolution dataset of earth's floodplains	Global	https://github.com/fnardi/GFPLAIN with	[431]
MERIT Hydro: A High-Resolution Global Hydrography Map Based on Latest Topography Dataset.	Global	http://hydro.iis.u-tokyo.ac.jp/~yamada/MERIT_Hydro/	[432]
Dataset of 100-year flood susceptibility maps	US	https://data.4tu.nl/articles/100-year_flood_susceptibility_maps_for_the_continental_U_S_derived_with_a_geomorphic_method/12693680	[433]
Global Flood Hazard	Global	https://data.jrc.ec.europa.eu/collection/floods	[434]
Modis Flood Mapping	Global	https://floodmap.modaps.eosdis.nasa.gov/	[435]
Map of Active Volcanoes and recent Earthquakes world-wide	Global	https://earthquakes.volcanodiscovery.com/	NA
Volcano hazard monitoring	US	https://www.usgs.gov/natural-hazards/volcano-hazards/	[333]

** 39 countries in the European Economic Area (EEA39).

Author Contributions: A.L. was responsible for the main part of this review analysis, writing, and production of some figures and some tables. T.J., C.T and C.M. contributed their knowledge about extensive methodology of terrain and surfaces as crucial characteristics for all geomorphological landforms. J.M.H., L.B., and S.J. run an aircraft or an aircraft company and have contributed numerous results and figures of flight campaigns for this paper. T.J., C.M., and S.C.T. have made important contributions to DEM/DSM and to the creation and correction of all tables. All co-authors, M.E.S., A.K.S., S.C.T., J.M.H., J.B. (Jussi Baade), L.B., E.B., J.B. (Jan Bumberger), P.D., C.G., D.H., M.H., T.J., S.J., R.K., M.M., H.M., C.M., M.P., C.R., N.S., C.S. (Christiane Schmillius), F.S., C.S. (Claudia Schütze), C.S. (Christian Schweitzer), P.S., D.S., M.V. (Michael Vohland), M.V. (Martin Volk), U.W. (Ute Weber), T.W., U.W. (Ulrike Werban), S.Z., and C.T., revised all requirements, checked and contributed to the final text, tables, and figures. All authors have read and agreed to the published version of the manuscript.

Funding: This research received no external funding.

Acknowledgments: Our special thanks go to the Helmholtz Centre for Environmental Research- UFZ and the TERENO project funded by the Helmholtz Association and the Federal Ministry of Education and Research for providing the hyperspectral equipment. This work was supported by funding from the Helmholtz Association in the framework of MOSES (Modular Observation Solutions for Earth Systems). At the same time we truly appreciate the support that we received from the project ‘GEOEssential—Essential Variables workflows for resource efficiency and environmental management’. The authors also thank the reviewers for their very valuable comments and recommendations. The authors gratefully acknowledge the German Helmholtz Association for supporting the activities. This study was conducted under the funding of the HGF Alliance HA-310 ‘Remote Sensing and Earth System Dynamics’. UM is grateful to the Helmholtz funded virtual institute DESERVE. Airborne Research Australia is substantially supported by the Hackett Foundation, Adelaide. One of the ARA ECO-Dimonas was donated by the late Don and Joyce Schultz of Glen Osmond, South Australia. I would like to express my special thanks to them for the very high quality image data from aircraft campaigns. In order to capture such high quality image data by means of aircraft campaigns, it is often necessary to have longstanding requirements: I would especially like to thank Sven Jany, Milan Geoservice GmbH—Figure 2c,f; Figure 3c–e; Figure 4a,b,d; Figures 9–11; Jorg Hacker, Airborne Research Australia (ARA)—Figure 2d,e,g,h; Figure 6; Christiane Schmillius, Christian Thiel and Nesrin Salepci, Friedrich Schiller University Jena—Figure 3b; Figure 4c,e; Figure 5; as well as Cornelia Glässer; Martin Luther University Halle-Wittenberg—Figure 8.

Conflicts of Interest: The authors declare no conflict of interest.

References

- Antonelli, A.; Kissling, W.D.; Flantua, S.G.A.; Bermúdez, M.A.; Mulch, A.; Muellner-Riehl, A.N.; Kreft, H.; Linder, H.P.; Badgley, C.; Fjeldså, J.; et al. Geological and climatic influences on mountain biodiversity. *Nat. Geosci.* **2018**, *11*, 718–725. [[CrossRef](#)]
- Leser, H.; Löffler, J. *Landschaftsökologie*; Auflage: 5.; Eugen Ulmer KG: Stuttgart, Germany, 2017; ISBN 3825287181.
- Lausch, A.; Baade, J.; Bannehr, L.; Borg, E.; Bumberger, J.; Chabrilhat, S.; Dietrich, P.; Gerighausen, H.; Glässer, C.; Hacker, J.; et al. Linking Remote Sensing and Geodiversity and Their Traits Relevant to Biodiversity—Part I: Soil Characteristics. *Remote Sens.* **2019**, *11*, 2356. [[CrossRef](#)]
- Green, J.L.; Bohannan, B.J.M.; Whitaker, R.J. Microbial Biogeography: From Taxonomy to Traits. *Science* **2008**, *320*, 1039–1043. [[CrossRef](#)]
- Read, Q.D.; Zarnetske, P.L.; Record, S.; Dahlin, K.M.; Costanza, J.K.; Finley, A.O.; Gaddis, K.D.; Grady, J.M.; Hobi, M.L.; Latimer, A.M.; et al. Beyond counts and averages: Relating geodiversity to dimensions of biodiversity. *Glob. Ecol. Biogeogr.* **2020**, *29*, 696–710. [[CrossRef](#)]
- Muellner-Riehl, A.N.; Schnitzler, J.; Kissling, W.D.; Mosbrugger, V.; Rijdsdijk, K.F.; Seijmonsbergen, A.C.; Versteegh, H.; Favre, A. Origins of global mountain plant biodiversity: Testing the ‘mountain-geobiodiversity hypothesis’. *J. Biogeogr.* **2019**, *46*, 2826–2838. [[CrossRef](#)]
- Lawler, J.J.; Ackerly, D.D.; Albano, C.M.; Anderson, M.G.; Dobrowski, S.Z.; Gill, J.L.; Heller, N.E.; Pressey, R.L.; Sanderson, E.W.; Weiss, S.B. The theory behind, and the challenges of, conserving nature’s stage in a time of rapid change. *Conserv. Biol.* **2015**, *29*, 618–629. [[CrossRef](#)]
- Comer, P.J.; Pressey, R.L.; Hunter, M.L.; Schloss, C.A.; Buttrick, S.C.; Heller, N.E.; Tirpak, J.M.; Faith, D.P.; Cross, M.S.; Shaffer, M.L. Incorporating geodiversity into conservation decisions. *Conserv. Biol.* **2015**, *29*, 692–701. [[CrossRef](#)]
- Haase, P.; Tonkin, J.D.; Stoll, S.; Burkhard, B.; Frenzel, M.; Geijzendorffer, I.R.; Häuser, C.; Klotz, S.; Kühn, I.; McDowell, W.H.; et al. The next generation of site-based long-term ecological monitoring: Linking essential biodiversity variables and ecosystem integrity. *Sci. Total Environ.* **2018**, *613–614*, 1376–1384. [[CrossRef](#)]
- Theobald, D.M. A general model to quantify ecological integrity for landscape assessments and US application. *Landsc. Ecol.* **2013**, *28*, 1859–1874. [[CrossRef](#)]

11. Gordon, J.E.; Crofts, R.; Díaz-Martínez, E.; Woo, K.S. Enhancing the Role of Geoconservation in Protected Area Management and Nature Conservation. *Geoheritage* **2018**, *10*, 191–203. [[CrossRef](#)]
12. Burek, C.V.; Prosser, C.D. The history of geoconservation: An introduction. *Geol. Soc. Spec. Publ.* **2008**, *300*, 1–5. [[CrossRef](#)]
13. Matthews, T.J. Integrating Geoconservation and Biodiversity Conservation: Theoretical Foundations and Conservation Recommendations in a European Union Context. *Geoheritage* **2014**, *6*, 57–70. [[CrossRef](#)]
14. Gray, M.; Gordon, J.E.; Brown, E.J. Geodiversity and the ecosystem approach: The contribution of geoscience in delivering integrated environmental management. *Proc. Geol. Assoc.* **2013**, *124*, 659–673. [[CrossRef](#)]
15. Schrodte, F.; Bailey, J.J.; Kissling, W.D.; Rijdsdijk, K.F.; Seijmonsbergen, A.C.; van Ree, D.; Hjort, J.; Lawley, R.S.; Williams, C.N.; Anderson, M.G.; et al. Opinion: To advance sustainable stewardship, we must document not only biodiversity but geodiversity. *Proc. Natl. Acad. Sci. USA* **2019**, *116*, 16155–16158. [[CrossRef](#)]
16. Alexandrowicz, Z.; Margielewski, W. Impact of mass movements on geo- and biodiversity in the Polish Outer (Flysch) Carpathians. *Geomorphology* **2010**, *123*, 290–304. [[CrossRef](#)]
17. Tukiainen, H.; Kiuttu, M.; Kalliola, R.; Alahuhta, J.; Hjort, J. Landforms contribute to plant biodiversity at alpha, beta and gamma levels. *J. Biogeogr.* **2019**, *46*, 1699–1710. [[CrossRef](#)]
18. Guitet, S.; Péliissier, R.; Brunaux, O.; Jaouen, G.; Sabatier, D. Geomorphological landscape features explain floristic patterns in French Guiana rainforest. *Biodivers. Conserv.* **2015**, *24*, 1215–1237. [[CrossRef](#)]
19. Jin, X.; Wan, L.; Zhang, Y.-K.; Hu, G.; Schaepman, M.E.; Clevers, J.G.P.W.; Su, Z.B. Quantification of spatial distribution of vegetation in the Qilian Mountain area with MODIS NDVI. *Int. J. Remote Sens.* **2009**, *30*, 5751–5766. [[CrossRef](#)]
20. Dobrowski, S.Z. A climatic basis for microrefugia: The influence of terrain on climate. *Glob. Chang. Biol.* **2011**, *17*, 1022–1035. [[CrossRef](#)]
21. Schmidtlein, S.; Feilhauer, H.; Bruehlheide, H. Mapping plant strategy types using remote sensing. *J. Veg. Sci.* **2012**, *23*, 395–405. [[CrossRef](#)]
22. Scaioni, M.; Longoni, L.; Melillo, V.; Papini, M. Remote Sensing for Landslide Investigations: An Overview of Recent Achievements and Perspectives. *Remote Sens.* **2014**, *6*, 9600–9652. [[CrossRef](#)]
23. le Roux, P.C.; Luoto, M. Earth surface processes drive the richness, composition and occurrence of plant species in an arctic-alpine environment. *J. Veg. Sci.* **2014**, *25*, 45–54. [[CrossRef](#)]
24. Amatulli, G.; McInerney, D.; Sethi, T.; Strobl, P.; Domisch, S. Geomorpho90m, empirical evaluation and accuracy assessment of global high-resolution geomorphometric layers. *Sci. Data* **2020**, *7*, 162. [[CrossRef](#)]
25. Pánek, T. Landslides and Quaternary climate changes—The state of the art. *Earth-Science Rev.* **2019**, *196*, 102871. [[CrossRef](#)]
26. Möller, M.; Volk, M.; Friedrich, K.; Lymburner, L. Placing soil- genesis and transport processes into a landscape context: A multiscale terrain-analysis approach. *J. Plant Nutr. Soil Sci.* **2008**, *171*, 419–430. [[CrossRef](#)]
27. Möller, M.; Volk, M. Effective map scales for soil transport processes and related process domains - Statistical and spatial characterization of their scale-specific inaccuracies. *Geoderma* **2015**, *247–248*, 151–160. [[CrossRef](#)]
28. Burnett, M.R.; August, P.V.; Brown, J.H.; Killingbeck, K.T. The Influence of Geomorphological Heterogeneity on Biodiversity I. A Patch-Scale Perspective. *Conserv. Biol.* **2008**, *12*, 363–370. [[CrossRef](#)]
29. Bétard, F. Patch-Scale Relationships Between Geodiversity and Biodiversity in Hard Rock Quarries: Case Study from a Disused Quartzite Quarry in NW France. *Geoheritage* **2013**, *5*, 59–71. [[CrossRef](#)]
30. Pellitero, R.; Manosso, F.C.; Serrano, E. Mid- and large-scale geodiversity calculation in fuentes carrionas (nw Spain) and serra do cadeado (Paraná, Brazil): Methodology and application for land management. *Geogr. Ann. Ser. A Phys. Geogr.* **2015**, *97*, 219–235. [[CrossRef](#)]
31. Parks, K.E.; Mulligan, M. On the relationship between a resource based measure of geodiversity and broad scale biodiversity patterns. *Biodivers. Conserv.* **2010**, *19*, 2751–2766. [[CrossRef](#)]
32. Bailey, J.J.; Boyd, D.S.; Hjort, J.; Lavers, C.P.; Field, R. Modelling native and alien vascular plant species richness: At which scales is geodiversity most relevant? *Glob. Ecol. Biogeogr.* **2017**, *26*, 763–776. [[CrossRef](#)]
33. Bergen, K.M.; Goetz, S.J.; Dubayah, R.O.; Henebry, G.M.; Hunsaker, C.T.; Imhoff, M.L.; Nelson, R.F.; Parker, G.G.; Radeloff, V.C. Remote sensing of vegetation 3-D structure for biodiversity and habitat: Review and implications for lidar and radar spaceborne missions. *J. Geophys. Res. Biogeosciences* **2009**, *114*, 13. [[CrossRef](#)]

34. Rahbek, C.; Borregaard, M.K.; Colwell, R.K.; Dalsgaard, B.; Holt, B.G.; Morueta-Holme, N.; Nogues-Bravo, D.; Whittaker, R.J.; Fjeldså, J. Humboldt's enigma: What causes global patterns of mountain biodiversity? *Science* **2019**, *365*, 1108–1113. [[CrossRef](#)]
35. Blanco-Pastor, J.L.; Fernández-Mazuecos, M.; Coello, A.J.; Pastor, J.; Vargas, P. Topography explains the distribution of genetic diversity in one of the most fragile European hotspots. *Divers. Distrib.* **2019**, *25*, 74–89. [[CrossRef](#)]
36. Muscarella, R.; Kolyaie, S.; Morton, D.C.; Zimmerman, J.K.; Uriarte, M. Effects of topography on tropical forest structure depend on climate context. *J. Ecol.* **2020**, *108*, 145–159. [[CrossRef](#)]
37. Stein, A.; Gerstner, K.; Kreft, H. Environmental heterogeneity as a universal driver of species richness across taxa, biomes and spatial scales. *Ecol. Lett.* **2014**, *17*, 866–880. [[CrossRef](#)]
38. Schrodte, F.; Santos, M.J.; Bailey, J.J.; Field, R. Challenges and opportunities for biogeography—What can we still learn from von Humboldt? *J. Biogeogr.* **2019**, *46*, 1631–1642. [[CrossRef](#)]
39. Barbarella, M.; Cuomo, A.; Di Benedetto, A.; Fiani, M.; Guida, D. Topographic Base Maps from Remote Sensing Data for Engineering Geomorphological Modelling: An Application on Coastal Mediterranean Landscape. *Geosciences* **2019**, *9*, 500. [[CrossRef](#)]
40. Capolongo, D.; Refice, A.; Bocchiola, D.; D'Addabbo, A.; Vouvalidis, K.; Soncini, A.; Zingaro, M.; Bovenga, F.; Stamatopoulos, L. Coupling multitemporal remote sensing with geomorphology and hydrological modeling for post flood recovery in the Strymonas dammed river basin (Greece). *Sci. Total Environ.* **2019**, *651*, 1958–1968. [[CrossRef](#)]
41. Leitão, P.J.; Santos, M.J. Improving Models of Species Ecological Niches: A Remote Sensing Overview. *Front. Ecol. Evol.* **2019**, *7*, 1–7. [[CrossRef](#)]
42. Kulp, S.A.; Strauss, B.H. New elevation data triple estimates of global vulnerability to sea-level rise and coastal flooding. *Nat. Commun.* **2019**, *10*, 4844. [[CrossRef](#)] [[PubMed](#)]
43. Parajuli, S.P.; Yang, Z.-L.; Kocurek, G. Mapping erodibility in dust source regions based on geomorphology, meteorology, and remote sensing. *J. Geophys. Res. Earth Surf.* **2014**, *119*, 1977–1994. [[CrossRef](#)]
44. Eegholm, B.H.; Wake, S.; Denny, Z.; Dogoda, P.; Poullos, D.; Coyle, B.; Mule, P.; Hagopian, J.G.; Thompson, P.; Ramos-Izquierdo, L.; et al. Global Ecosystem Dynamics Investigation (GEDI) instrument alignment and test. In Proceedings of the Optical Modeling and System Alignment, San Diego, CA, USA, 12–13 August 2019.
45. Dubayah, R.; Blair, J.B.; Goetz, S.; Fatoyinbo, L.; Hansen, M.; Healey, S.; Hofton, M.; Hurr, G.; Kellner, J.; Luthcke, S.; et al. The Global Ecosystem Dynamics Investigation: High-resolution laser ranging of the Earth's forests and topography. *Sci. Remote Sens.* **2020**, *1*, 100002. [[CrossRef](#)]
46. Krieger, G.; Pardini, M.; Schulze, D.; Bachmann, M.; Borla Tridon, D.; Reimann, J.; Brautigam, B.; Steinbrecher, U.; Tienda, C.; Sanjuan Ferrer, M.; et al. Tandem-L: Main results of the phase a feasibility study. In Proceedings of the 2016 IEEE International Geoscience and Remote Sensing Symposium (IGARSS), Beijing, China, 10–15 July 2016; IEEE. pp. 2116–2119.
47. Moreira, A.; Krieger, G.; Gonzalez, C.; Nannini, M.; Zink, M. Tandem-L: A Highly Innovative Bistatic SAR Mission for Monitoring Earth's System Dynamics. *Geophys. Res. Abstr.* **2019**, *21*, 2019.
48. Rast, M.; Painter, T.H. Earth Observation Imaging Spectroscopy for Terrestrial Systems: An Overview of Its History, Techniques, and Applications of Its Missions. *Surv. Geophys.* **2019**, *40*, 303–331. [[CrossRef](#)]
49. Nieke, J.; Rast, M. Towards the Copernicus Hyperspectral Imaging Mission For The Environment (CHIME). In Proceedings of the IGARSS 2018—2018 IEEE International Geoscience and Remote Sensing Symposium, Valencia, Spain, 22–27 July 2018; IEEE. pp. 157–159.
50. Hulley, G.C.; Ghent, D.; Hook, S.J. A Look to the Future: Thermal-Infrared Missions and Measurements. In *Taking the Temperature of the Earth*; Elsevier: Amsterdam, The Netherlands, 2019; pp. 227–237. Available online: <https://www.sciencedirect.com/book/9780128144589/taking-the-temperature-of-the-earth#book-description> (accessed on 22 September 2020).
51. Guanter, L.; Kaufmann, H.; Segl, K.; Foerster, S.; Rogass, C.; Chabrillat, S.; Kuester, T.; Hollstein, A.; Rossner, G.; Chlebek, C.; et al. The EnMAP Spaceborne Imaging Spectroscopy Mission for Earth Observation. *Remote Sens.* **2015**, *7*, 8830–8857. [[CrossRef](#)]
52. Zarnetske, P.L.; Read, Q.D.; Record, S.; Gaddis, K.D.; Pau, S.; Hobi, M.L.; Malone, S.L.; Costanza, J.M.; Dahlin, K.; Latimer, A.M.; et al. Towards connecting biodiversity and geodiversity across scales with satellite remote sensing. *Glob. Ecol. Biogeogr.* **2019**, *28*, 548–556. [[CrossRef](#)]

53. Lausch, A.; Bastian, O.; Klotz, S.; Leitão, P.J.; Jung, A.; Rocchini, D.; Schaepman, M.E.; Skidmore, A.K.; Tischendorf, L.; Knapp, S. Understanding and assessing vegetation health by in situ species and remote-sensing approaches. *Methods Ecol. Evol.* **2018**, *9*, 1799–1809. [[CrossRef](#)]
54. Lausch, A.; Bannehr, L.; Beckmann, M.; Boehm, C.; Feilhauer, H.; Hacker, J.M.; Heurich, M.; Jung, A.; Klenke, R.; Neumann, C.; et al. Linking Earth Observation and taxonomic, structural and functional biodiversity: Local to ecosystem perspectives. *Ecol. Indic.* **2016**, *70*, 317–339. [[CrossRef](#)]
55. Woodcock, C.E.; Allen, R.; Anderson, M.; Belward, A.; Bindschadler, R.; Cohen, W.; Gao, F.; Goward, S.N.; Helder, D.; Helmer, E.; et al. Free Access to Landsat Imagery. *Science* **2008**, *320*, 1011–1012. [[CrossRef](#)]
56. Zhu, Z.; Wulder, M.A.; Roy, D.P.; Woodcock, C.E.; Hansen, M.C.; Radeloff, V.C.; Healey, S.P.; Schaaf, C.; Hostert, P.; Strobl, P.; et al. Benefits of the free and open Landsat data policy. *Remote Sens. Environ.* **2019**, *224*, 382–385. [[CrossRef](#)]
57. Wulder, M.A.; Loveland, T.R.; Roy, D.P.; Crawford, C.J.; Masek, J.G.; Woodcock, C.E.; Allen, R.G.; Anderson, M.C.; Belward, A.S.; Cohen, W.B.; et al. Current status of Landsat program, science, and applications. *Remote Sens. Environ.* **2019**, *225*, 127–147. [[CrossRef](#)]
58. Masek, J.G.; Wulder, M.A.; Markham, B.; McCorkel, J.; Crawford, C.J.; Storey, J.; Jenstrom, D.T. Landsat 9: Empowering open science and applications through continuity. *Remote Sens. Environ.* **2020**, *248*, 111968. [[CrossRef](#)]
59. Dlamini, S.N.; Beloconi, A.; Mabaso, S.; Vounatsou, P.; Impouma, B.; Fall, I.S. Review of remotely sensed data products for disease mapping and epidemiology. *Remote Sens. Appl. Soc. Environ.* **2019**, *14*, 108–118. [[CrossRef](#)]
60. Tromp-van Meerveld, H.J.; McDonnell, J.J. On the interrelations between topography, soil depth, soil moisture, transpiration rates and species distribution at the hillslope scale. *Adv. Water Resour.* **2006**, *29*, 293–310. [[CrossRef](#)]
61. Bardgett, R.D.; Wardle, D.A. *Aboveground-Belowground Linkages: Biotic Interactions, Ecosystem Processes, and Global Change*; Oxford University Press: Oxford, UK, 2010; ISBN 0199546886.
62. Skidmore, A.K. A comparison of techniques for calculating gradient and aspect from a gridded digital elevation model. *Int. J. Geogr. Inf. Syst.* **1989**, *3*, 323–334. [[CrossRef](#)]
63. Skidmore, A.K. Terrain position as mapped from a gridded digital elevation model. *Int. J. Geogr. Inf. Syst.* **1990**, *4*, 33–49. [[CrossRef](#)]
64. McLean, K.A.; Trainor, A.M.; Asner, G.P.; Crofoot, M.C.; Hopkins, M.E.; Campbell, C.J.; Martin, R.E.; Knapp, D.E.; Jansen, P.A. Movement patterns of three arboreal primates in a Neotropical moist forest explained by LiDAR-estimated canopy structure. *Landsc. Ecol.* **2016**, *31*, 1849–1862. [[CrossRef](#)]
65. Broadbent, E.N.; Zambrano, A.M.A.; Asner, G.P.; Field, C.B.; Rosenheim, B.E.; Kennedy-Bowdoin, T.; Knapp, D.E.; Burke, D.; Giardina, C.; Cordell, S. Linking rainforest ecophysiology and microclimate through fusion of airborne LiDAR and hyperspectral imagery. *Ecosphere* **2014**, *5*, art57. [[CrossRef](#)]
66. Lembrechts, J.J.; Nijs, I.; Lenoir, J. Incorporating microclimate into species distribution models. *Ecography* **2019**, *42*, 1267–1279. [[CrossRef](#)]
67. Murrian, M.J.; Gonzalez, C.W.; Humphreys, T.E.; Novlan, T.D. A dense reference network for mass-market centimeter-accurate positioning. In Proceedings of the 2016 IEEE/ION Position, Savannah, Georgia, USA, 11–16 April 2016; IEEE. pp. 243–254.
68. Ancillao, A. Stereophotogrammetry in Functional Evaluation: History and Modern Protocols. In *SpringerBriefs in Applied Sciences and Technology*; Springer: Rome, Italy, 2018; pp. 1–29.
69. Rosen, P.A.; Hensley, S.; Gurrola, E.; Rogez, F.; Chan, S.; Martin, J.; Rodriguez, E. SRTM C-band topographic data: Quality assessments and calibration activities. In Proceedings of the IGARSS 2001. Scanning the Present and Resolving the Future. Proceedings. IEEE 2001 International Geoscience and Remote Sensing Symposium (Cat. No.01CH37217), Sydney, NSW, Australia, 9–13 July 2001; 2001; Volume 2, pp. 739–741.
70. McElroy, J.L.; Eckert, J.A.; Hager, C.J. Airborne downlooking lidar measurements during state 78. *Atmos. Environ.* **1981**, *15*, 2223–2230. [[CrossRef](#)]
71. Okyay, U.; Telling, J.; Glennie, C.L.; Dietrich, W.E. Airborne lidar change detection: An overview of Earth sciences applications. *Earth-Science Rev.* **2019**, *198*, 102929. [[CrossRef](#)]
72. Pieraccini, M.; Miccinesi, L. Ground-Based Radar Interferometry: A Bibliographic Review. *Remote Sens.* **2019**, *11*, 1029. [[CrossRef](#)]

73. Strozzi, T.; Kaab, A.; Frauenfelder, R.; Wegmuller, U. Detection and monitoring of unstable high-mountain slopes with L-band SAR interferometry. In Proceedings of the IGARSS 2003. 2003 IEEE International Geoscience and Remote Sensing Symposium. Proceedings (IEEE Cat. No.03CH37477), Toulouse, France, 21–25 July 2003; IEEE. Volume 3, pp. 1852–1854.
74. Tang, P.; Chen, F.; Tian, B.; Zhang, H.; Miao, Z.; Wang, Q.; Zhou, W. Monitoring of surface instability in tourist zones in Sanya (China) using high-resolution SAR interferometry. *Remote Sens. Lett.* **2019**, *10*, 129–138. [[CrossRef](#)]
75. Mashaly, J.; Ghoneim, E. Flash Flood Hazard Using Optical, Radar, and Stereo-Pair Derived DEM: Eastern Desert, Egypt. *Remote Sens.* **2018**, *10*, 1204. [[CrossRef](#)]
76. Capaldo, P.; Nascetti, A.; Porfiri, M.; Pieralice, F.; Fratarcangeli, F.; Crespi, M.; Toutin, T. Evaluation and comparison of different radargrammetric approaches for Digital Surface Models generation from COSMO-SkyMed, TerraSAR-X, RADARSAT-2 imagery: Analysis of Beauport (Canada) test site. *ISPRS J. Photogramm. Remote Sens.* **2015**, *100*, 60–70. [[CrossRef](#)]
77. Cook, K.L. An evaluation of the effectiveness of low-cost UAVs and structure from motion for geomorphic change detection. *Geomorphology* **2017**, *278*, 195–208. [[CrossRef](#)]
78. Manfreda, S.; McCabe, M.F.; Miller, P.E.; Lucas, R.; Madrigal, V.P.; Mallinis, G.; Ben Dor, E.; Helman, D.; Estes, L.; Ciraolo, G.; et al. On the use of unmanned aerial systems for environmental monitoring. *Remote Sens.* **2018**, *10*, 641. [[CrossRef](#)]
79. Manfreda, S.; Dvorak, P.; Mullerova, J.; Herban, S.; Vuono, P.; Juan, J.; Justel, A.; Perks, M. Accuracy Assessment on Unmanned Aerial System Derived Digital Surface Models. *Preprints* **2018**, *2018*, 2018090579.
80. Ewertowski, M.W.; Tomczyk, A.M.; Evans, D.J.A.; Roberts, D.H.; Ewertowski, W. Operational Framework for Rapid, Very-high Resolution Mapping of Glacial Geomorphology Using Low-cost Unmanned Aerial Vehicles and Structure-from-Motion Approach. *Remote Sens.* **2019**, *11*, 65. [[CrossRef](#)]
81. Suomalainen, J.; Anders, N.; Iqbal, S.; Roerink, G.; Franke, J.; Wenting, P.; Hünninger, D.; Bartholomeus, H.; Becker, R.; Kooistra, L. A lightweight hyperspectral mapping system and photogrammetric processing chain for unmanned aerial vehicles. *Remote Sens.* **2014**, *6*, 11013–11030. [[CrossRef](#)]
82. Westoby, M.J.; Brasington, J.; Glasser, N.F.; Hambrey, M.J.; Reynolds, J.M. “Structure-from-Motion” photogrammetry: A low-cost, effective tool for geoscience applications. *Geomorphology* **2012**, *179*, 300–314. [[CrossRef](#)]
83. Forsmo, J.; Anderson, K.; Macleod, C.J.A.; Wilkinson, M.E.; DeBell, L.; Brazier, R.E. Structure from motion photogrammetry in ecology: Does the choice of software matter? *Ecol. Evol.* **2019**, *9*, 12964–12979. [[CrossRef](#)] [[PubMed](#)]
84. Anderson, K.; Westoby, M.J.; James, M.R. Low-budget topographic surveying comes of age: Structure from motion photogrammetry in geography and the geosciences. *Prog. Phys. Geogr.* **2019**, *43*, 163–173. [[CrossRef](#)]
85. Kröhnert, M.; Anderson, R.; Bumberger, J.; Dietrich, P.; Harpole, W.S.; Maas, H.-G. WATCHING GRASSGROW - A PILOT STUDY ON THE SUITABILITY OF PHOTOGRAMMETRIC TECHNIQUES FOR QUANTIFYING CHANGE IN ABOVEGROUND BIOMASS IN GRASSLAND EXPERIMENTS. *ISPRS Int. Arch. Photogramm. Remote Sens. Spat. Inf. Sci.* **2018**, *XLII-2*, 539–542.
86. Thiel, C.; Baade, J.; Schmuilius, C. Comparison of UAV photograph-based and airborne lidar-based point clouds over forest from a forestry application perspective. *Int. J. Remote Sens.* **2017**, *38*, 2411–2426. [[CrossRef](#)]
87. Tachikawa, T.; Hato, M.; Kaku, M.; Iwasaki, A. Characteristics of ASTER GDEM version 2. In Proceedings of the 2011 IEEE International Geoscience and Remote Sensing Symposium, Vancouver, BC, Canada, 24–29 July 2011; IEEE. pp. 3657–3660.
88. Gesch, D.; Oimoen, M.; Danielson, J.; Meyer, D. Validation of the ASTER global digital elevation model version 3 over the Conterminous United States. *Int. Arch. Photogramm. Remote Sens. Spat. Inf. Sci. ISPRS Arch.* **2016**, *41*, 143–148. [[CrossRef](#)]
89. Tadono, T.; Shimada, M. Calibration of PRISM and AVNIR-2 onboard ALOS “Daichi”. *IEEE Trans. Geosci. Remote Sens.* **2009**, *47*, 4042–4050. [[CrossRef](#)]
90. Takaku, J.; Tadono, T.; Tsutsui, K. Generation of high resolution global DSM from ALOS PRISM. *Int. Arch. Photogramm. Remote Sens. Spat. Inf. Sci. ISPRS Arch.* **2014**, *40*, 243–248. [[CrossRef](#)]
91. Aldosari, A.A.; Jacobsen, K. Quality of Height Models Covering Large Areas. *PFG J. Photogramm. Remote Sens. Geoinf. Sci.* **2019**, *87*, 177–190. [[CrossRef](#)]
92. Alganci, U.; Besol, B.; Sertel, E. Accuracy Assessment of Different Digital Surface Models. *ISPRS Int. J. Geo-Inf.* **2018**, *7*, 114. [[CrossRef](#)]

93. Hajnsek, I.; Pottier, E.; Cloude, S.R. Inversion of surface parameters from polarimetric SAR. *IEEE Trans. Geosci. Remote Sens.* **2003**, *41*, 727–744. [[CrossRef](#)]
94. Zebker, H.A.; Goldstein, R.M. Topographic mapping from interferometric synthetic aperture radar observations. *J. Geophys. Res.* **1986**, *91*, 4993. [[CrossRef](#)]
95. Graham, L.C. Synthetic Interferometer Radar For Topographic Mapping. *Proc. IEEE* **1974**, *62*, 763–768. [[CrossRef](#)]
96. Hagberg, J.O.; Ulander, L.M.H.; Askne, J. Repeat-pass SAR interferometry over forested terrain. *IEEE Trans. Geosci. Remote Sens.* **1995**, *33*, 331–340. [[CrossRef](#)]
97. Hyyppä, J.; Hallikainen, M. A Helicopter-Borne Eight-Channel Ranging Scatterometer for Remote Sensing: Part I System Description. *IEEE Trans. Geosci. Remote Sens.* **1993**, *31*, 170–179. [[CrossRef](#)]
98. Thiel, C.; Schmullius, C. Investigating ALOS PALSAR interferometric coherence in central Siberia at unfrozen and frozen conditions: Implications for forest growing stock volume estimation. *Can. J. Remote Sens.* **2013**, *39*, 232–250. [[CrossRef](#)]
99. Thiel, C.; Schmullius, C. Investigating the impact of freezing on the ALOS PALSAR InSAR phase over Siberian forests. *Remote Sens. Lett.* **2013**, *4*, 900–909. [[CrossRef](#)]
100. Chowdhury, T.A.; Thiel, C.; Schmullius, C. Growing stock volume estimation from L-band ALOS PALSAR polarimetric coherence in Siberian forest. *Remote Sens. Environ.* **2014**, *155*, 129–144. [[CrossRef](#)]
101. Crippen, R.; Buckley, S.; Agram, P.; Belz, E.; Gurrola, E.; Hensley, S.; Kobrick, M.; Lavalle, M.; Martin, J.; Neumann, M.; et al. Nasadem Global Elevation Model: Methods and Progress. *ISPRS Int. Arch. Photogramm. Remote Sens. Spat. Inf. Sci.* **2016**, *XLI-B4*, 125–128. [[CrossRef](#)]
102. Simard, M.; Neumann, M.; Buckley, S. Validation of the New Srtm Digital Elevation Model (Nasadem) with Icesat/Glas over the United States. *IEEE Int. Geosci. Remote Sens. Symp.* **2016**, 3227–3229. [[CrossRef](#)]
103. Wessel, B.; Huber, M.; Wohlfart, C.; Marschalk, U.; Kosmann, D.; Roth, A. Accuracy assessment of the global TanDEM-X Digital Elevation Model with GPS data. *ISPRS J. Photogramm. Remote Sens.* **2018**, *139*, 171–182. [[CrossRef](#)]
104. Tansey, K.J.; Luckman, A.J.; Skinner, L.; Balzter, H.; Strozzi, T.; Wagner, W. Classification of forest volume resources using ERS tandem coherence and JERS backscatter data. *Int. J. Remote Sens.* **2004**, *25*, 751–768. [[CrossRef](#)]
105. Gens, R.; Van Genderen, J.L. Review Article SAR interferometry—issues, techniques, applications. *Int. J. Remote Sens.* **1996**, *17*, 1803–1835. [[CrossRef](#)]
106. Crosetto, M.; Monserrat, O.; Cuevas, M.; Crippa, B. Spaceborne Differential SAR Interferometry: Data Analysis Tools for Deformation Measurement. *Remote Sens.* **2011**, *3*, 305–318. [[CrossRef](#)]
107. Le Toan, T.; Quegan, S.; Davidson, M.W.J.; Balzter, H.; Paillou, P.; Papathanassiou, K.; Plummer, S.; Rocca, F.; Saatchi, S.; Shugart, H.; et al. The BIOMASS mission: Mapping global forest biomass to better understand the terrestrial carbon cycle. *Remote Sens. Environ.* **2011**, *115*, 2850–2860. [[CrossRef](#)]
108. Quegan, S.; Le Toan, T.; Chave, J.; Dall, J.; Exbrayat, J.-F.; Minh, D.H.T.; Lomas, M.; D’Alessandro, M.M.; Paillou, P.; Papathanassiou, K.; et al. The European Space Agency BIOMASS mission: Measuring forest above-ground biomass from space. *Remote Sens. Environ.* **2019**, *227*, 44–60. [[CrossRef](#)]
109. Crosetto, M.; Monserrat, O.; Cuevas-González, M.; Devanthery, N.; Crippa, B. Persistent Scatterer Interferometry: A review. *ISPRS J. Photogramm. Remote Sens.* **2016**, *115*, 78–89. [[CrossRef](#)]
110. Zhong, C.; Liu, Y.; Gao, P.; Chen, W.; Li, H.; Hou, Y.; Nuremanguli, T.; Ma, H. Landslide mapping with remote sensing: Challenges and opportunities. *Int. J. Remote Sens.* **2020**, *41*, 1555–1581. [[CrossRef](#)]
111. Solari, L.; Bianchini, S.; Franceschini, R.; Barra, A.; Monserrat, O.; Thuegaz, P.; Bertolo, D.; Crosetto, M.; Catani, F. Satellite interferometric data for landslide intensity evaluation in mountainous regions. *Int. J. Appl. Earth Obs. Geoinf.* **2020**, *87*, 102028. [[CrossRef](#)]
112. Dirscherl, M.; Dietz, A.J.; Dech, S.; Kuenzer, C. Remote sensing of ice motion in Antarctica—A review. *Remote Sens. Environ.* **2020**, *237*, 111595. [[CrossRef](#)]
113. Salepci, N. Multi-Sensor Synergy For Persistent Scatterer Interferometry Based Ground Subsidence Monitoring, PhD at the Friedrich-Schiller-University of Jena, Chemical-Geoscientific Faculty. 2015. Available online: https://www.db-thueringen.de/receive/dbt_mods_00026315 (accessed on 7 November 2020).
114. Höfle, B.; Rutzinger, M. Topographic airborne LiDAR in geomorphology: A technological perspective. *Zeitschrift für Geomorphol.* **2011**, *55*, 1–29. [[CrossRef](#)]
115. Riveiro, B. *Laser Scanning*; Riveiro, B., Lindenbergh, R., Eds.; CRC Press: London, UK, 2019; ISBN 9781351018869. [[CrossRef](#)]

116. Hudak, A.T.; Lefsky, M.A.; Cohen, W.B.; Berterretche, M. Integration of lidar and Landsat ETM+ data for estimating and mapping forest canopy height. *Remote Sens. Environ.* **2002**, *82*, 397–416. [CrossRef]
117. Hudak, A.T.; Evans, J.S.; Stuart Smith, A.M. LiDAR Utility for Natural Resource Managers. *Remote Sens.* **2009**, *1*, 934–951. [CrossRef]
118. Brodu, N.; Lague, D. 3D terrestrial lidar data classification of complex natural scenes using a multi-scale dimensionality criterion: Applications in geomorphology. *ISPRS J. Photogramm. Remote Sens.* **2012**, *68*, 121–134. [CrossRef]
119. Guzzetti, F.; Mondini, A.C.; Cardinali, M.; Fiorucci, F.; Santangelo, M.; Chang, K.-T. Landslide inventory maps: New tools for an old problem. *Earth-Science Rev.* **2012**, *112*, 42–66. [CrossRef]
120. Telling, J.; Lyda, A.; Hartzell, P.; Glennie, C. Review of Earth science research using terrestrial laser scanning. *Earth-Science Rev.* **2017**, *169*, 35–68. [CrossRef]
121. Eltner, A.; Maas, H.; Faust, D. Soil micro-topography change detection at hillslopes in fragile Mediterranean landscapes. *Geoderma* **2018**, *313*, 217–232. [CrossRef]
122. Stysley, P.R.; Coyle, D.B.; Clarke, G.B.; Frese, E.; Blalock, G.; Morey, P.; Kay, R.B.; Poullos, D.; Hersh, M. Laser production for NASA's Global Ecosystem Dynamics Investigation (GEDI) lidar. *Opt. Laser Technol.* **2015**, *68*, 67–72. [CrossRef]
123. Hancock, S.; Armston, J.; Hofton, M.; Sun, X.; Tang, H.; Duncanson, L.I.; Kellner, J.R.; Dubayah, R. The GEDI simulator: A large-footprint waveform lidar simulator for calibration and validation of spaceborne missions. *Earth Sp. Sci.* **2019**, *6*, 2018EA000506. [CrossRef]
124. Markus, T.; Neumann, T.; Martino, A.; Abdalati, W.; Brunt, K.; Csatho, B.; Farrell, S.; Fricker, H.; Gardner, A.; Harding, D.; et al. The Ice, Cloud, and land Elevation Satellite-2 (ICESat-2): Science requirements, concept, and implementation. *Remote Sens. Environ.* **2017**, *190*, 260–273. [CrossRef]
125. Margottini, C.; Canuti, P.; Sassa, K. *Landslide Science and Practice*; Margottini, C., Canuti, P., Sassa, K., Eds.; Springer Berlin Heidelberg: Berlin/Heidelberg, Germany, 2013; ISBN 978-3-642-31444-5.
126. Tilly, N.; Kelterbaum, D.; Zeese, R. GEOMORPHOLOGICAL MAPPING WITH TERRESTRIAL LASER SCANNING AND UAV-BASED IMAGING. *ISPRS Int. Arch. Photogramm. Remote Sens. Spat. Inf. Sci.* **2016**, *XLI-B5*, 591–597. [CrossRef]
127. RIEGL_miniVUX-1UAV. Available online: http://www.riegl.com/uploads/tx_pxpriegldownloads/RIEGL_miniVUX-1UAV_Datasheet_2020-10-06.pdf (accessed on 8 November 2020).
128. Xie, T.; Zhu, J.; Jiang, C.; JIANG, Y.; GUO, W.; WANG, C.; LIU, R. Situation and prospect of light and miniature UAV-borne LiDAR. In Proceedings of the XIV International Conference on Pulsed Lasers and Laser Applications, Tomsk, Russian, 15–20 September 2019; Klimkin, A.V., Tarasenko, V.F., Trigub, M.V., Eds.; SPIE: Tomsk, Russian Federation, 2019; p. 20.
129. Jeziorska, J. UAS for Wetland Mapping and Hydrological Modeling. *Remote Sens.* **2019**, *11*, 1997. [CrossRef]
130. Lefsky, M.A.; Harding, D.J.; Keller, M.; Cohen, W.B.; Carabajal, C.C.; Del Bom Espirito-Santo, F.; Hunter, M.O.; de Oliveira, R. Estimates of forest canopy height and aboveground biomass using ICESat. *Geophys. Res. Lett.* **2005**, *32*, 1–4. [CrossRef]
131. Drake, J.B.; Dubayah, R.O.; Clark, D.B.; Knox, R.G.; Blair, J.B.; Hofton, M.A.; Chazdon, R.L.; Weishampel, J.F.; Prince, S. Estimation of tropical forest structural characteristics, using large-footprint lidar. *Remote Sens. Environ.* **2002**, *79*, 305–319. [CrossRef]
132. Duncanson, L.; Neuenschwander, A.; Hancock, S.; Thomas, N.; Fatoyinbo, T.; Simard, M.; Silva, C.A.; Armston, J.; Luthcke, S.B.; Hofton, M.; et al. Biomass estimation from simulated GEDI, ICESat-2 and NISAR across environmental gradients in Sonoma County, California. *Remote Sens. Environ.* **2020**, *242*, 111779. [CrossRef]
133. Vandemark, D.; Tran, N.; Beckley, B.D.; Chapron, B.; Gaspar, P. Direct estimation of sea state impacts on radar altimeter sea level measurements. *Geophys. Res. Lett.* **2002**, *29*, 1-1–1-4. [CrossRef]
134. Hawker, L.; Bates, P.; Neal, J.; Rougier, J. Perspectives on Digital Elevation Model (DEM) Simulation for Flood Modeling in the Absence of a High-Accuracy Open Access Global DEM. *Front. Earth Sci.* **2018**, *6*, 233. [CrossRef]
135. Schwefel, D.; Glässer, C.; Glässer, W. Dynamik anthropogen induzierter Landschaftsveränderungen im Bergbaufolgegebiet Teutschenthal-Bahnhof (Sachsen-Anhalt). *Hercynia* **2012**, *45*, 9–31.
136. Mulder, V.L.; de Bruin, S.; Schaepman, M.E.; Mayr, T.R. The use of remote sensing in soil and terrain mapping — A review. *Geoderma* **2011**, *162*, 1–19. [CrossRef]

137. Fassnacht, F.E.; Latifi, H.; Stereńczak, K.; Modzelewska, A.; Lefsky, M.; Waser, L.T.; Straub, C.; Ghosh, A. Review of studies on tree species classification from remotely sensed data. *Remote Sens. Environ.* **2016**, *186*, 64–87. [[CrossRef](#)]
138. Cavender-Bares, J.; Gamon, J.A.; Townsend, P.A. *Remote Sensing of Plant Biodiversity*; Cavender-Bares, J., Gamon, J.A., Townsend, P.A., Eds.; Springer International Publishing: Cham, Switzerland, 2020; ISBN 978-3-030-33156-6.
139. Lausch, A.; Erasmi, S.; King, D.J.; Magdon, P.; Heurich, M. Understanding Forest Health with Remote Sensing -Part I—A Review of Spectral Traits, Processes and Remote-Sensing Characteristics. *Remote Sens.* **2016**, *8*, 1029. [[CrossRef](#)]
140. Lausch, A.; Erasmi, S.; King, D.; Magdon, P.; Heurich, M. Understanding Forest Health with Remote Sensing-Part II—A Review of Approaches and Data Models. *Remote Sens.* **2017**, *9*, 129. [[CrossRef](#)]
141. Wellmann, T.; Haase, D.; Knapp, S.; Salbach, C.; Selsam, P.; Lausch, A. Urban land use intensity assessment: The potential of spatio-temporal spectral traits with remote sensing. *Ecol. Indic.* **2018**, *85*, 190–203. [[CrossRef](#)]
142. Haase, D.; Jänicke, C.; Wellmann, T. Front and back yard green analysis with subpixel vegetation fractions from earth observation data in a city. *Landsc. Urban Plan.* **2019**, *182*, 44–54. [[CrossRef](#)]
143. Bai, Z.G.; Dent, D.L.; Olsson, L.; Schaeppman, M.E. Proxy global assessment of land degradation. *Soil Use Manag.* **2008**, *24*, 223–234. [[CrossRef](#)]
144. Borrelli, P.; Robinson, D.A.; Fleischer, L.R.; Lugato, E.; Ballabio, C.; Alewell, C.; Meusburger, K.; Modugno, S.; Schütt, B.; Ferro, V.; et al. An assessment of the global impact of 21st century land use change on soil erosion. *Nat. Commun.* **2017**, *8*, 2013. [[CrossRef](#)]
145. Cherlet, M.; Hutchinson, C.; Reynolds, J.; Hill, J.; Sommer, S.; von Maltitz, G. *World Atlas of Desertification*; Publication Office of the European Union: Luxembourg, 2018.
146. FAO. Global Land Degradation Information System (GLADIS). Available online: http://www.fao.org/nr/lada/gladis/gladis_db/downl.php (accessed on 17 June 2020).
147. BMZ Presseservic. Available online: http://www.bmz.de/de/presse/aktuelleMeldungen/2019/juni/190614_pm_034_Minister-Mueller-zum-Internationalen-Tag-gegen-Wuestenbildung/index.html (accessed on 17 June 2020).
148. Webb, N.P.; Kachergis, E.; Miller, S.W.; McCord, S.E.; Bestelmeyer, B.T.; Brown, J.R.; Chappell, A.; Edwards, B.L.; Herrick, J.E.; Karl, J.W.; et al. Indicators and benchmarks for wind erosion monitoring, assessment and management. *Ecol. Indic.* **2020**, *110*, 105881. [[CrossRef](#)]
149. Livingstone, I.; Wiggs, G.F.S.; Weaver, C.M. Geomorphology of desert sand dunes: A review of recent progress. *Earth-Science Rev.* **2007**, *80*, 239–257. [[CrossRef](#)]
150. Zheng, Z.; Du, S.; Du, S.; Zhang, X. A multiscale approach to delineate dune-field landscape patches. *Remote Sens. Environ.* **2020**, *237*, 111591. [[CrossRef](#)]
151. Baughman, C.A.; Jones, B.M.; Bodony, K.L.; Mann, D.H.; Larsen, C.F.; Himelstoss, E.; Smith, J. Remotely Sensing the Morphometrics and Dynamics of a Cold Region Dune Field Using Historical Aerial Photography and Airborne LiDAR Data. *Remote Sens.* **2018**, *10*, 792. [[CrossRef](#)]
152. Blumberg, D.G. Analysis of large aeolian (wind-blown) bedforms using the Shuttle Radar Topography Mission (SRTM) digital elevation data. *Remote Sens. Environ.* **2006**, *100*, 179–189. [[CrossRef](#)]
153. Al-Masrahy, M.A.; Mountney, N.P. Remote sensing of spatial variability in aeolian dune and interdune morphology in the Rub' Al-Khali, Saudi Arabia. *Aeolian Res.* **2013**, *11*, 155–170. [[CrossRef](#)]
154. Ewing, R.C.; Kocurek, G.; Lake, L.W. Pattern analysis of dune-field parameters. *Earth Surf. Process. Landforms* **2006**, *31*, 1176–1191. [[CrossRef](#)]
155. Sharma, P.; Heggy, E.; Farr, T.G. Exploring morphology, layering and formation history of linear terrestrial dunes from radar observations: Implications for Titan. *Remote Sens. Environ.* **2018**, *204*, 296–307. [[CrossRef](#)]
156. Liang, P.; Yang, X. Landscape spatial patterns in the Maowusu (Mu Us) Sandy Land, northern China and their impact factors. *Catena* **2016**, *145*, 321–333. [[CrossRef](#)]
157. Forman, R.T.T. Ecologically Sustainable Landscapes: The Role of Spatial Configuration. In *Changing Landscapes: An Ecological Perspective*; Springer: New York, NY, USA, 1990; pp. 261–278.
158. Lausch, A.; Blaschke, T.; Haase, D.; Herzog, F.; Syrbe, R.-U.; Tischendorf, L.; Walz, U. Understanding and quantifying landscape structure—A review on relevant process characteristics, data models and landscape metrics. *Ecol. Modell.* **2015**, *295*, 31–41. [[CrossRef](#)]

159. Brown, D.G.; Arbogast, A.F. Digital Photogrammetric Change Analysis As Applied To Active Coastal Dunes in Michigan. *Photogramm. Eng. Remote Sens.* **1999**, *65*, 467–474.
160. Ding, C.; Zhang, L.; Liao, M.; Feng, G.; Dong, J.; Ao, M.; Yu, Y. Quantifying the spatio-temporal patterns of dune migration near Minqin Oasis in northwestern China with time series of Landsat-8 and Sentinel-2 observations. *Remote Sens. Environ.* **2020**, *236*, 111498. [[CrossRef](#)]
161. Dong, P.; Chen, Q. *LiDAR Remote Sensing and its Applications*; CRC Press: Boca Raton, FL, USA, 2018; ISBN 978-1-4822-4301-7. [[CrossRef](#)]
162. Mitasova, H.; Overton, M.; Harmon, R.S. Geospatial analysis of a coastal sand dune field evolution: Jockey’s Ridge, North Carolina. *Geomorphology* **2005**, *72*, 204–221. [[CrossRef](#)]
163. Grohmann, C.H.; Sawakuchi, A.O. Influence of cell size on volume calculation using digital terrain models: A case of coastal dune fields. *Geomorphology* **2013**, *180–181*, 130–136. [[CrossRef](#)]
164. Hugenholtz, C.H.; Levin, N.; Barchyn, T.E.; Baddock, M.C. Remote sensing and spatial analysis of aeolian sand dunes: A review and outlook. *Earth-Science Rev.* **2012**, *111*, 319–334. [[CrossRef](#)]
165. Anders, K.; Winiwarter, L.; Lindenbergh, R.; Williams, J.G.; Vos, S.E.; Höfle, B. 4D objects-by-change: Spatiotemporal segmentation of geomorphic surface change from LiDAR time series. *ISPRS J. Photogramm. Remote Sens.* **2020**, *159*, 352–363. [[CrossRef](#)]
166. Wyrick, J.R.; Senter, A.E.; Pasternack, G.B. Revealing the natural complexity of fluvial morphology through 2D hydrodynamic delineation of river landforms. *Geomorphology* **2014**, *210*, 14–22. [[CrossRef](#)]
167. Gopal Ghosh, K.; Mukhopadhyay, S. Introductory Chapter: Current Practice in Fluvial Geomorphology: Research Frontiers, Issues and Challenges. In *Current Practice in Fluvial Geomorphology—Dynamics and Diversity*; IntechOpen: London, UK, 2020; pp. 1–8.
168. Piégay, H.; Arnaud, F.; Belletti, B.; Bertrand, M.; Bizzi, S.; Carbonneau, P.; Dufour, S.; Liébault, F.; Ruiz-Villanueva, V.; Slater, L. Remotely sensed rivers in the Anthropocene: State of the art and prospects. *Earth Surf. Process. Landf.* **2020**, *45*, 157–188.
169. Grimaldi, S.; Xu, J.; Li, Y.; Pauwels, V.R.N.; Walker, J.P. Flood mapping under vegetation using single SAR acquisitions. *Remote Sens. Environ.* **2020**, *237*, 111582. [[CrossRef](#)]
170. UNISDR. CRED Summary for Policymakers. In *Climate Change 2013—The Physical Science Basis*; Intergovernmental Panel on Climate Change, Ed.; Cambridge University Press: Cambridge, UK, 2015; pp. 1–30. ISBN 9788578110796.
171. Tien Bui, D.; Khosravi, K.; Li, S.; Shahabi, H.; Panahi, M.; Singh, V.; Chapi, K.; Shirzadi, A.; Panahi, S.; Chen, W.; et al. New Hybrids of ANFIS with Several Optimization Algorithms for Flood Susceptibility Modeling. *Water* **2018**, *10*, 1210. [[CrossRef](#)]
172. Alfieri, L.; Bisselink, B.; Dottori, F.; Naumann, G.; de Roo, A.; Salamon, P.; Wyser, K.; Feyen, L. Global projections of river flood risk in a warmer world. *Earth’s Future* **2017**, *5*, 171–182. [[CrossRef](#)]
173. Marcus, W.A.; Fonstad, M.A. Optical remote mapping of rivers at sub-meter resolutions and watershed extents. *Earth Surf. Process. Landf.* **2008**, *33*, 4–24. [[CrossRef](#)]
174. Carbonneau, P.E.; Piégay, H. *Fluvial Remote Sensing for Science and Management*; Carbonneau, P.E., Piégay, H., Eds.; John Wiley & Sons, Ltd: Chichester, UK, 2012; ISBN 9781119940791.
175. Tomsett, C.; Leyland, J. Remote sensing of river corridors: A review of current trends and future directions. *River Res. Appl.* **2019**, *35*, 779–803. [[CrossRef](#)]
176. Entwistle, N.; Heritage, G.; Milan, D. Recent remote sensing applications for hydro and morphodynamic monitoring and modelling. *Earth Surf. Process. Landf.* **2018**, *43*, 2283–2291. [[CrossRef](#)]
177. Gläßer, C.; Reinartz, P. Multitemporal and Multispectral Remote Sensing Approach for Flood Detection in the Elbe-Mulde Region 2002. *Acta Hydrochim. Hydrobiol.* **2005**, *33*, 395–403. [[CrossRef](#)]
178. Götze, C.; Gläßer, C.; Jung, A. Detecting heavy metal pollution of floodplain vegetation in a pot experiment using reflectance spectroscopy. *Int. J. River Basin Manag.* **2016**, *14*, 499–507. [[CrossRef](#)]
179. Riedel, F. Der Einsatz Hyperspektraler Fernerkundungsdaten zur Analyse Schwermetallbedingter Boden- und Pflanzenbelastungen in Einem Auenökosystem unter Besonderer Berücksichtigung der Feinmorphologie.—Dissertation, Universität Halle-Wittenberg, 1-226. 2018. Available online: <http://digital.bibliothek.uni-halle.de/hs/content/titleinfo/2923679> (accessed on 7 November 2020).
180. Bizzi, S.; Demarchi, L.; Grabowski, R.C.; Weissteiner, C.J. The use of remote sensing to characterise hydromorphological properties of European rivers. *Aquat. Sci.* **2016**, *78*, 57–70. [[CrossRef](#)]

181. Pekel, J.-F.; Cottam, A.; Gorelick, N.; Belward, A.S. High-resolution mapping of global surface water and its long-term changes. *Nature* **2016**, *540*, 418–422. [[CrossRef](#)]
182. Lee, W.T. *The Face of the Earth as Seen from the Air*; American Geographical Society: New York, NY, USA, 1922.
183. Simpson, R.B. RADAR, GEOGRAPHIC TOOL. *Ann. Assoc. Am. Geogr.* **1966**, *56*, 80–96. [[CrossRef](#)]
184. Short, N.M.; Blair, R.W. *Geomorphology from Space: A Global Overview of Regional Landforms*; Scientific and Technical Information Branch, National Aeronautics and Space Administration: Washington, DC, USA, 1986.
185. Monegaglia, F.; Zolezzi, G.; Güneralp, I.; Henshaw, A.J.; Tubino, M. Automated extraction of meandering river morphodynamics from multitemporal remotely sensed data. *Environ. Model. Softw.* **2018**, *105*, 171–186. [[CrossRef](#)]
186. Gupta, N.; Atkinson, P.M.; Carling, P.A. Decadal length changes in the fluvial planform of the River Ganga: Bringing a mega-river to life with Landsat archives. *Remote Sens. Lett.* **2013**, *4*, 1–9. [[CrossRef](#)]
187. Schumann, G.J.P.; Domeneghetti, A. Exploiting the proliferation of current and future satellite observations of rivers. *Hydrol. Process.* **2016**, *30*, 2891–2896. [[CrossRef](#)]
188. Schumann, G.J.P.; Moller, D.K. Microwave remote sensing of flood inundation. *Phys. Chem. Earth* **2015**, *83–84*, 84–95. [[CrossRef](#)]
189. Ghent, E.O. Application of Remote Sensing and Geographical Information Systems in Flood Management: A Review. *Res. J. Appl. Sci. Eng. Technol.* **2013**, *6*, 1884–1894.
190. Teng, J.; Jakeman, A.J.; Vaze, J.; Croke, B.F.W.; Dutta, D.; Kim, S. Flood inundation modelling: A review of methods, recent advances and uncertainty analysis. *Environ. Model. Softw.* **2017**, *90*, 201–216. [[CrossRef](#)]
191. Ogashawara, I.; Curtarelli, M.P.; Ferreira, C.M. The Use of Optical Remote Sensing For Mapping Flooded Areas. *J. Eng. Res. Appl.* **2013**, *3*, 1956–1960.
192. Shahabi, H.; Shirzadi, A.; Ghaderi, K.; Omidvar, E.; Al-Ansari, N.; Clague, J.J.; Geertsema, M.; Khosravi, K.; Amini, A.; Bahrami, S.; et al. Flood Detection and Susceptibility Mapping Using Sentinel-1 Remote Sensing Data and a Machine Learning Approach: Hybrid Intelligence of Bagging Ensemble Based on K-Nearest Neighbor Classifier. *Remote Sens.* **2020**, *12*, 266. [[CrossRef](#)]
193. Ghoshal, S.; James, L.A.; Singer, M.B.; Aalto, R. Channel and Floodplain Change Analysis over a 100-Year Period: Lower Yuba River, California. *Remote Sens.* **2010**, *2*, 1797–1825. [[CrossRef](#)]
194. Creutin, J.D.; Borga, M. Radar hydrology modifies the monitoring of flash-flood hazard. *Hydrol. Process.* **2003**, *17*, 1453–1456. [[CrossRef](#)]
195. Costache, R.; Pham, Q.B.; Sharifi, E.; Linh, N.T.T.; Abba, S.I.; Vojtek, M.; Vojteková, J.; Nhi, P.T.T.; Khoi, D.N. Flash-Flood Susceptibility Assessment Using Multi-Criteria Decision Making and Machine Learning Supported by Remote Sensing and GIS Techniques. *Remote Sens.* **2019**, *12*, 106. [[CrossRef](#)]
196. Alexandre, C.; Johary, R.; Catry, T.; Mouquet, P.; Révillion, C.; Rakotondraompiana, S.; Pennober, G. A Sentinel-1 Based Processing Chain for Detection of Cyclonic Flood Impacts. *Remote Sens.* **2020**, *12*, 252. [[CrossRef](#)]
197. Zhang, M.; Chen, F.; Tian, B.; Liang, D.; Yang, A. Characterization of Kyagar Glacier and Lake Outburst Floods in 2018 Based on Time-Series Sentinel-1A Data. *Water* **2020**, *12*, 184. [[CrossRef](#)]
198. San Martín, L.; Morandeira, N.S.; Grimson, R.; Rajngewerc, M.; González, E.B.; Kandus, P. The contribution of ALOS/PALSAR-1 multi-temporal data to map permanently and temporarily flooded coastal wetlands. *Int. J. Remote Sens.* **2020**, *41*, 1582–1602. [[CrossRef](#)]
199. Hong Quang, N.; Tuan, V.A.; Thi Thu Hang, L.; Manh Hung, N.; Thi The, D.; Thi Dieu, D.; Duc Anh, N.; Hackney, C.R. Hydrological/Hydraulic Modeling-Based Thresholding of Multi SAR Remote Sensing Data for Flood Monitoring in Regions of the Vietnamese Lower Mekong River Basin. *Water* **2019**, *12*, 71. [[CrossRef](#)]
200. Alsdorf, D.E.; Melack, J.M.; Dunne, T.; Mertes, L.A.K.; Hess, L.L.; Smith, L.C. Interferometric radar measurements of water level changes on the Amazon flood plain. *Nature* **2000**, *404*, 174–177. [[CrossRef](#)]
201. Zeng, Z.; Gan, Y.; Kettner, A.J.; Yang, Q.; Zeng, C.; Brakenridge, G.R.; Hong, Y. Towards high resolution flood monitoring: An integrated methodology using passive microwave brightness temperatures and Sentinel synthetic aperture radar imagery. *J. Hydrol.* **2020**, *582*, 124377. [[CrossRef](#)]
202. Wang, Y.; Colby, J.D.; Mulcahy, K.A. An efficient method for mapping flood extent in a coastal floodplain using Landsat TM and DEM data. *Int. J. Remote Sens.* **2002**, *23*, 3681–3696. [[CrossRef](#)]
203. Himayoun, D.; Roshni, T. Geomorphic changes in the Jhelum River due to an extreme flood event: A case study. *Arab. J. Geosci.* **2020**, *13*, 23. [[CrossRef](#)]

204. Walker, J.J.; Soulard, C.E.; Petrakis, R.E. Integrating stream gage data and Landsat imagery to complete time-series of surface water extents in Central Valley, California. *Int. J. Appl. Earth Obs. Geoinf.* **2020**, *84*, 101973. [[CrossRef](#)]
205. Chadburn, S.E.; Burke, E.J.; Cox, P.M.; Friedlingstein, P.; Hugelius, G.; Westermann, S. An observation-based constraint on permafrost loss as a function of global warming. *Nat. Clim. Chang.* **2017**, *7*, 340–344. [[CrossRef](#)]
206. Goffi, A.; Stroppiana, D.; Brivio, P.A.; Bordogna, G.; Boschetti, M. Towards an automated approach to map flooded areas from Sentinel-2 MSI data and soft integration of water spectral features. *Int. J. Appl. Earth Obs. Geoinf.* **2020**, *84*, 101951. [[CrossRef](#)]
207. Caballero, I.; Ruiz, J.; Navarro, G. Sentinel-2 Satellites Provide Near-Real Time Evaluation of Catastrophic Floods in the West Mediterranean. *Water* **2019**, *11*, 2499. [[CrossRef](#)]
208. Sadek, M.; Li, X. Low-Cost Solution for Assessment of Urban Flash Flood Impacts Using Sentinel-2 Satellite Images and Fuzzy Analytic Hierarchy Process: A Case Study of Ras Ghareb City, Egypt. *Adv. Civ. Eng.* **2019**, *2019*, 1–15. [[CrossRef](#)]
209. Olivera-Guerra, L.; Merlin, O.; Er-Raki, S. Irrigation retrieval from Landsat optical/thermal data integrated into a crop water balance model: A case study over winter wheat fields in a semi-arid region. *Remote Sens. Environ.* **2020**, *239*, 111627. [[CrossRef](#)]
210. Deshpande, S.S. Improved Floodplain Delineation Method Using High-Density LiDAR Data. *Comput. Civ. Infrastruct. Eng.* **2013**, *28*, 68–79. [[CrossRef](#)]
211. Webster, T.L.; Forbes, D.L.; Dickie, S.; Shreenan, R. Using topographic lidar to map flood risk from storm-surge events for Charlottetown, Prince Edward Island, Canada. *Can. J. Remote Sens.* **2004**, *30*, 64–76. [[CrossRef](#)]
212. Fewtrell, T.J.; Duncan, A.; Sampson, C.C.; Neal, J.C.; Bates, P.D. Benchmarking urban flood models of varying complexity and scale using high resolution terrestrial LiDAR data. *Phys. Chem. Earth* **2011**, *36*, 281–291. [[CrossRef](#)]
213. Breili, K.; Simpson, M.J.R.; Klokkervold, E.; Roaldsdotter Ravndal, O. High-accuracy coastal flood mapping for Norway using lidar data. *Nat. Hazards Earth Syst. Sci.* **2020**, *20*, 673–694. [[CrossRef](#)]
214. Stoleriu, C.C.; Urzica, A.; Miha-Pintilie, A. Improving flood risk map accuracy using high-density LiDAR data and the HEC-RAS river analysis system: A case study from north-eastern Romania. *J. Flood Risk Manag.* **2019**, *13*, 1–17. [[CrossRef](#)]
215. Miha-Pintilie, A.; Cîmpianu, C.I.; Stoleriu, C.C.; Pérez, M.N.; Paveluc, L.E. Using high-density LiDAR data and 2D streamflow hydraulic modeling to improve urban flood hazard maps: A HEC-RAS multi-scenario approach. *Water* **2019**, *11*, 1832. [[CrossRef](#)]
216. Jerome Morrissey, P.; McCormack, T.; Naughton, O.; Meredith Johnston, P.; William Gill, L. Modelling groundwater flooding in a lowland karst catchment. *J. Hydrol.* **2020**, *580*, 124361. [[CrossRef](#)]
217. Raber, G.T.; Jensen, J.R.; Hodgson, M.E.; Tullis, J.A.; Davis, B.A.; Berglund, J. Impact of lidar nominal post-spacing on DEM accuracy and flood zone delineation. *Photogramm. Eng. Remote Sensing* **2007**, *73*, 793–804. [[CrossRef](#)]
218. Imam, R.; Pini, M.; Marucco, G.; Dominici, F.; DAVIS, F. UAV-Based GNSS-R for Water Detection as a Support to Flood Monitoring Operations: A Feasibility Study. *Appl. Sci.* **2019**, *10*, 210. [[CrossRef](#)]
219. Bandini, F.; Sunding, T.P.; Linde, J.; Smith, O.; Jensen, I.K.; Köppl, C.J.; Butts, M.; Bauer-Gottwein, P. Unmanned Aerial System (UAS) observations of water surface elevation in a small stream: Comparison of radar altimetry, LIDAR and photogrammetry techniques. *Remote Sens. Environ.* **2020**, *237*, 111487. [[CrossRef](#)]
220. Ielpi, A.; Lapôte, M.G.A. A tenfold slowdown in river meander migration driven by plant life. *Nat. Geosci.* **2020**, *13*, 82–86. [[CrossRef](#)]
221. Mertes, L.A.K.; Daniel, D.L.; Melack, J.M.; Nelson, B.; Martinelli, L.A.; Forsberg, B.R. Spatial patterns of hydrology, geomorphology, and vegetation on the floodplain of the Amazon river in Brazil from a remote sensing perspective. *Geomorphology* **1995**, *13*, 215–232. [[CrossRef](#)]
222. Finotello, A.; D’Alpaos, A.; Bogoni, M.; Ghinassi, M.; Lanzoni, S. Remotely-sensed planform morphologies reveal fluvial and tidal nature of meandering channels. *Sci. Rep.* **2020**, *10*, 1–13. [[CrossRef](#)]
223. Garofalo, D. The Influence of Wetland Vegetation on Tidal Stream Channel Migration and Morphology. *Estuaries* **1980**, *3*, 258. [[CrossRef](#)]
224. Dépret, T.; Riquier, J.; Piégay, H. Evolution of abandoned channels: Insights on controlling factors in a multi-pressure river system. *Geomorphology* **2017**, *294*, 99–118. [[CrossRef](#)]

225. Yang, X.; Damen, M.C.J.; Van Zuidam, R.A. Satellite remote sensing and GIS for the analysis of channel migration changes in the active Yellow River Delta, China. *ITC J.* **1999**, *1*, 146–157. [[CrossRef](#)]
226. Peixoto, J.M.A.; Nelson, B.W.; Wittmann, F. Spatial and temporal dynamics of river channel migration and vegetation in central Amazonian white-water floodplains by remote-sensing techniques. *Remote Sens. Environ.* **2009**, *113*, 2258–2266. [[CrossRef](#)]
227. Yang, C.; Cai, X.; Wang, X.; Yan, R.; Zhang, T.; Zhang, Q.; Lu, X. Remotely sensed trajectory analysis of channel migration in Lower Jingjiang Reach during the period of 1983–2013. *Remote Sens.* **2015**, *7*, 16241–16256. [[CrossRef](#)]
228. Wen, Z.; Yang, H.; Zhang, C.; Shao, G.; Wu, S. Remotely Sensed Mid-Channel Bar Dynamics in Downstream of the Three Gorges Dam, China. *Remote Sens.* **2020**, *12*, 409. [[CrossRef](#)]
229. Thomas, J.; Kumar, S.; Sudheer, K.P. Channel stability assessment in the lower reaches of the Krishna River (India) using multi-temporal satellite data during 1973–2015. *Remote Sens. Appl. Soc. Environ.* **2020**, *17*, 100274. [[CrossRef](#)]
230. Naito, K.; Parker, G. Can Bankfull Discharge and Bankfull Channel Characteristics of an Alluvial Meandering River be Cospecified From a Flow Duration Curve? *J. Geophys. Res. Earth Surf.* **2019**, *124*, 2381–2401. [[CrossRef](#)]
231. Bhaskar, A.S.; Kumar, R.B.B. Remote sensing of coastal geomorphology to understand river migration in the Thengapatnam area, southern India. *Int. J. Remote Sens.* **2011**, *32*, 5287–5301. [[CrossRef](#)]
232. Ielpi, A.; Lapôtre, M.G.A.; Finotello, A.; Ghinassi, M.; D’Alpaos, A. Channel mobility drives a diverse stratigraphic architecture in the dryland Mojave River (California, USA). *Earth Surf. Process. Landf.* **2020**, *45*, 1717–1731. [[CrossRef](#)]
233. Lorenz, R.D.; Lopes, R.M.; Paganelli, F.; Lunine, J.I.; Kirk, R.L.; Mitchell, K.L.; Soderblom, L.A.; Stofan, E.R.; Ori, G.; Myers, M.; et al. Fluvial channels on Titan: Initial Cassini RADAR observations. *Planet. Space Sci.* **2008**, *56*, 1132–1144. [[CrossRef](#)]
234. Zakharova, E.; Nielsen, K.; Kamenev, G.; Kouraev, A. River discharge estimation from radar altimetry: Assessment of satellite performance, river scales and methods. *J. Hydrol.* **2020**, *583*, 124561. [[CrossRef](#)]
235. Tarpanelli, A.; Brocca, L.; Barbeta, S.; Faruolo, M.; Lacava, T.; Moramarco, T. Coupling MODIS and Radar Altimetry Data for Discharge Estimation in Poorly Gauged River Basins. *IEEE J. Sel. Top. Appl. Earth Obs. Remote Sens.* **2015**, *8*, 141–148. [[CrossRef](#)]
236. Smith, L.C.; Pavelsky, T.M. Estimation of river discharge, propagation speed, and hydraulic geometry from space: Lena River, Siberia. *Water Resour. Res.* **2008**, *44*, 1–11. [[CrossRef](#)]
237. Tourian, M.J.; Sneeuw, N.; Bárdossy, A. A quantile function approach to discharge estimation from satellite altimetry (ENVISAT). *Water Resour. Res.* **2013**, *49*, 4174–4186. [[CrossRef](#)]
238. Duró, G.; Crosato, A.; Kleinhans, M.G.; Uijtewaal, W.S.J. Bank erosion processes measured with UAV-SfM along complex banklines of a straight mid-sized river reach. *Earth Surf. Dyn.* **2018**, *6*, 933–953. [[CrossRef](#)]
239. Micheli, E.R.; Kirchner, J.W. Effects of wet meadow riparian vegetation on streambank erosion. 1. Remote sensing measurements of streambank migration and erodibility. *Earth Surf. Process. Landf.* **2002**, *27*, 627–639. [[CrossRef](#)]
240. Heeren, D.M.; Mittelstet, A.R.; Fox, G.A.; Storm, D.E.; Al-Madhhachi, A.T.; Midgley, T.L.; Stringer, A.F.; Stunkel, K.B.; Tejral, R.D. Using Rapid Geomorphic Assessments to Assess Streambank Stability in Oklahoma Ozark Streams. *Trans. ASABE* **2012**, *55*, 957–968. [[CrossRef](#)]
241. Johansen, K.; Grove, J.; Denham, R.; Phinn, S. Assessing stream bank condition using airborne LiDAR and high spatial resolution image data in temperate semirural areas in Victoria, Australia. *J. Appl. Remote Sens.* **2013**, *7*, 073492. [[CrossRef](#)]
242. Resop, J.P.; Lehmann, L.; Hession, W.C. Drone Laser Scanning for Modeling Riverscape Topography and Vegetation: Comparison with Traditional Aerial Lidar. *Drones* **2019**, *3*, 35. [[CrossRef](#)]
243. Hamshaw, S.D.; Bryce, T.; Rizzo, D.M.; O’Neil-Dunne, J.; Frolik, J.; Dewoolkar, M.M. Quantifying streambank movement and topography using unmanned aircraft system photogrammetry with comparison to terrestrial laser scanning. *River Res. Appl.* **2017**, *33*, 1354–1367. [[CrossRef](#)]
244. Meinen, B.U.; Robinson, D.T. Streambank topography: An accuracy assessment of UAV-based and traditional 3D reconstructions. *Int. J. Remote Sens.* **2020**, *41*, 1–18. [[CrossRef](#)]
245. Dürr, H.H.; Laruelle, G.G.; van Kempen, C.M.; Slomp, C.P.; Meybeck, M.; Middelkoop, H. Worldwide Typology of Nearshore Coastal Systems: Defining the Estuarine Filter of River Inputs to the Oceans. *Estuaries Coasts* **2011**, *34*, 441–458. [[CrossRef](#)]

246. Vousdoukas, M.I.; Ranasinghe, R.; Mentaschi, L.; Plomaritis, T.A.; Athanasiou, P.; Luijendijk, A.; Feyen, L. Sandy coastlines under threat of erosion. *Nat. Clim. Chang.* **2020**, *10*, 260–263. [[CrossRef](#)]
247. Boak, E.H.; Turner, I.L. Shoreline Definition and Detection: A Review. *J. Coast. Res.* **2005**, *214*, 688–703. [[CrossRef](#)]
248. Allen, T.; Wang, Y. Selected Scientific Analyses and Practical Applications of Remote Sensing. In *Manual of Geospatial Science and Technology, Second Edition*; CRC Press: Boca Raton, FL, USA, 2010; pp. 467–485.
249. Green, E.P.; Mumby, P.J.; Edwards, A.J.; Clark, C.D. *Remote Sensing Handbook for Tropical Coastal Management*; UNESCO: Paris, France, 2000; ISBN 9231037366.
250. Klemas, V.V. Coastal and Environmental Remote Sensing from Unmanned Aerial Vehicles: An Overview. *J. Coast. Res.* **2015**, *315*, 1260–1267. [[CrossRef](#)]
251. Moore, L.J.; Griggs, G.B. Long-term cliff retreat and erosion hotspots along the central shores of the Monterey Bay National Marine Sanctuary. *Mar. Geol.* **2002**, *181*, 265–283. [[CrossRef](#)]
252. Kanwal, S.; Ding, X.; Sajjad, M.; Abbas, S. Three Decades of Coastal Changes in Sindh, Pakistan (1989–2018): A Geospatial Assessment. *Remote Sens.* **2019**, *12*, 8. [[CrossRef](#)]
253. Ford, M.R.; Dickson, M.E. Detecting ebb-tidal delta migration using Landsat imagery. *Mar. Geol.* **2018**, *405*, 38–46. [[CrossRef](#)]
254. Gong, Z.; Wang, Q.; Guan, H.; Zhou, D.; Zhang, L.; Jing, R.; Wang, X.; Li, Z. Extracting tidal creek features in a heterogeneous background using Sentinel-2 imagery: A case study in the Yellow River Delta, China. *Int. J. Remote Sens.* **2020**, *41*, 3653–3676. [[CrossRef](#)]
255. Kawakubo, F.S.; Morato, R.G.; Nader, R.S.; Luchiani, A. Mapping changes in coastline geomorphic features using Landsat TM and ETM+ imagery: Examples in southeastern Brazil. *Int. J. Remote Sens.* **2011**, *32*, 2547–2562. [[CrossRef](#)]
256. Gens, R. Remote sensing of coastlines: Detection, extraction and monitoring. *Int. J. Remote Sens.* **2010**, *31*, 1819–1836. [[CrossRef](#)]
257. Marghany, M.; Sabu, Z.; Hashim, M. Mapping coastal geomorphology changes using synthetic aperture radar data. *Int. J. Phys. Sci.* **2010**, *5*, 1890–1896.
258. Shu, Y.; Li, J.; Gomes, G. Shoreline Extraction from RADARSAT-2 Intensity Imagery Using a Narrow Band Level Set Segmentation Approach. *Mar. Geod.* **2010**, *33*, 187–203. [[CrossRef](#)]
259. Brock, J.C.; Wright, C.W.; Sallenger, A.H.; Krabill, W.B.; Swift, R.N. Basis and methods of NASA Airborne Topographic Mapper lidar surveys for coastal studies. *J. Coast. Res.* **2002**, *18*, 1–13.
260. Database, C. Available online: <http://database.eohandbook.com/index.aspx> (accessed on 22 September 2020).
261. Müller, F.; Hoffmann-Kroll, R.; Wiggering, H. Indicating ecosystem integrity — theoretical concepts and environmental requirements. *Ecol. Modell.* **2000**, *130*, 13–23. [[CrossRef](#)]
262. Liu, Y.; Zhang, P.; He, Y.; Peng, Z. River detection based on feature fusion from synthetic aperture radar images. *J. Appl. Remote Sens.* **2020**, *14*, 1. [[CrossRef](#)]
263. Emery, C.M.; Paris, A.; Biancamaria, S.; Boone, A.; Calmant, S.; Garambois, P.-A.; Santos da Silva, J. Large-scale hydrological model river storage and discharge correction using a satellite altimetry-based discharge product. *Hydrol. Earth Syst. Sci.* **2018**, *22*, 2135–2162. [[CrossRef](#)]
264. Domeneghetti, A. On the use of SRTM and altimetry data for flood modeling in data-sparse regions. *Water Resour. Res.* **2016**, *52*, 2901–2918. [[CrossRef](#)]
265. Tadono, T.; Ishida, H.; Oda, F.; Naito, S.; Minakawa, K.; Iwamoto, H. Precise Global DEM Generation by ALOS PRISM. *ISPRS Ann. Photogramm. Remote Sens. Spat. Inf. Sci.* **2014**, *II-4*, 71–76. [[CrossRef](#)]
266. DEM, G. Available online: https://insitu.copernicus.eu/library/reports/OverviewofGlobalDEM_i0r7.pdf (accessed on 17 June 2020).
267. ASTER GDEM V3. Available online: https://lpdaac.usgs.gov/documents/434/ASTGTm_User_Guide_V3.pdf (accessed on 17 June 2020).
268. Rizzoli, P.; Martone, M.; Gonzalez, C.; Wecklich, C.; Borla Tridon, D.; Bräutigam, B.; Bachmann, M.; Schulze, D.; Fritz, T.; Huber, M.; et al. Generation and performance assessment of the global TanDEM-X digital elevation model. *ISPRS J. Photogramm. Remote Sens.* **2017**, *132*, 119–139. [[CrossRef](#)]
269. Hawker, L.; Neal, J.; Bates, P. Accuracy assessment of the TanDEM-X 90 Digital Elevation Model for selected floodplain sites. *Remote Sens. Environ.* **2019**, *232*, 111319. [[CrossRef](#)]
270. O’Loughlin, F.E.; Paiva, R.C.D.; Durand, M.; Alsdorf, D.E.; Bates, P.D. A multi-sensor approach towards a global vegetation corrected SRTM DEM product. *Remote Sens. Environ.* **2016**, *182*, 49–59. [[CrossRef](#)]

271. Robinson, N.; Regetz, J.; Guralnick, R.P. EarthEnv-DEM90: A nearly-global, void-free, multi-scale smoothed, 90m digital elevation model from fused ASTER and SRTM data. *ISPRS J. Photogramm. Remote Sens.* **2014**, *87*, 57–67. [[CrossRef](#)]
272. Danielson, J.J.; Gesch, D.B. Global Multi-Resolution Terrain Elevation Data 2010 (GMTED2010), USGS. 2011. Available online: <https://pubs.usgs.gov/of/2011/1073/> (accessed on 7 November 2020).
273. Yamazaki, D.; Ikeshima, D.; Tawatari, R.; Yamaguchi, T.; O’Loughlin, F.; Neal, J.C.; Sampson, C.C.; Kanae, S.; Bates, P.D. A high-accuracy map of global terrain elevations. *Geophys. Res. Lett.* **2017**, *44*, 5844–5853. [[CrossRef](#)]
274. Farr, T.G.; Rosen, P.A.; Caro, E.; Crippen, R.; Duren, R.; Hensley, S.; Kobrick, M.; Paller, M.; Rodriguez, E.; Roth, L.; et al. The Shuttle Radar Topography Mission. *Rev. Geophys.* **2007**, *45*, RG2004. [[CrossRef](#)]
275. DIGITAL ELEVATION DATA. Available online: <http://www.viewfinderpanoramas.org/dem3.html> (accessed on 17 June 2020).
276. Takaku, J.; Tadono, T. Quality updates of ‘AW3D’ global DSM generated from ALOS PRISM. In Proceedings of the 2017 IEEE International Geoscience and Remote Sensing Symposium (IGARSS), Fort Worth, TX, USA, 23–28 July 2017; IEEE. pp. 5666–5669.
277. Tadono, T.; Takaku, J.; Tsutsui, K.; Oda, F.; Nagai, H. Status of “ALOS World 3D (AW3D)” global DSM generation. In Proceedings of the 2015 IEEE International Geoscience and Remote Sensing Symposium (IGARSS), Milan, Italy, 26–31 July 2015; IEEE. pp. 3822–3825.
278. Planetobserver. Available online: <https://www.planetobserver.com/products/planetdem/planetdem-30/> (accessed on 17 June 2020).
279. NEXTMap®Elevation Data Suite. Available online: <https://www.intermap.com/data/nextmap> (accessed on 17 June 2020).
280. Habib, A.; Kim, E.M.; Morgan, M.; Couloigner, I. DEM Generation from High Resolution Satellite Imagery. *Photogramm. Fernerkundung Geoinf.* **2013**, *2013*, 483–493.
281. Nikolakopoulos, K.G.; Kamaratakis, E.K.; Chrysoulakis, N. SRTM vs ASTER elevation products. Comparison for two regions in Crete, Greece. *Int. J. Remote Sens.* **2006**, *27*, 4819–4838. [[CrossRef](#)]
282. Jacobsen, K. Digital Surface Models of City Areas by Very High Resolution Space Imagery. 2006. Available online: https://www.ipi.uni-hannover.de/fileadmin/ipi/publications/City_model_jac.pdf (accessed on 7 November 2020).
283. Toutin, T. Generation of DSMs from SPOT-5 in-track HRS and across-track HRG stereo data using spatiotriangulation and autocalibration. *ISPRS J. Photogramm. Remote Sens.* **2006**, *60*, 170–181. [[CrossRef](#)]
284. Toutin, T. Comparison of 3D Physical and Empirical Models for Generating DSMs from Stereo HR Images. *Photogramm. Eng. Remote Sens.* **2006**, *72*, 597–604. [[CrossRef](#)]
285. Zhang, L.; Gruen, A. Multi-image matching for DSM generation from IKONOS imagery. *ISPRS J. Photogramm. Remote Sens.* **2006**, *60*, 195–211. [[CrossRef](#)]
286. Buyuksalih, G.; Jacobsen, K. Digital surface models in build up areas based on very high resolution space images. *Am. Soc. Photogramm. Remote Sens. ASPRS Annu. Conf. 2007 Identifying Geospatial Solut.* **2007**, *1*, 118–125.
287. Alobeid, A.; Jacobsen, K. Automatic generation of digital surface models from IKONOS stereo imagery and related application. In Proceedings of the GORS 16th International Symposium, Damascus, Syria, 10 November 2008.
288. Crespi, M.; Capaldo, P.; Fratarcangeli, F.; Nascetti, A.; Pieralice, F. DSM generation from very high optical and radar sensors: Problems and potentialities along the road from the 3D geometric modeling to the Surface Model. In Proceedings of the 2010 IEEE International Geoscience and Remote Sensing Symposium, Honolulu, HI, USA, 25–30 July 2010; IEEE. pp. 3596–3599.
289. Capaldo, P.; Crespi, M.; Fratarcangeli, F.; Nascetti, A.; Pieralic, F.; Agugiario, G.; Poli, D.; Remondino, F. DSM generation from optical and SAR high resolution satellite imagery: Methodology, problems and potentialities. In Proceedings of the 2012 IEEE International Geoscience and Remote Sensing Symposium, Munich, Germany, 22–27 July 2012; IEEE. 2012; pp. 6936–6939.
290. Gong, K.; Fritsch, D. A detailed study about digital surface model generation using high resolution satellite stereo imagery. *ISPRS Ann. Photogramm. Remote Sens. Spat. Inf. Sci.* **2016**, *III-1*, 69–76. [[CrossRef](#)]
291. Yu, M.; Huang, Y.; Xu, Q.; Guo, P.; Dai, Z. Application of virtual earth in 3D terrain modeling to visual analysis of large-scale geological disasters in mountainous areas. *Environ. Earth Sci.* **2016**, *75*, 563. [[CrossRef](#)]

292. Huang, Y.; Yu, M.; Xu, Q.; Sawada, K.; Moriguchi, S.; Yashima, A.; Liu, C.; Xue, L. InSAR-derived digital elevation models for terrain change analysis of earthquake-triggered flow-like landslides based on ALOS/PALSAR imagery. *Environ. Earth Sci.* **2015**, *73*, 7661–7668. [[CrossRef](#)]
293. Purinton, B.; Bookhagen, B. Validation of digital elevation models (DEMs) and comparison of geomorphic metrics on the southern Central Andean Plateau. *Earth Surf. Dyn.* **2017**, *5*, 211–237. [[CrossRef](#)]
294. Vassilaki, D.I.; Stamos, A.A. TanDEM-X DEM: Comparative performance review employing LIDAR data and DSMs. *ISPRS J. Photogramm. Remote Sens.* **2020**, *160*, 33–50. [[CrossRef](#)]
295. Zink, M.; Fiedler, H.; Hajnsek, I.; Krieger, G.; Moreira, A.; Werner, M. The TanDEM-X Mission Concept. In Proceedings of the 2006 IEEE International Symposium on Geoscience and Remote Sensing, Denver, CO, USA, 31 July–4 August 2006; IEEE. pp. 1938–1941.
296. Potin, P.; Rosich, B.; Roeder, J.; Bargellini, P. Sentinel-1 Mission operations concept. In Proceedings of the 2014 IEEE Geoscience and Remote Sensing Symposium, Quebec City, QC, Canada, IEEE. 13–18 July 2014; pp. 1465–1468.
297. Rosenqvist, A.; Shimada, M.; Ito, N.; Watanabe, M. ALOS PALSAR: A pathfinder mission for global-scale monitoring of the environment. *IEEE Trans. Geosci. Remote Sens.* **2007**, *45*, 3307–3316. [[CrossRef](#)]
298. Kankaku, Y.; Suzuki, S.; OSAWA, Y. ALOS-2 mission and development status. In Proceedings of the 2013 IEEE International Geoscience and Remote Sensing Symposium—IGARSS, Melbourne, Australia, 21–26 July 2013; IEEE. pp. 2396–2399.
299. Hirano, A.; Welch, R.; Lang, H. Mapping from ASTER stereo image data: DEM validation and accuracy assessment. *ISPRS J. Photogramm. Remote Sens.* **2003**, *57*, 356–370. [[CrossRef](#)]
300. Takaku, J.; Tadono, T. High resolution DSM generation from ALOS PRISM-mosaic dataset. In Proceedings of the 2012 IEEE International Geoscience and Remote Sensing Symposium, Munich, Germany, 22–27 July 2012; IEEE. pp. 2687–2690.
301. Schutz, B.E.; Zwally, H.J.; Shuman, C.A.; Hancock, D.; DiMarzio, J.P. Overview of the ICESat mission. *Geophys. Res. Lett.* **2005**, *32*, 1–4. [[CrossRef](#)]
302. Le Roy, Y.; Deschaux-Beaume, M. SRAL, A RADAR ALTIME TER DESIGNED TO MEASURE A WIDE RANGE OF SURFACE TYPES Thales Alenia Space, 26 avenue Jean -François Champollion-31037 Toulouse Cedex 1 (France) * Presenting author (E-mail: yves.le-roy@thalesaleniaspace.com) European Space. *Power* **2009**, *1*, 445–448.
303. Reigber, A.; Horn, R.; Nottensteiner, A.; Prats, P.; Scheiber, R.; Bethke, K.; Baumgartner, S. Current status of DLR's new F-SAR sensor. *Eusar* **2010**, 1078–1081.
304. Donnellan, A.; Parker, J.; Hensley, S.; Pierce, M.; Wang, J.; Rundle, J. UAVSAR observations of triggered slip on the Imperial, Superstition Hills, and East Elmore Ranch Faults associated with the 2010 M 7.2 El Mayor-Cucapah earthquake. *Geochem. Geophys. Geosyst.* **2014**, *15*, 815–829. [[CrossRef](#)]
305. Shiroma, G.H.; de Macedo, K.A.; Wimmer, C.; Fernandes, D.; Barreto, T.L. Combining dual-band capability and PolInSAR technique for forest ground and canopy estimation. In Proceedings of the 2014 IEEE Geoscience and Remote Sensing Symposium, Quebec City, QC, Canada, 13–18 July 2014; pp. 4592–4595.
306. Shimada, M.; Kawano, N.; Watanabe, M.; Motooka, T.; Ohki, M. Calibration and validation of the Pi-SAR-L2. In Proceedings of the Proc. of APSAR 2013, Tsukuba, Japan, 23–27 September 2013; pp. 194–197.
307. Leica DMC III Luftbild-Digitalkamera. 2018. Available online: <https://leica-geosystems.com/de-de/products/airborne-systems/imaging-sensors/leica-dmciii> (accessed on 30 January 2018).
308. Leica ADS40 Large-Scale Digital Imagery. 2004. Available online: http://www.dlr.de/os/en/Portaldata/48/Resources/dokumente/ads40_flyer_leica.pdf (accessed on 30 January 2018).
309. Quantum Systems, Q. Airborne LiDAR. 2018. Available online: <https://www.quantum-systems.com/download/31626/> (accessed on 30 January 2018).
310. DJI Phantom 4 Pro Specs. 2018. Available online: <https://www.dji.com/phantom-4-pro/info#specs> (accessed on 30 January 2018).
311. Riegl VUX-1UAV. 2018. Available online: http://www.riegl.com/uploads/tx_pxpriegldownloads/RIEGL_VUX-1UAV_Datasheet_2017-09-01.pdf (accessed on 30 January 2018).
312. Nurminen, K.; Litkey, P.; Honkavaara, E.; Vastaranta, M.; Holopainen, M.; Lyytikäinen-Saarenmaa, P.; Kantola, T.; Lyytikäinen, M. Automation aspects for the georeferencing of photogrammetric aerial image archives in forested scenes. *Remote Sens.* **2015**, *7*, 1565–1593. [[CrossRef](#)]

313. Cigna, F.; Lasaponara, R.; Masini, N.; Milillo, P.; Tapete, D. Persistent scatterer interferometry processing of COSMO-skymed stripmap HIMAGE time series to depict deformation of the historic centre of Rome, Italy. *Remote Sens.* **2014**, *6*, 12593–12618. [[CrossRef](#)]
314. Wegmüller, U.; Walter, D.; Spreckels, V.; Werner, C. Evaluation of TerraSAR-X DINSAR and IPTA for ground motion monitoring. In Proceedings of the 3rd TerraSAR-X Science Team Meeting, DLR, Oberpfaffenhofen, Germany, 25–26 November 2008; pp. 25–26.
315. Wang, L.; Marzahn, P.; Bernier, M.; Jacome, A.; Poulin, J.; Ludwig, R. Comparison of TerraSAR-X and ALOS PALSAR Differential Interferometry with Multisource DEMs for Monitoring Ground Displacement in a Discontinuous Permafrost Region. *IEEE J. Sel. Top. Appl. Earth Obs. Remote Sens.* **2017**, *10*, 4074–4093. [[CrossRef](#)]
316. Pepe, A.; Sansosti, E.; Berardino, P.; Lanari, R. On the Generation of {ERS/ENVISAT} {DInSAR} Time-Series Via the {SBAS} Technique. *Geosci. Remote Sens. Lett.* **2005**, *2*, 265–269. [[CrossRef](#)]
317. Goel, K.; Adam, N.; Shau, R.; Rodriguez-Gonzalez, F. Improving the reference network in wide-area Persistent Scatterer Interferometry for non-urban areas. In Proceedings of the 2016 IEEE International Geoscience and Remote Sensing Symposium (IGARSS), Beijing, China, 10–15 July 2016; IEEE. pp. 1448–1451.
318. Shanker, P.; Casu, F.; Zebker, H.A.; Lanari, R. Comparison of persistent scatterers and small baseline time-series InSAR results: A case study of the San Francisco bay area. *IEEE Geosci. Remote Sens. Lett.* **2011**, *8*, 592–596. [[CrossRef](#)]
319. Khan, S.D.; Huang, Z.; Karacay, A. Study of ground subsidence in northwest Harris county using GPS, LiDAR, and InSAR techniques. *Nat. Hazards* **2014**, *73*, 1143–1173. [[CrossRef](#)]
320. Feng, G.; Ding, X.; Li, Z.; Mi, J.; Zhang, L.; Omura, M. Calibration of an insar-derived coseismic deformation map associated with the 2011 mw-9.0 tohoku-oki earthquake. *IEEE Geosci. Remote Sens. Lett.* **2012**, *9*, 302–306. [[CrossRef](#)]
321. De Luca, C.; Bonano, M.; Casu, F.; Fusco, A.; Lanari, R.; Manunta, M.; Manzo, M.; Pepe, A.; Zinno, I. Automatic and Systematic Sentinel-1 SBAS-DInSAR Processing Chain for Deformation Time-series Generation. *Procedia Comput. Sci.* **2016**, *100*, 1176–1180. [[CrossRef](#)]
322. Navarro-Sanchez, V.D.; Lopez-Sanchez, J.M.; Ferro-Famil, L. Polarimetric approaches for persistent scatterers interferometry. *IEEE Trans. Geosci. Remote Sens.* **2014**, *52*, 1667–1676. [[CrossRef](#)]
323. Czarnogorska, M.; Samsonov, S.; White, D.; Decker, V. Ground deformation at the Aquistore CO₂ storage site in Saskatchewan (Canada) measured by RADARSAT-2 DInSAR. In Proceedings of the 2014 IEEE Geoscience and Remote Sensing Symposium, Quebec City, QC, Canada, 13–18 July 2014; IEEE. pp. 445–447.
324. Natsuaki, R.; Nagai, H.; Motohka, T.; Ohki, M.; Watanabe, M.; Thapa, R.B.; Tadono, T.; Shimada, M.; Suzuki, S. SAR interferometry using ALOS-2 PALSAR-2 data for the Mw 7.8 Gorkha, Nepal earthquake. *Earth Planets Sp.* **2016**, *68*, 15. [[CrossRef](#)]
325. Montenbruck, O.; Allende-Alba, G.; Rosello, J.; Tossaint, M.; Zangerl, F. Precise Orbit and Baseline Determination for the SAOCOM-CS Bistatic Radar Mission. *Navigation* **2018**, *65*, 15–24. [[CrossRef](#)]
326. Optech ALTM Gemini—Your Base Mapping Solution. 2008. Available online: <http://airsensing.com/wp-content/uploads/2014/11> (accessed on 7 November 2020).
327. Imakiire, T.; Koarai, M. Wide-area land subsidence caused by “the 2011 off the Pacific Coast of Tohoku Earthquake”. *Soils Found.* **2012**, *52*, 842–855. [[CrossRef](#)]
328. Suh, J.; Choi, Y. Mapping hazardous mining-induced sinkhole subsidence using unmanned aerial vehicle (drone) photogrammetry. *Environ. Earth Sci.* **2017**, *76*, 144. [[CrossRef](#)]
329. Gasperini, D.; Allemand, P.; Delacourt, C.; Grandjean, P. Potential and limitation of UAV for monitoring subsidence in municipal landfills. *Int. J. Environ. Technol. Manag.* **2014**, *17*, 1. [[CrossRef](#)]
330. Weiss, D.J.; Walsh, S.J. Remote Sensing of Mountain Environments. *Geogr. Compass* **2009**, *3*, 1–21. [[CrossRef](#)]
331. Farmakis-Serebryakova, M.; Hurni, L. Comparison of Relief Shading Techniques Applied to Landforms. *ISPRS Int. J. Geo-Inf.* **2020**, *9*, 253. [[CrossRef](#)]
332. Meybeck, M.; Green, P.; Vörösmarty, C. A New Typology for Mountains and Other Relief Classes. *Mt. Res. Dev.* **2001**, *21*, 34–45. [[CrossRef](#)]
333. Ganci, G.; Cappello, A.; Bilotta, G.; Del Negro, C. How the variety of satellite remote sensing data over volcanoes can assist hazard monitoring efforts: The 2011 eruption of Nabro volcano. *Remote Sens. Environ.* **2020**, *236*, 111426. [[CrossRef](#)]

334. Calvari, S.; Ganci, G.; Victória, S.; Hernandez, P.; Perez, N.; Barrancos, J.; Alfama, V.; Dionis, S.; Cabral, J.; Cardoso, N.; et al. Satellite and Ground Remote Sensing Techniques to Trace the Hidden Growth of a Lava Flow Field: The 2014–2015 Effusive Eruption at Fogo Volcano (Cape Verde). *Remote Sens.* **2018**, *10*, 1115. [[CrossRef](#)]
335. Ganci, G.; James, M.R.; Calvari, S.; Negro, C. Del Separating the thermal fingerprints of lava flows and simultaneous lava fountaining using ground-based thermal camera and SEVIRI measurements. *Geophys. Res. Lett.* **2013**, *40*, 5058–5063. [[CrossRef](#)]
336. Casagli, N.; Frodella, W.; Morelli, S.; Tofani, V.; Ciampalini, A.; Intrieri, E.; Raspini, F.; Rossi, G.; Tanteri, L.; Lu, P. Spaceborne, UAV and ground-based remote sensing techniques for landslide mapping, monitoring and early warning. *Geoenvironmental Disasters* **2017**, *4*, 9. [[CrossRef](#)]
337. van der Meer, F.; Hecker, C.; van Ruitenbeek, F.; van der Werff, H.; de Wijkerslooth, C.; Wechsler, C. Geologic remote sensing for geothermal exploration: A review. *Int. J. Appl. Earth Obs. Geoinf.* **2014**, *33*, 255–269. [[CrossRef](#)]
338. Liang, G.; Xiao, K.; Zheng, H.; Zhao, W.; Zhang, Q.; Gao, C. Rockfall monitoring based on multichannel synthetic aperture radar. *Vibroengineering Procedia* **2019**, *22*, 146–152.
339. Cabré, A.; Remy, D.; Aguilar, G.; Carretier, S.; Riquelme, R. Mapping rainstorm erosion associated with an individual storm from InSAR coherence loss validated by field evidence for the Atacama Desert. *Earth Surf. Process. Landf.* **2020**, *45*, 2091–2106.
340. Caviezel, A.; Gerber, W. Brief Communication: Measuring rock decelerations and rotation changes during short-duration ground impacts. *Nat. Hazards Earth Syst. Sci.* **2018**, *18*, 3145–3151. [[CrossRef](#)]
341. Fanos, A.M.; Pradhan, B.; Alamri, A.; Lee, C.W. Machine Learning-Based and 3D Kinematic Models for Rockfall Hazard Assessment Using LiDAR Data and GIS. *Remote Sens.* **2020**, *12*, 1755. [[CrossRef](#)]
342. Lato, M.J.; Anderson, S.; Porter, M.J. Reducing Landslide Risk Using Airborne Lidar Scanning Data. *J. Geotech. Geoenvironmental Eng.* **2019**, *145*, 06019004. [[CrossRef](#)]
343. Liu, H.; Wang, X.; Liao, X.; Sun, J.; Zhang, S. Rockfall Investigation and Hazard Assessment from Nang County to Jiacha County in Tibet. *Appl. Sci.* **2019**, *10*, 247. [[CrossRef](#)]
344. Caviezel, A.; Demmel, S.E.; Ringenbach, A.; Bühler, Y.; Lu, G.; Christen, M.; Dinneen, C.E.; Eberhard, L.A.; von Rickenbach, D.; Bartelt, P. Reconstruction of four-dimensional rockfall trajectories using remote sensing and rock-based accelerometers and gyroscopes. *Earth Surf. Dyn.* **2019**, *7*, 199–210. [[CrossRef](#)]
345. Hormes, A.; Adams, M.; Amabile, A.S.; Blauensteiner, F.; Demmler, C.; Fey, C.; Ostermann, M.; Rechberger, C.; Sausgruber, T.; Vecchiotti, F.; et al. Innovative methods to monitor rock and mountain slope deformation. *Geomech. Tunn.* **2020**, *13*, 88–102. [[CrossRef](#)]
346. Lambert, S.; Nicot, F. *Rockfall Engineering*; Lambert, S., Nicot, F., Eds.; John Wiley & Sons, Inc.: Hoboken, NJ, USA, 2013; ISBN 9781118601532.
347. Bonneau, D.A.; Hutchinson, D.J.; DiFrancesco, P.-M.; Coombs, M.; Sala, Z. Three-dimensional rockfall shape back analysis: Methods and implications. *Nat. Hazards Earth Syst. Sci.* **2019**, *19*, 2745–2765. [[CrossRef](#)]
348. Godone, D.; Allasia, P.; Borrelli, L.; Gullà, G. UAV and Structure from Motion Approach to Monitor the Maierato Landslide Evolution. *Remote Sens.* **2020**, *12*, 1039. [[CrossRef](#)]
349. Wu, Q.; Song, C.; Liu, K.; Ke, L. Integration of TanDEM-X and SRTM DEMs and Spectral Imagery to Improve the Large-Scale Detection of Opencast Mining Areas. *Remote Sens.* **2020**, *12*, 1451. [[CrossRef](#)]
350. Song, W.; Song, W.; Gu, H.; Li, F. Progress in the Remote Sensing Monitoring of the Ecological Environment in Mining Areas. *Int. J. Environ. Res. Public Health* **2020**, *17*, 1846. [[CrossRef](#)]
351. Nascimento, F.S.; Gastauer, M.; Souza-Filho, P.W.M.; Nascimento, W.R.; Santos, D.C.; Costa, M.F. Land cover changes in open-cast mining complexes based on high-resolution remote sensing data. *Remote Sens.* **2020**, *12*, 611. [[CrossRef](#)]
352. Schmidt, H.; Glaesser, C. Multitemporal analysis of satellite data and their use in the monitoring of the environmental impacts of open cast lignite mining areas in eastern germany. *Int. J. Remote Sens.* **1998**. [[CrossRef](#)]
353. Verma, S.; Malpe, D.B. Mining Activity Monitoring Through Remote Sensing and GIS- A Case Study from Wani Area of Yavatmal District, Maharashtra. *Int. J. Adv. Remote Sens. GIS* **2017**. [[CrossRef](#)]
354. Bhattacharya, R.K.; Das Chatterjee, N.; Das, K. Impact of instream sand mining on habitat destruction or transformation using coupling models of HSI and MLR. *Spat. Inf. Res.* **2020**, *28*, 67–85. [[CrossRef](#)]
355. Gläßer, C.; Birger, J.; Herrmann, B. Integrated monitoring and management system of lignite opencast mines using multiple remote sensing data and GIS. In *Operational Remote Sensing for Sustainable Development*;

- Nieuwenhuis, G.J.A., Vaughan, R.A., Molehaar, M., Eds.; *Operational Remote Sensing for Sustainable Development*: Rotterdam, The Netherlands, 1999; pp. 439–444.
356. Götze, C.; Beyer, F.; Gläßer, C. Pioneer vegetation as an indicator of the geochemical parameters in abandoned mine sites using hyperspectral airborne data. *Environ. Earth Sci.* **2016**, *75*, 613. [[CrossRef](#)]
357. Platt, R.V.; Manthos, D.; Amos, J. Estimating the Creation and Removal Date of Fracking Ponds Using Trend Analysis of Landsat Imagery. *Environ. Manage.* **2018**, *61*, 310–320. [[CrossRef](#)]
358. Khan, N.M.; Rastokuev, V.V.; Sato, Y.; Shiozawa, S. Assessment of hydrosaline land degradation by using a simple approach of remote sensing indicators. *Agric. Water Manag.* **2005**, *77*, 96–109. [[CrossRef](#)]
359. Symeonakis, E.; Drake, N. Monitoring desertification and land degradation over sub-Saharan Africa. *Int. J. Remote Sens.* **2004**, *25*, 573–592. [[CrossRef](#)]
360. Hunter, F.D.L.; Mitchard, E.T.A.; Tyrrell, P.; Russell, S. Inter-Seasonal Time Series Imagery Enhances Classification Accuracy of Grazing Resource and Land Degradation Maps in a Savanna Ecosystem. *Remote Sens.* **2020**, *12*, 198. [[CrossRef](#)]
361. Giuliani, G.; Mazzetti, P.; Santoro, M.; Nativi, S.; Van Bemmelen, J.; Colangeli, G.; Lehmann, A. Knowledge generation using satellite earth observations to support sustainable development goals (SDG): A use case on Land degradation. *Int. J. Appl. Earth Obs. Geoinf.* **2020**, *88*, 102068. [[CrossRef](#)]
362. del Valle, H.F.; Blanco, P.D.; Metternicht, G.I.; Zinck, J.A. Radar Remote Sensing of Wind-Driven Land Degradation Processes in Northeastern Patagonia. *J. Environ. Qual.* **2010**, *39*, 62–75. [[CrossRef](#)] [[PubMed](#)]
363. Eagleston, H.; Marion, J.L. Application of airborne LiDAR and GIS in modeling trail erosion along the Appalachian Trail in New Hampshire, USA. *Landsc. Urban Plan.* **2020**, *198*, 103765. [[CrossRef](#)]
364. Abdelkareem, M.; Gaber, A.; Abdalla, F.; El-Din, G.K. Use of optical and radar remote sensing satellites for identifying and monitoring active/inactive landforms in the driest desert in Saudi Arabia. *Geomorphology* **2020**, *362*, 107197. [[CrossRef](#)]
365. Davis, J.M.; Grindrod, P.M.; Boazman, S.J.; Vermeesch, P.; Baird, T. Quantified Aeolian Dune Changes on Mars Derived From Repeat Context Camera Images. *Earth Sp. Sci.* **2020**, *7*. [[CrossRef](#)]
366. Shumack, S.; Hesse, P.; Farebrother, W. Deep learning for dune pattern mapping with the AW3D30 global surface model. *Earth Surf. Process. Landf.* **2020**, *45*, 2417–2431. [[CrossRef](#)]
367. Radebaugh, J.; Lorenz, R.; Farr, T.; Paillou, P.; Savage, C.; Spencer, C. Linear dunes on Titan and earth: Initial remote sensing comparisons. *Geomorphology* **2010**, *121*, 122–132. [[CrossRef](#)]
368. Blumberg, D.G. Remote Sensing of Desert Dune Forms by Polarimetric Synthetic Aperture Radar (SAR). *Remote Sens. Environ.* **1998**, *65*, 204–216. [[CrossRef](#)]
369. Bradley, A.V.; Haughan, A.E.; Al-Dughairi, A.; McLaren, S.J. Spatial variability in shrub vegetation across dune forms in central Saudi Arabia. *J. Arid Environ.* **2019**, *161*, 72–84. [[CrossRef](#)]
370. Bhadra, B.K.; Rehpade, S.B.; Meena, H.; Srinivasa Rao, S. Analysis of Parabolic Dune Morphometry and Its Migration in Thar Desert Area, India, using High-Resolution Satellite Data and Temporal DEM. *J. Indian Soc. Remote Sens.* **2019**, *47*, 2097–2111. [[CrossRef](#)]
371. Warren, A.; Allison, D. The palaeoenvironmental significance of dune size hierarchies. *Palaeogeogr. Palaeoclimatol. Palaeoecol.* **1998**, *137*, 289–303. [[CrossRef](#)]
372. Michel, S.; Avouac, J.-P.; Ayoub, F.; Ewing, R.C.; Vriend, N.; Heggy, E. Comparing dune migration measured from remote sensing with sand flux prediction based on weather data and model, a test case in Qatar. *Earth Planet. Sci. Lett.* **2018**, *497*, 12–21. [[CrossRef](#)]
373. Mandlbürger, G.; Hauer, C.; Wieser, M.; Pfeifer, N. Topo-Bathymetric LiDAR for Monitoring River Morphodynamics and Instream Habitats—A Case Study at the Pielach River. *Remote Sens.* **2015**, *7*, 6160–6195. [[CrossRef](#)]
374. Allen, G.H.; Pavelsky, T. Global extent of rivers and streams. *Science* **2018**, *361*, 585–588. [[CrossRef](#)]
375. Bird, S.; Hogan, D.; Schwab, J. Photogrammetric monitoring of small streams under a riparian forest canopy. *Earth Surf. Process. Landf.* **2010**, *970*, 952–970. [[CrossRef](#)]
376. Wheaton, J.M.; Fryirs, K.A.; Brierley, G.; Bangen, S.G.; Bouwes, N.; O'Brien, G. Geomorphic mapping and taxonomy of fluvial landforms. *Geomorphology* **2015**, *248*, 273–295. [[CrossRef](#)]
377. Demarchi, L.; Bizzi, S.; Piégay, H. Regional hydromorphological characterization with continuous and automated remote sensing analysis based on VHR imagery and low-resolution LiDAR data. *Earth Surf. Process. Landf.* **2017**, *42*, 531–551. [[CrossRef](#)]

378. Pinheiro, M.; Amao-Oliva, J.; Scheiber, R.; Jaeger, M.; Horn, R.; Keller, M.; Fischer, J.; Reigber, A. Dual-frequency airborne SAR for large scale mapping of tidal flats. *Remote Sens.* **2020**, *12*, 1827. [\[CrossRef\]](#)
379. Belletti, B.; Dufour, S.; Piégay, H. What is the Relative Effect of Space and Time to Explain the Braided River Width and Island Patterns at a Regional Scale? *River Res. Appl.* **2015**, *31*, 1–15. [\[CrossRef\]](#)
380. Lallias-Tacon, S.; Liébault, F.; Piégay, H. Step by step error assessment in braided river sediment budget using airborne LiDAR data. *Geomorphology* **2014**, *214*, 307–323. [\[CrossRef\]](#)
381. Houser, C.; Hamilton, S. Morphodynamics of a 1000-year flood in the Kamp River, Austria, and impacts on floodplain morphology. *Earth Surf. Process. Landf.* **2009**, *34*, 613–628. [\[CrossRef\]](#)
382. Biron, P.M.; Choné, G.; Buffin-Bélanger, T.; Demers, S.; Olsen, T. Improvement of streams hydro-geomorphological assessment using LiDAR DEMs. *Earth Surf. Process. Landf.* **2013**, *38*, 1808–1821. [\[CrossRef\]](#)
383. Perks, M.T.; Russell, A.J.; Large, A.R.G. Technical Note: Advances in flash flood monitoring using UAVs. *Hydrol. Earth Syst. Sci. Discuss.* **2016**, *20*, 4005–4015. [\[CrossRef\]](#)
384. Ridolf, E.; Manciola, P. Water Level Measurements from Drones: A Pilot Case Study at a Dam Site. *Water* **2018**, *10*, 297. [\[CrossRef\]](#)
385. Hirpa, F.A.; Hopson, T.M.; De Groeve, T.; Brakenridge, G.R.; Gebremichael, M.; Restrepo, P.J. Upstream satellite remote sensing for river discharge forecasting: Application to major rivers in South Asia. *Remote Sens. Environ.* **2013**, *131*, 140–151. [\[CrossRef\]](#)
386. Gilvear, D.J.; Davids, C.; Tyler, A.N. The use of remotely sensed data to detect channel hydromorphology; River Tummel, Scotland. *River Res. Appl.* **2004**, *20*, 795–811. [\[CrossRef\]](#)
387. Brousse, G.; Arnaud-Fassetta, G.; Liébault, F.; Bertrand, M.; Melun, G.; Loire, R.; Malavoi, J.; Fantino, G.; Borgniet, L. Channel response to sediment replenishment in a large gravel-bed river: The case of the Saint-Sauveur dam in the Buëch River (Southern Alps, France). *River Res. Appl.* **2020**, *36*, 880–893. [\[CrossRef\]](#)
388. Vázquez-Tarrió, D.; Borgniet, L.; Liébault, F.; Recking, A. Using UAS optical imagery and SfM photogrammetry to characterize the surface grain size of gravel bars in a braided river (Vénéon River, French Alps). *Geomorphology* **2017**, *285*, 94–105. [\[CrossRef\]](#)
389. Carbonneau, P.E.; Bizzi, S.; Marchetti, G. Robotic photosieving from low-cost multicopter sUAS: A proof-of-concept. *Earth Surf. Process. Landf.* **2018**, *43*, 1160–1166. [\[CrossRef\]](#)
390. Carbonneau, P.E.; Dugdale, S.J.; Breckon, T.P.; Dietrich, J.D.; Fonstad, M.A.; Miyamoto, H.; Woodget, A.S. Generalised classification of hyperspatial resolution airborne imagery of fluvial scenes with deep convolutional neural networks. *Geophys. Res. Abstr.* **2019**, *21*, 1.
391. Carbonneau, P.E.; Lane, S.N.; Bergeron, N.E. Catchment-scale mapping of surface grain size in gravel bed rivers using airborne digital imagery. *Water Resour. Res.* **2004**, *40*. [\[CrossRef\]](#)
392. Rainey, M.; Tyler, A.; Gilvear, D.; Bryant, R.; McDonald, P. Mapping intertidal estuarine sediment grain size distributions through airborne remote sensing. *Remote Sens. Environ.* **2003**, *86*, 480–490. [\[CrossRef\]](#)
393. Cassel, M.; Piégay, H.; Fantino, G.; Lejot, J.; Bultingaire, L.; Michel, K.; Perret, F. Comparison of ground-based and UAV a-UHF artificial tracer mobility monitoring methods on a braided river. *Earth Surf. Process. Landf.* **2020**, *45*, 1123–1140. [\[CrossRef\]](#)
394. Dietrich, J.T. Bathymetric Structure-from-Motion: Extracting shallow stream bathymetry from multi-view stereo photogrammetry. *Earth Surf. Process. Landf.* **2017**, *42*, 355–364. [\[CrossRef\]](#)
395. Legleiter, C.J. Remote measurement of river morphology via fusion of LiDAR topography and spectrally based bathymetry. *Earth Surf. Process. Landf.* **2012**, *37*, 499–518. [\[CrossRef\]](#)
396. Legleiter, C.J.; Overstreet, B.T.; Glennie, C.L.; Pan, Z.; Fernandez-Diaz, J.C.; Singhanian, A. Evaluating the capabilities of the CASI hyperspectral imaging system and Aquarius bathymetric LiDAR for measuring channel morphology in two distinct river environments. *Earth Surf. Process. Landf.* **2016**, *41*, 344–363. [\[CrossRef\]](#)
397. Barale, V. Environmental Remote Sensing of the Mediterranean Sea. *J. Environ. Sci. Heal. Part A* **2003**, *38*, 1681–1688. [\[CrossRef\]](#)
398. Kaliraj, S.; Chandrasekar, N.; Ramachandran, K.K. Mapping of coastal landforms and volumetric change analysis in the south west coast of Kanyakumari, South India using remote sensing and GIS techniques. *Egypt. J. Remote Sens. Sp. Sci.* **2017**, *20*, 265–282. [\[CrossRef\]](#)
399. Dang, K.B.; Dang, V.B.; Bui, Q.T.; Nguyen, V.V.; Pham, T.P.N.; Ngo, V.L. A Convolutional Neural Network for Coastal Classification Based on ALOS and NOAA Satellite Data. *IEEE Access* **2020**, *8*, 11824–11839. [\[CrossRef\]](#)

400. Valderrama-Landeros, L.; Blanco y Correa, M.; Flores-Verdugo, F.; Álvarez-Sánchez, L.F.; Flores-de-Santiago, F. Spatiotemporal shoreline dynamics of Marismas Nacionales, Pacific coast of Mexico, based on a remote sensing and GIS mapping approach. *Environ. Monit. Assess.* **2020**, *192*.
401. Elnabwy, M.T.; Elbeltagi, E.; El Banna, M.M.; Elshikh, M.M.Y.; Motawa, I.; Kaloop, M.R. An approach based on landsat images for shoreline monitoring to support integrated coastal management - A case study, ezbet elborg, Nile delta, Egypt. *ISPRS Int. J. Geo-Inf.* **2020**, *9*, 199. [[CrossRef](#)]
402. Toure, S.; Diop, O.; Kpalma, K.; Maiga, A. Shoreline Detection using Optical Remote Sensing: A Review. *ISPRS Int. J. Geo-Inf.* **2019**, *8*, 75. [[CrossRef](#)]
403. Arcioni, M.; Bensi, P.; Fehringer, M.; Fois, F.; Heliere, F.; Lin, C.C.; Scipal, K. The Biomass mission, status of the satellite system. *Int. Geosci. Remote Sens. Symp.* **2014**, 1413–1416. [[CrossRef](#)]
404. Gebert, N.; Domínguez, B.C.; Martín, M.D.; Di Salvo, E.; Temussi, F.; Giove, P.V.; Gibbons, M.; Phelps, P.; Griffiths, L. SAR Instrument Pre-development Activities for SAOCOM-CS. In Proceedings of the 11th European Conference on Synthetic Aperture Radar EUSAR 2016 SAR, Hamburg, Germany, 6–9 June 2016; pp. 718–721.
405. Rosen, P.A.; Kim, Y.; Kumar, R.; Misra, T.; Bhan, R.; Sagi, V.R. Global persistent SAR sampling with the NASA-ISRO SAR (NISAR) mission. In Proceedings of the 2017 IEEE Radar Conference (RadarConf), Seattle, WA, USA, 8–12 May 2017; IEEE. pp. 0410–0414.
406. JAXA Advanced Land Observing Satellite-4 (ALOS-4). 2018. Available online: <http://global.jaxa.jp/projects/sat/alos4/> (accessed on 1 February 2018).
407. Moreira, A.; Krieger, G.; Hajnsek, I.; Papathanassiou, K.; Younis, M.; Lopez-Dekker, P.; Huber, S.; Villano, M.; Pardini, M.; Eineder, M.; et al. Tandem-L: A Highly Innovative Bistatic SAR Mission for Global Observation of Dynamic Processes on the Earth's Surface. *IEEE Geosci. Remote Sens. Mag.* **2015**, *3*, 8–23. [[CrossRef](#)]
408. Tandem-L. Available online: https://www.dlr.de/hr/desktopdefault.aspx/tabid-8113/14171_read-35837/ (accessed on 17 June 2020).
409. Pierdicca, N.; Davidson, M.; Chini, M.; Dierking, W.; Djavidnia, S.; Haarpaintner, J.; Hajduch, G.; Laurin, G.V.; Lavallo, M.; López-Martínez, C.; et al. The Copernicus L-band SAR mission ROSE-L (Radar Observing System for Europe) (Conference Presentation). In Proceedings of the Active and Passive Microwave Remote Sensing for Environmental Monitoring III, Strasbourg, France, 9–12 September 2019; Notarnicola, C., Pierdicca, N., Bovenga, F., Santi, E., Eds.; SPIE Remote Sensing: Strasbourg, France, 2019; p. 13.
410. Fagúndez, G.A.; Blettler, D.C.; Krumrick, C.G.; Bertos, M.A.; Trujillo, C.G. Do agrochemicals used during soybean flowering affect the visits of *Apis mellifera* L.? *Span. J. Agric. Res.* **2016**, *14*, 1130–1134. [[CrossRef](#)]
411. Cohen, M.; Larkins, A.; Semedo, P.L.; Burbidge, G. NovaSAR-S low cost spaceborne SAR payload design, development and deployment of a new benchmark in spaceborne radar. In Proceedings of the 2017 IEEE Radar Conference (RadarConf), Seattle, WA, USA, 8–12 May 2017; 2017; pp. 0903–0907.
412. Qi, W.; Dubayah, R.O. Combining Tandem-X InSAR and simulated GEDI lidar observations for forest structure mapping. *Remote Sens. Environ.* **2016**, *187*, 253–266. [[CrossRef](#)]
413. Miliareis, G.C.; Argialas, D. Segmentation of physiographic features from the global digital elevation model/GTOPO30. *Comput. Geosci.* **1999**, *25*, 715–728. [[CrossRef](#)]
414. Denker, H. Evaluation of SRTM3 and GTOPO30 terrain data in Germany. In *Gravity, Geoid and Space Missions*; Fernandes, C., BastosJoana, J., Eds.; Springer: Berlin/Heidelberg, Germany, 2004; pp. 218–223.
415. USGS 30 ARC-second Global Elevation Data, GTOPO30. Research Data Archive at the National Center for Atmospheric Research, Computational and Information Systems Laboratory. 1997. Available online: <https://doi.org/10.5065/A1Z4-EE71> (accessed on 1 January 2020).
416. USGS Shuttle Radar Topography Mission; 1 Arc Second scene SRTM_u03_n008e004; Unfilled Unfinished 2. 2004.
417. Rexer, M.; Hirt, C. Comparison of free high resolution digital elevation data sets (ASTER GDEM2, SRTM v2.1/v4.1) and validation against accurate heights from the Australian National Gravity Database. *Aust. J. Earth Sci.* **2014**, *61*, 213–226. [[CrossRef](#)]
418. Tadono, T.; Nagai, H.; Ishida, H.; Oda, F.; Naito, S.; Minakawa, K.; Iwamoto, H. GENERATION OF THE 30 M-MESH GLOBAL DIGITAL SURFACE MODEL BY ALOS PRISM. *ISPRS Int. Arch. Photogramm. Remote Sens. Spat. Inf. Sci.* **2016**, *XLI-B4*, 157–162. [[CrossRef](#)]
419. Global Land Survey Digital Elevation Model: (GLSDEM). Available online: <https://ui.adsabs.harvard.edu/abs/2019AGUFM.A33L2955F/abstract> (accessed on 17 June 2020).

420. Theobald, D.M.; Harrison-Atlas, D.; Monahan, W.B.; Albano, C.M. Ecologically-Relevant Maps of Landforms and Physiographic Diversity for Climate Adaptation Planning. *PLoS ONE* **2015**, *10*, e0143619. [CrossRef]
421. Kennedy, C.M.; Oakleaf, J.R.; Theobald, D.M.; Baruch-Mordo, S.; Kiesecker, J. Managing the middle: A shift in conservation priorities based on the global human modification gradient. *Glob. Chang. Biol.* **2019**, *25*, 811–826. [CrossRef]
422. COP-DEM. Available online: https://spacedata.copernicus.eu/documents/20126/0/GEO1988-CopernicusDEM-SPE-002_ProductHandbook_I1.00.pdf/082dd479-f908-bf42-51bf-4c0053129f7c?t=1586526993604 (accessed on 31 October 2020).
423. Stereńczak, K.; Laurin, G.V.; Chirici, G.; Coomes, D.A.; Dalponte, M.; Latifi, H.; Puletti, N. Global Airborne Laser Scanning Data Providers Database (GlobALS)—A New Tool for Monitoring Ecosystems and Biodiversity. *Remote Sens.* **2020**, *12*, 1877. [CrossRef]
424. ESA The TerraFirma Atlas. The terrain motion information service for Europe. 2009. Available online: <http://esamultimedia.esa.int/multimedia/publications/TerraFirmaAtlas/pageflip.html> (accessed on 2 December 2018).
425. Bateson, L.; Novali, F.; Cooksley, G. TerraFirma User Guide. 2010. Available online: http://www.terrafirma.eu.com/images_all_site/documents/user_guide/TerraFirma%20User%20Guide%20Oct%202010.pdf (accessed on 2 December 2018).
426. Semple, A.G.; Pritchard, M.E.; Lohman, R.B. An incomplete inventory of suspected human-induced surface deformation in North America detected by satellite interferometric synthetic-aperture radar. *Remote Sens.* **2017**, *9*, 1296. [CrossRef]
427. ArcticDEM. Available online: <https://ui.adsabs.harvard.edu/abs/2017AGUFM.C51A0951C/abstract> (accessed on 17 June 2020).
428. ArcticDEM. Available online: <https://ui.adsabs.harvard.edu/abs/2016EGUGA..18.8396M/abstract> (accessed on 17 June 2020).
429. Dai, C.; Howat, I.M. Measuring Lava Flows With ArcticDEM: Application to the 2012–2013 Eruption of Tolbachik, Kamchatka. *Geophys. Res. Lett.* **2017**, *44*, 12133–12140. [CrossRef]
430. Cignetti, M.; Guenzi, D.; Ardizzone, F.; Allasia, P.; Giordan, D. An Open-Source Web Platform to Share Multisource, Multisensor Geospatial Data and Measurements of Ground Deformation in Mountain Areas. *ISPRS Int. J. Geo-Inf.* **2019**, *9*, 4. [CrossRef]
431. Nardi, F.; Annis, A.; Di Baldassarre, G.; Vivoni, E.R.; Grimaldi, S. GFPLAIN250m, a global high-resolution dataset of earth's floodplains. *Sci. Data* **2019**, *6*, 1–6. [CrossRef]
432. Yamazaki, D.; Ikeshima, D.; Sosa, J.; Bates, P.D.; Allen, G.H.; Pavelsky, T.M. MERIT Hydro: A High-Resolution Global Hydrography Map Based on Latest Topography Dataset. *Water Resour. Res.* **2019**, *55*, 5053–5073. [CrossRef]
433. Samela, C.; Manfreda, S.; Troy, T.J. Dataset of 100-year flood susceptibility maps for the continental U.S. derived with a geomorphic method. *Data Br.* **2017**, *12*, 203–207. [CrossRef]
434. Dorigo, W.A.; Wagner, W.; Hohensinn, R.; Hahn, S.; Paulik, C.; Xaver, A.; Gruber, A.; Drusch, M.; Mecklenburg, S.; Van Oevelen, P.; et al. The International Soil Moisture Network: A data hosting facility for global in situ soil moisture measurements. *Hydrol. Earth Syst. Sci.* **2011**, *15*, 1675–1698. [CrossRef]
435. Carroll, M.L.; DiMiceli, C.M.; Townshend, J.R.G.; Sohlberg, R.A.; Noojipady, P. *Flood Map, 2008 US Midwest Flood, MOD_FLOOD.2008158.Midwest.Geog, Version 1*; University of Maryland: College Park, MD, USA, 2008.

Publisher's Note: MDPI stays neutral with regard to jurisdictional claims in published maps and institutional affiliations.



© 2020 by the authors. Licensee MDPI, Basel, Switzerland. This article is an open access article distributed under the terms and conditions of the Creative Commons Attribution (CC BY) license (<http://creativecommons.org/licenses/by/4.0/>).